UCLouvain

FACULTE DES SCIENCES

Faculté des sciences

Gas sorption in porous ionic packings

Author : **Nicolas Malherbe**

Promotors : **Prof. Yaroslav Filinchuk and Dr. Timothy Steenhaut**

Supervisor : **Guillaume Esser**

Jury members : **Pr. Torben R. Jensen, Pr. Sophie Hermans and Dr. Koen Robeyns**

Academic Year **2023-2024**

Jury members :

Prof. Torben R. Jensen – Aarhus University, Denmark

Prof. Sophie Hermans – Université catholique de Louvain

Dr. Koen Robeyns – Université catholique de Louvain

Promoters :

Prof. Yaroslav Filinchuk – Université catholique de Louvain

Dr. Timothy Steenhaut – Université catholique de Louvain

Tutor :

Guillaume Esser

Acknowledgement

I would like to express my deepest gratitude to my promoters, Prof. Yaroslav Filinchuk and Dr. Timothy Steenhaut, for their outstanding support throughout my master's thesis. I am grateful to Yaroslav for taking me under his wing as early as my second year of bachelor's studies, and to Timothy for teaching me the importance of surpassing myself and for his unwavering support. Their guidance and encouragement have been instrumental in the completion of this thesis. Very big thanks go to Jian Wang, the graduating PhD student of Prof. Yaroslav Filinchuk, who introduced me to the boron chemistry and in particular the synthesis of dodecaborates. I enjoyed sharing his office for my two first months and thank him for the continuous support, even after his departure.

I am also grateful to Prof. Torben R. Jensen, Prof. Sophie Hermans, and Dr. Koen Robeyns, members of the jury, for their time in reading and attending the defense of this thesis.

Special thanks to the remarkable team of research experts at UCLouvain who assisted with measurements and setup, particularly Dr. Koen Robeyns, Jean-François Statsyns, and Dr. Gabriella Barozzino. I extend my thanks to those at the Institut Laue-Langevin for their help with the neutron diffraction experiment: Thomas Hansen, Simon Baudouin, Alain Daramsy, and Laura Cañadillas Delgado.

I am deeply appreciative of my friends and fellow master's students for their unwavering support throughout this journey.

Lastly, I wish to extend my heartfelt thanks to my tutor, Guillaume Esser. His daily presence, both in and out of the lab, and his assistance with every synthesis and measurement have been invaluable. This thesis would not be what it is without him.

Abstract

This project focused on the synthesis, characterization, and sorption performance of porous ionic packings (PIPs), a new class of compounds made of large cations and/or anions. The thesis is divided into three experimental parts covering respectively synthesis of $(NMe_4)_2B_{12}H_{12}$ (TMAD), extension of the PIP concept through the synthesis of other PIPs, and investigation of TMAD gas sorption properties using volumetric and diffraction methods.

In the first part, the successful synthesis of face-centered cubic (*fcc*) porous TMAD was confirmed, utilizing the ionic exchange in water between $Na_2B_{12}H_{12}$·4diglyme and NMe_4Br. The synthesis conditions, particularly water temperature, were found to significantly affect the relative intensities and lattice expansion of the TMAD. Synthesis in hot water revealed an additional unidentified phase, while synthesis in cold water optimized the yield of the *fcc* TMAD.

The second part demonstrated that the PIP concept can be extended by synthesis of another PIP, $(PMe_4)_2B_{12}H_{12}$ (TMPD), the latter exhibited an *fcc* porous phase and a monoclinic non-porous phase. The *fcc* phase was obtained in pure form by synthesis in cold water. TMPD displayed thermal stability up to 420 °C, surpassing TMAD. Attempts to synthesize a dodecaborate with a lower symmetry cation, $(t\text{-}BuNH_3)_2B_{12}H_{12}$, resulted in non-porous $(t\text{-}BuNH_3)_2B_{12}H_{12}\cdot H_2O$ and $(t\text{-}BuNH_3)_3B_{12}H_{12}Br$. The presence of water in $(t\text{-}BuNH_3)_2B_{12}H_{12}\cdot H_2O$ is owing to the multiple possibilities to form both hydrogen and dihydrogen bonds.

In the third part, gas sorption properties of PIPs were investigated. Crystal structures of TMAD and $Cs_2B_{12}H_{12}$ reveal empty non-connected pores of similar size. TMAD demonstrated CO_2 and H_2 sorption capacities of 5.92 and 0.21 wt% respectively, at room temperature. The adsorption kinetics is very slow, we attribute this to slow diffusion between the non-connected pores. On the other hand, $Cs_2B_{12}H_{12}$ showed no gas sorption, suggesting the role of the rotational dynamics of cations for gas diffusion and ultimately the gas adsorption. Structural disorder hindered precise localization of CO_2 inside the pores. Exposure to air showed TMAD's ability to sorb water, as confirmed by dynamic vapor sorption (DVS) measurements. Both TMAD and TMPD exhibited phase transitions under high CO_2 or Xe pressure, indicating the

high stability of the porous phase. Sequential Rietveld refinement on Xe in TMPD revealed 25 % pore filling at 400 K.

This work shows that large ions can be assembled into close-packed structures containing relatively large, isolated pores. They are not easily accessible, since they are not connected, but they demonstrate the ability to adsorb guests, showing slow gas adsorption kinetics. The latter is likely dominated by the rotational dynamics of cations and/or anions. PIPs with these unique properties may find applications in gas storage and separation, allowing to exploit advantages of the large differences with classical porous solids.

List of abbreviations

ATR-FTIR	**A**ttenuated **T**otal **R**eflectance **F**ourier **T**ransform **I**nfrared
CCS	**C**arbon **C**apture and **S**torage
DMS	**Di**methyl**s**ulfide
DMSO	**Di**methyl**s**ulf**o**xide
DVS	**D**ynamic **V**apor **S**orption
fcc	**F**ace-**c**entered **c**ubic
IEA	**I**nternational **E**nergy **A**gency
ILL	**I**nstitut **L**aue-**L**angevin
IUPAC	**I**nternational **U**nion of **P**ure and **A**pplied **C**hemistry
Me	**Me**thyl
MOF	**M**etal-**O**rganic **F**ramework
NMR	**N**uclear **M**agnetic **R**esonance
NPD	**N**eutron **P**owder **D**iffraction
PIP	**P**orous **I**onic **P**acking
PXRD	**P**owder **X**-**R**ay **D**iffraction
RH	**R**elative **H**umidity
Rpm	**R**evolutions **p**er **m**inutes
RT	**R**oom **T**emperature
SC-XRD	**S**ingle **C**rystal **X**-**R**ay **D**iffraction
TG-DTA	**T**hermo**g**ravimetric – **D**ifferential **T**hermal **A**nalysis
TMAD	**T**etra**m**ethyl**a**mmonium **D**odecahydrododecaborate
TMPD	**T**etra**m**ethyl**p**hosphonium **D**odecahydrododecaborate
XRD	**X**-**R**ay **D**iffraction
XRF	**X**-**R**ay **F**luorescence

Content table

1. Introduction

1.1. Gas sorption

1.1.1. Motivation for energy purposes

To address climate change effectively, it is crucial to minimize the human-caused release of greenhouse gases, with a particular emphasis on reducing CO_2 emissions. Gas capture technologies holds promise to address this issue, offering potential solutions for environmental remediation challenges and storage of excess production of renewable energies.[1–3] According to the International Energy Agency (IEA), carbon capture and storage (CCS) initiatives are expected to contribute up to 12 % of CO_2 emission reductions, in the goal of reaching a 60 % reduction by 2050 compared to 2013 levels.[4] However, progress in demonstrating and deploying CCS has been slow, with currently only 30 operational projects in ten countries, capturing and storing around 40 million tons of CO_2 per year, far away from the target of billions of tons per year.[5] Projects of this nature encounter major challenges, including limited social acceptance and inadequate policy backing, even though the European Union initiates funding for such endeavors.[6–8] It is therefore imperative for researchers to explore new, more efficient and cost-effective methods for capturing and storing greenhouse gases.

In the pursuit of sustainable energy solutions, renewable energy sources like solar, hydro, and wind power have become essential alternatives to fossil fuels. Yet, their intermittent availability, heavily relying on weather conditions and time of day, creates a notable obstacle to ensuring a steady energy supply, despite the fact that electricity consumption follows a steady and predictable pattern.[9,10] Hydrogen presents a promising solution as carrier of renewable energy, although it necessitates efficient storage solutions.[11,12]

Gaseous hydrogen can be generated from diverse sources, labelled in various colors that represent different production methods and environmental impacts.[12] “Grey hydrogen” is the most common type, created by steam methane reforming, which emits loads of carbon dioxide. “Blue hydrogen” is produced similarly to grey hydrogen but with CCS technologies to reduce emissions. “Green hydrogen” is obtained through electrolysis using renewable energy sources, emitting no greenhouse gases. Other colors like pink, turquoise, and yellow also exist, each indicating a specific production method. While green hydrogen is the most environmentally

friendly, blue hydrogen is often more cost-effective due to its production process.[13] As countries aim to reduce reliance on imported fossil fuels, investing industrial and domestic hydrogen production offers a strategic advantage.[14] Hydrogen-based solutions would mitigate geopolitical risks associated with energy dependence while stimulating local economies through job creation and innovation.[15,16]

Table 1. Advantages and disadvantages of hydrogen storage methods (adapted from reference 17).

Storage method	Advantages	Disadvantages
Compressed gas	• Proven technology, particularly effective on a small scale • Pressurized hydrogen storage enables rapid filling and discharge	• Low to moderate compression with approximately 15 % energy losses • Provides hydrogen at high pressure • Safety concerns, particularly regarding leakage • Hydrogen's low density necessitates either low-temperature or high-pressure storage
Liquid hydrogen	• Effective compression • Low pressure • Cost-effective low-pressure liquid hydrogen storage system • Reliable liquid storage method requiring lower pressure than compressed gas • High liquid density and storage efficiency	• Approximately 30 % energy losses • Boil-off occurs over several days • Requires cooling systems
Solid-state	• Potential for high hydrogen density at moderate temperatures and pressures • Capability to store large amounts of hydrogen in a small volume	• Consideration of the weight and volume of the storage material

At present, hydrogen storage methods include compressing or liquefying hydrogen, or use specific storage materials. The strengths and weaknesses of each storage technique are outlined in *Table 1*.[17] Overall, compressed hydrogen storage is beneficial for fuel applications because of its swift charging and discharging capabilities. However, it necessitates compressing and high-pressure tanks, limiting its applicability. On the other hand, liquid hydrogen offers high volumetric energy density but is hindered by its energy-intensive liquefaction and storage. Corrosion can also occur due to ice formation around the tank, leading to boil-off. Metal hydrides (solid-state) provide a maximum gravimetric capacity of around 14 wt% but require high pressure and temperature for hydride formation and hydrogen release. Interestingly, hydrogen can also be stored in porous systems, which have the potency to offer not only high gravimetric capacity but also good reversibility. However, some challenges still remain, including addressing the need of low temperatures and/or high pressures, and improving the interactions with H_2 molecules.[18]

1.1.2. Physical principles

Sorption occurs when gases, dissolved substances, or liquids (sorbates) adhere to the surface of solids (sorbents) through physical and chemical forces, leading to the enrichment of one or more components in an interfacial layer.[19] Those forces can be weak, resulting in physical *ad*sorption or "physisorption", or strong, leading to chemisorption, also referred to as *ab*sorption.[20] Typical chemisorption and physisorption enthalpy ranges are 15-100 and 2-10 kcal/mol, respectively, for simple molecules.[21] The weak nature of physisorption, which is dominated by Van der Waals interactions, allows to easily form and break interactions, resulting in a reversible system. In this master's thesis, we intentionally opted to use the term *sorption* throughout the manuscript to eliminate any potential confusion, as suggested by Sing et al.[22]

The rate at which a gas physically adheres to a porous sorbent is typically governed by how quickly it diffuses into the internal pore structure.[23] Moreover, in some cases, viscous flow of gaseous sorbate or capillary condensation may dominate over actual diffusion.[21] The pore size and shape of a sorbent material therefore play a crucial role in determining its sorption capacity and efficiency. The optimal pore size is an essential parameter, as maintaining a pore size that is just right allows for efficient sorption without impeding molecular diffusion.[24,25]

The International Union of Pure and Applied Chemistry (IUPAC) categorizes pores according to their size into micropore (width of less than 2 nm), mesopore (width of 2 to 50 nm), and a macropore (width of more than 50 nm).[26] While macropores provide large diffusion channels, they contribute less to sorption compared to mesopores and micropores. Mesopores are effective at sorbing macromolecules and facilitating the passage of molecules to micropores. As pore size decreases to the micropore range, and assuming the same pore geometry, the surface area exposed to sorbates increases, resulting in higher gas sorption capacity.[27–29]

Sorption is generally assessed by measuring isotherms, which refer to the relationship between the amount of gas sorbed by the sorbent and the equilibrium pressure or concentration and the equilibrium pressure or concentration of that gas a constant temperature. Those isotherms are influenced by the different pore shapes and sizes, classified by IUPAC in six isotherm types (*Figure 1*)[22] :

- Type I: microporous;

- Type II: non-porous or macroporous;

- Type III: non-porous or macroporous with weak interactions;

- Type IV: mesoporous;

- Type V: mesoporous with weak interaction;

- Type VI: layer-by-layer adsorption on a highly non-uniform surface.

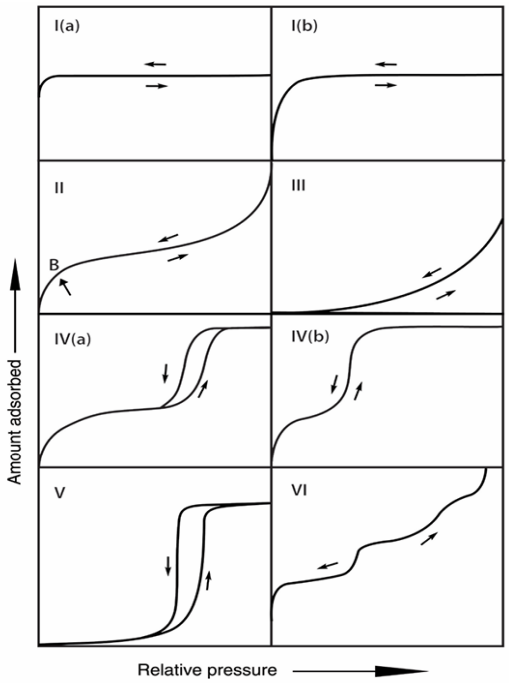

Figure 1. Classification of physisorption isotherms.

The path of the sorption and desorption isotherms are not always the same. The presence of a hysteresis between both curves indicates the presence of a non-equilibrium process, such as capillary condensation.[30]

1.2. Crystalline porous materials

1.2.1. Zeolites and MOFs

Zeolites and metal-organic frameworks (MOFs) are widely recognized as two of the most important classes of porous materials, which have been attracting considerable attention from both the academic and industrial research communities.[31–34] They both showcase impressive sorption capabilities, largely owing to their extensive surface area and adjustability.

Zeolites are highly stable microporous aluminosilicates which find applications in molecular sieving, catalysis, and more.[31,35,36]. They are built upon primary SiO_4 and AlO_4 tetrahedral building units, interconnected by shared oxygen atoms to form secondary building units. The obtained framework contains a network of channels and cages, resulting in a highly porous structure with a significant surface area. Zeolites exhibit distinct micropore sizes, categorized into large-pore, medium-pore, and small-pore zeolites based on the diameter of the rings within their structure. Large-pore zeolites feature at minimum 12-member rings (with diameters exceeding 0.70 nm),[37] while medium-pore zeolites comprise 10-member rings (with diameters ranging from 0.50 to 0.60 nm), and small pore zeolites contain 6- or 8-member rings (with diameters ranging from 0.28 to 0.40 nm).[38]

The incorporation of aluminum ions into the tetrahedral positions of the zeolite framework results in an excess of electrons, leading to a negative charge. This latter is typically balanced by exchangeable cations such as Na^+, K^+, NH_4^+, H^+, Ca^{2+}, Sr^{2+}, or Mg^{2+}.[39] Furthermore, the Si/Al ratio in zeolites is variable, offering a supplementary means to tailor their properties.[40] With their large range of topologies, zeolites are able to discriminate between molecules of high practical interest, such as CO_2, ethylene or isobutene with a precision of 0.01 nm (*Figure 2*).[41] Their meticulously structured microporous arrangement, complemented by precisely defined sites, render zeolites ideal for sorption.

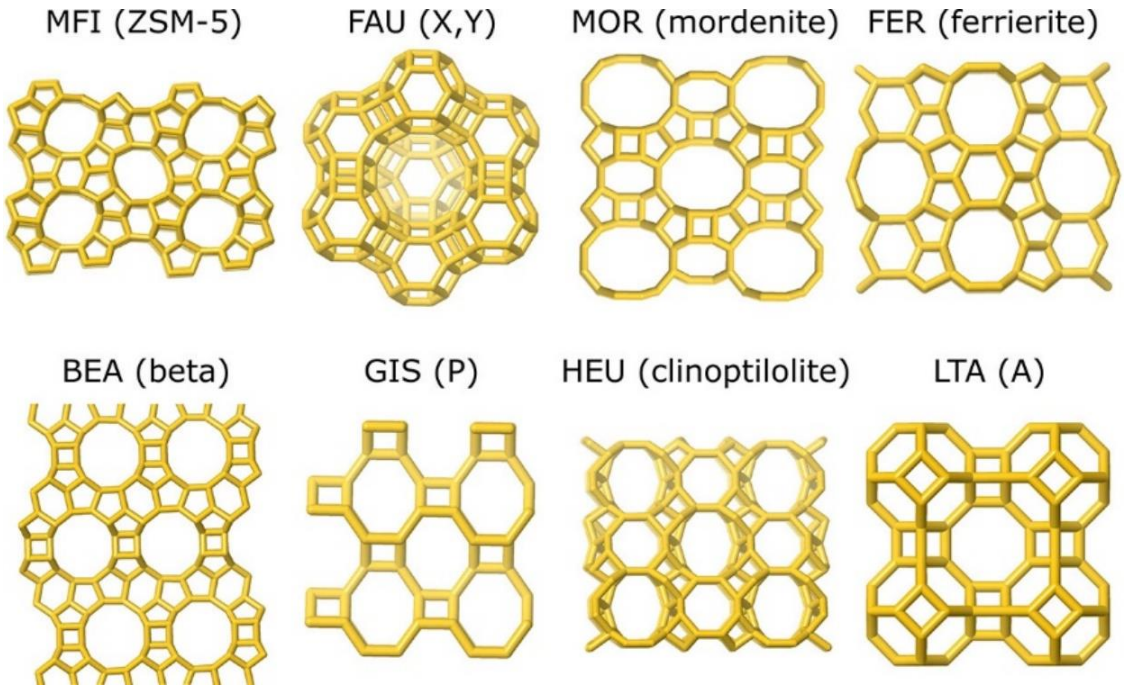

Figure 2. Front view of the main pores of various zeolites. The three letter codes written above each structure represent the official designations given to each structure by the International Zeolite Association. The common name of each zeolite is provided between parentheses. Scheme taken from reference 35.

IUPAC defines MOFs as a coordination network with organic ligands containing potential void.[42] Although MOFs generally demonstrate a crystalline structure (*Figure 3*), it is important to note that there is emerging interest in the study of amorphous and liquid MOFs,[43,44] which will however not be further developed here.

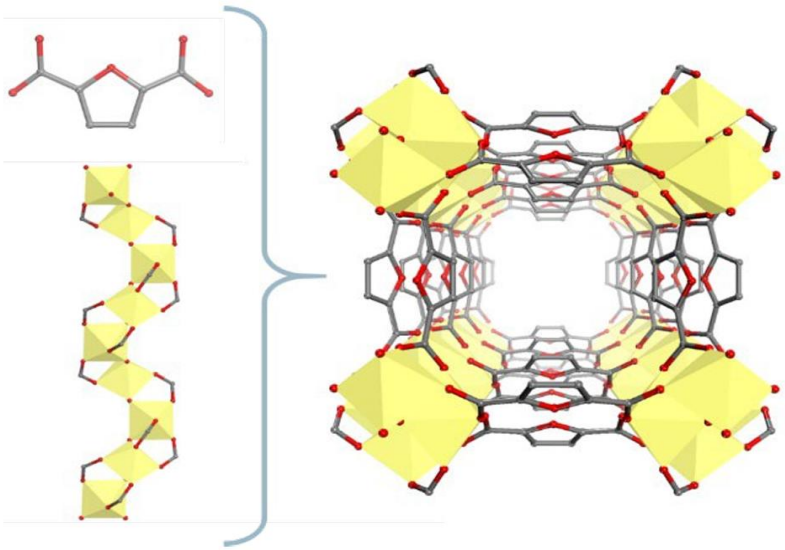

Figure 3. MIL-160 (Al) MOF structure (without hydrogens for clarity) with the Al polyhedral. The organic linker is represented in the upper left of the figure. Color code: Al = yellow, C = grey and O = red. Scheme taken from reference 44.

While most MOFs demonstrate microporosity, (i.e. HKUST-1), there are also instances of mesoporous structures, such as MIL-100 (Cr). Macroporosity can also be introduced inside the MOF structure to enhance the overall diffusion of guests within the framework. The goal is to retain the structure's inherent micro- or mesoporosity while improving the general diffusion rate by creating additional void spaces within the framework.[45–47] These materials can exhibit ultrahigh porosity, reaching up to 90 % free volume, and impressive specific surface areas extending beyond 7000 m^2/g.[48,49] These attributes have propelled MOFs to a position of increasing significance in the domain of porous solids.[50]

The versatility and adjustability of MOFs are remarkable, as they enable precise manipulation of pore size, shape, functionality, and chemical stability through the selection of metal and linker components.[51,52] Customizing specific sites within MOF pores for particular guests enables targeted host-guest interactions. This involves aligning the sizes and shapes of pores and guests, as well as adjusting host-guest interactions to improve both physical and chemical properties.[53] These interactions include diverse mechanisms, including hydrogen bonding, π–π stacking, electrostatic interactions, van der Waals forces, and coordination with open metal centers.

However, MOFs often face stability issues stemming from thermal, chemical, and mechanical factors, posing challenges for gas storage.[54,55] Thermal instability, can lead to structural degradation of the MOF material, reducing its gas sorption capacity or altering its pore structure. Similarly, chemical instability may result in reactions with gases or contaminants, affecting the integrity of the MOF and its gas storage properties. Mechanical instability, such as structural collapse, may result in the loss of porosity. The degradation of MOFs typically occurs in two fashions: the rupture of metal-ligand bonds and the formation of more stable products.[56,57] In recent years, several promising techniques have emerged to enhance MOF stability, with a particular emphasis on chemical stability.[51]

1.2.2. Fullerenes: materials with non-interconnected pores

The fullerene family, the third allotropic form of carbon, is characterized by carbon-based molecules often forming spheres, tubes, or other shapes.[58,59] They can undergo a range of reactions, including reduction, oxidation, hydrogenation, halogenation, and nucleophilic reactions, allowing for easy surface modification and therefore tuning their properties.[60]

Moreover, fullerenes showcase loads of advantages, such as high thermal/chemical stability and a high specific surface area.[61] Their versatility in undergoing various chemical reactions opens doors to numerous potential applications in diverse fields such as material chemistry, electronics, medicine, nanotechnology, etc.[62–64]

Buckminsterfullerene, or C_{60}, consists of 60 carbon atoms arranged in a hollow sphere, resembling a soccer ball. The unique structure of C_{60} forms a truncated icosahedron, featuring 12 pentagonal faces and 20 hexagonal faces. Each carbon atom within C_{60} forms bonds with three neighboring carbon atoms, creating alternating single and double bonds, enabling significant resonance stabilization, and leading to outstanding stability.[65] The suitable crystallographic face-centered cubic (*fcc*) form of C_{60} fullerene possesses interstitial voids due to the specific arrangement of the large and spherical C_{60} molecules in the crystal lattice (*Figure 4*). Hence, we here coin this type of structure as "*porous molecular packing*". Despite the pores not being interconnected, *in situ* XRD studies have demonstrated that C_{60} can effectively sorb gases such as N_2, O_2, and Kr.[66,67]

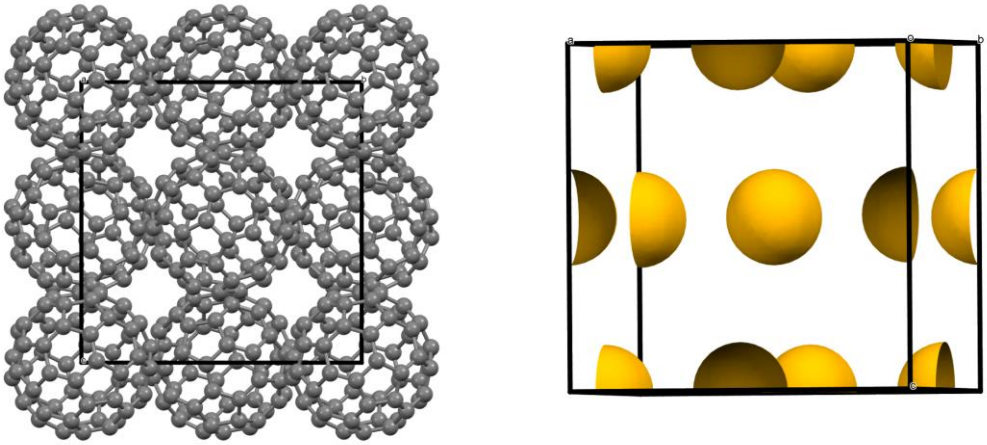

Figure 4. Crystal structure of C_{60} on the left and the solvent accessible voids on the right, utilizing a 1.5 Å probe radius. Color code: C = grey and voids = yellow.

1.2.3. Porous ionic packing

Building on the "porous molecular packing" concept we just mentioned, we hereby introduce the concept of "porous ionic packings" (PIP), extending this idea to ions. This strategy involves the packing of large spherical ions together to yield structures with interstitial voids

(*Figure 5*). Generally, to enable gas sorption within the framework, the voids must be interconnected to form continuous pores.

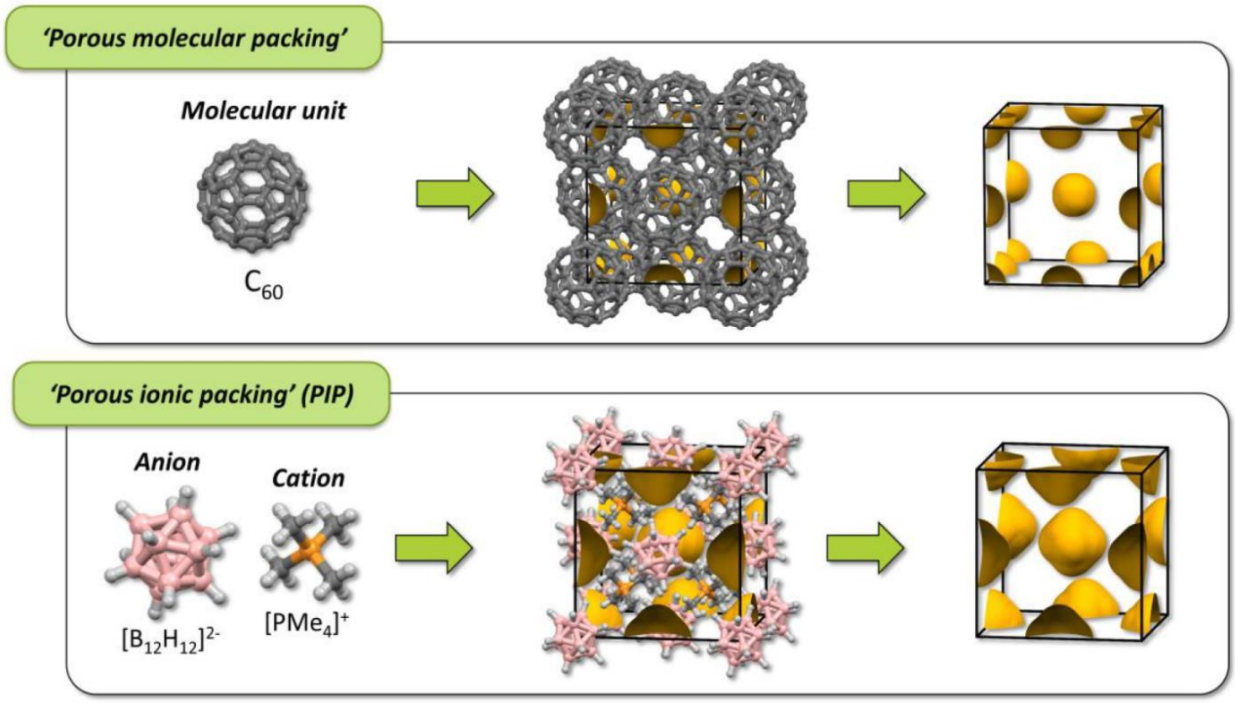

Figure 5. Illustration of the formation of voids in a "porous molecular packing" induced by assembly of C_{60} molecules and of the "porous ionic packing" (PIP) $(PMe_4)_2B_{12}H_{12}$. Building blocks are shown on the left, packings with voids in the middle, and isolated pores on the right. Color code: C = grey, H = white, B = pinkish, P = orange, voids = yellow.

Closo-dodecaborates $[B_{12}H_{12}]^{2-}$ are great examples of ions large enough to create interstitial voids in their crystal lattice. When paired with alkali metal ions, the dodecaborate anion tends to form a *fcc* lattice of the antifluorite type, where the anion occupies the positions of Cu atoms in the Cu-type structure type and the cation are taking the tetrahedral site formed by the anions, as depicted in *Figure 6*. The resulting structure appears to contain relatively large unoccupied voids. The ionic radii were obtained from the Shannon-Prewitt tables of ionic radii, and the void accessible solvent volume was extracted from the cif files of the corresponding dodecaborates, using the software Mercury, with a probe radius of 1.2 Å.[68] These structures, belonging to the space group $Fm\bar{3}$, are observed for alkali metals larger than Na^+ ($Na_2B_{12}H_{12}$ is monoclinic). By increasing the ionic radius of the cation paired with $[B_{12}H_{12}]^{2-}$, the voids are

logically expanded, as shown in *Figure 7* below. Therefore, the porosity can indeed be tuned by increasing the cation size, while maintaining the same type of lattice (*fcc* anti-CaF_2 type). To achieve this, it is crucial to conserve the stoichiometry of the ions and to keep the anion/cation size ratio within an acceptable range of phase stability. Otherwise, the coordination and packing may change, resulting in a different structure type.

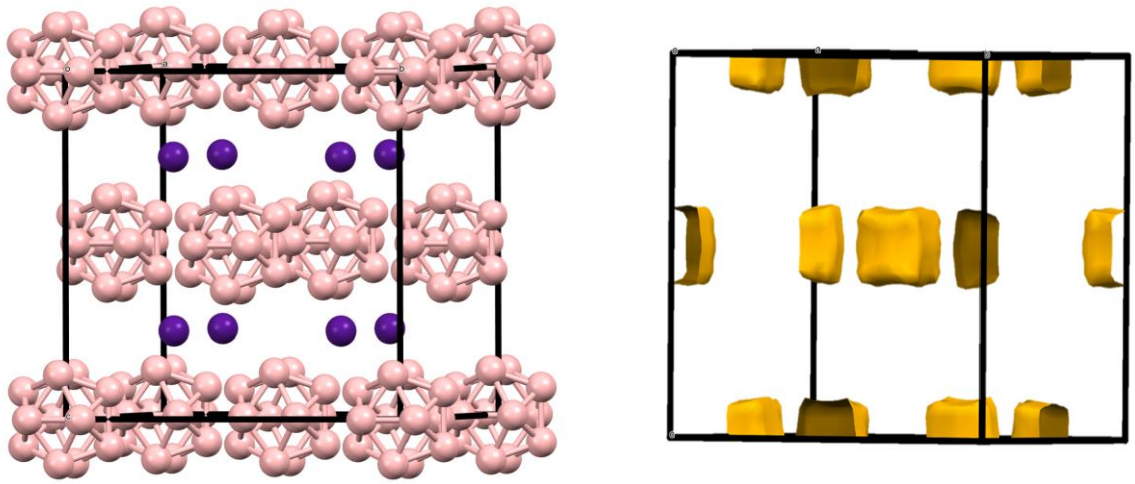

Figure 6. The anti-CaF_2 crystal structure of $Cs_2B_{12}H_{12}$ (without hydrogen for clarity) on the left and the solvent accessible voids on the right, utilizing a probe radius of 1.2 Å. Color code : B = pinkish, Cs = purple, voids = yellow. Scheme realized using the software Mercury.

The dodecaborate anion can participate in rapid rotational motion. This significant dynamical feature contributes to the entropic part of the free energy, which determines the thermodynamic stability of the phase. Changes in the rotational motion may lead to structural transitions, to conductivity of metal ions in the solid-state and to the diffusion of neutral molecules inside the bulk of the porous structure. Therefore, understanding the anion reorientation dynamics is crucial for comprehending the fundamental properties of dodecaborate salts, such as thermal stability and crystal structure symmetry.[69] During rotation, the anions approach spherical symmetry, averaging out local hydrogen–cation interactions and more closely following the ideal packing of hard spheres. This results in the stabilization of higher crystal symmetries.[70] This rotational motion also contributes to these compounds being excellent solid-state ionic conductors.[71,72] Unfortunately, these compounds do not meet the

criteria to be considered PIPs, as they contain voids rather than pores, indicating a lack of connectivity between the voids.

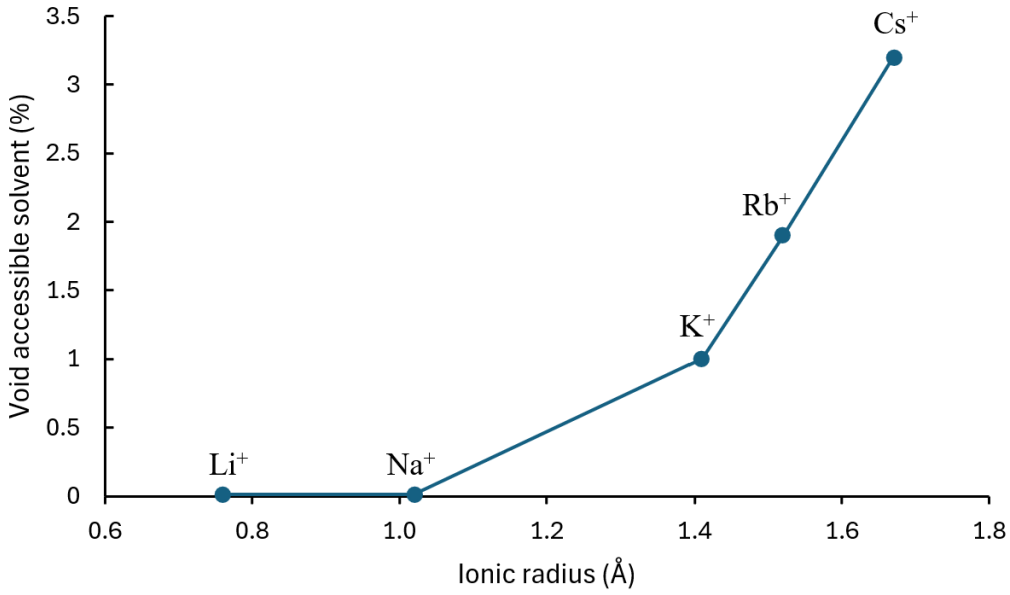

Figure 7. Plot of the ionic radius of alkali metals (M^+) and the void accessible solvent of the crystal lattice of $M_2[B_{12}H_{12}]$.

By serendipity, a member of our group (Jian Wang) discovered that the cation exchange between an alkali metal dodecaborate and the organic cation NMe_4^+ led to tetramethylammonium dodecaborate (TMAD), which exhibited a porous anti-CaF_2 type of structure. The NMe_4^+ mobility could enable the connection of the voids and result in effective reversible gas sorption within the framework. Indeed, this tetrahedral cation could promote guest insertion through a paddle-wheel mechanism, namely the coupling of ion rotation with guest diffusion. Therefore, the tetramethylammonium dodecaborate (TMAD) was the first PIP discovered by our group.

1.3. Characterization of porous materials

1.3.1. Structure

Comprehensive characterization is crucial in porous materials to gain a detailed understanding of the structural, chemical, and physical properties of these materials. Various analytical techniques are used to evaluate synthesis outcomes, determine crystallinity, analyze, investigate stability, and assess gas sorption properties. The primary techniques used for these purposes are explained below.

X-ray diffraction (XRD)

Understanding the spatial arrangement of atoms in PIP is essential for comprehending their sorption properties, making X-ray diffraction the most important tool in this master's thesis. Single-crystal X-ray diffraction (SC-XRD) is the most straightforward method for determining new structures, but its use is limited by the availability of suitable single crystals. An effective alternative is powder X-ray diffraction (PXRD), which, although more complex for solving unknown structures, allows for the easy identification of known phases. Consequently, PXRD can be used to verify synthesis reproducibility and assess sample purity. Additionally, PXRD is useful for monitoring structural transformations, evaluating stability and following pore filling under various conditions (e.g., varying temperature, pressure) through *in situ* experiments. These experiments provide insights into sorption mechanisms, host-guest interactions, and allow for the quantification of sorption through subsequent refinement.

Nuclear magnetic resonance (NMR)

Solution ^{1}H- and ^{11}B-nuclear magnetic resonance (NMR) spectroscopies are valuable methods for identifying and assessing the purity of PIP compounds. The ^{1}H-NMR spectra of the dissolved PIP show signals corresponding to the organic cation used, as well as any remnants of the reaction solvent. The ^{11}B-NMR spectroscopy enables the identification of reaction intermediates and helps determine when the formation of the $[B_{12}H_{12}]^{2-}$ anion is complete. Quantitative analysis of the spectra allows for the determination of the relative stoichiometry of the ions with the remnants of the reaction solvent. However, quantification is not always possible. For example, if the relaxation times (T_1) of nuclei are not properly accounted for, some signals may not fully relax between pulses, leading to inaccurate

integration. Additionally, if the pulse repetition time is too short, signals may become saturated, causing deviations from true quantitative value.

Attenuated total reflectance Fourier transform infrared spectroscopy (ATR-FTIR)

ATR-FTIR provides insights into the chemical composition of the PIPs and can qualitatively probe for the presence of guests inside the pores. Additionally, the spectral infrared absorption bands offer valuable information about bonding interactions and potential guest-host interactions, such as dihydrogen and hydrogen bonds.

Neutron powder diffraction (NPD)

Neutron diffraction provides unique insights, particularly regarding hydrogen sorption. It utilizes the large neutron coherent cross section of deuterium (D_2) gas to locate the hydrogen sorption sites. When combined with XRD techniques, it enhances our understanding of the microscopic picture of chemical interactions.

1.3.2. Stability

Thermogravimetric – differential thermal analyses (TG-DTA)

Thermal stability, guest release, and decomposition behavior of PIPs can be assessed using TGA. This technique involves subjecting a sample to a controlled temperature program and recording weight changes. Successive weight losses typically correspond to the release of solvents or guest molecules, followed by PIP decomposition. The temperatures at which these losses occur, intensity of the latter, and the shape of the thermograms provide information on stability and the amount of guests released. This analysis can be complemented by examining the solid residue with PXRD.

Coupling TGA with DTA helps differentiate between endothermic events accompanied by mass loss (guest release) and exothermic events accompanied by mass loss (PIP decomposition). Additionally, DTA can detect temperature-induced phase transitions.

1.3.3. Sorption properties

Volumetric gas sorption

Volumetric gas sorption allows the determination of the amount of gas sorbed by a material as a function of pressure and/or temperature. In this method, the sample is exposed to a known gas pressure. There are two volumes: one containing the sample and the other with gas at a specified pressure. Opening the valve between these volumes allows the determination of the sorbed gas quantity by measuring the equilibrium pressure. This technique provides valuable information about the sorption capacity, and storage performance of PIP for gases such as H_2 and CO_2. Volumetric gas sorption experiments can be conducted over a wide range of temperatures and pressures, enabling studies of gas sorption kinetics and thermodynamics, the impact of temperature on sorption behavior, and whether the voids are interconnected based on the type of isotherm observed.[73]

Dynamic vapor sorption (DVS)

To analyze the vapor sorption properties of PIPs, DVS is a powerful technique. It involves recording the mass change associated with gas or vapor molecules sorbed or desorbed by the sample as a function of time or relative humidity. This technique provides insights into the sorption mechanisms and kinetics, enhancing our understanding of PIPs' sorption behavior. Factors such as pore size significantly influence vapor sorption in porous materials. DVS data for PIPs is collected as mass changes relative to humidity at a fixed temperature, yielding a water sorption isotherm. Hysteresis curves, often observed, can be attributed to slow desorption kinetics due to restricted diffusion, which hinders the efficient release of water molecules from the material's pores.

1.4. Dodecaborates

1.4.1. Boron chemistry and synthesis

Boron has three valence electrons and a ground state electron configuration of $1s^2 2s^2 2p^1$. Typically, boron forms trivalent neutral compounds such as boron trifluoride (BF_3), in which boron has six valence electrons. In these compounds, boron is sp^2 hybridized, possesses an

empty p-orbital, and exhibits a trigonal planar geometry. These compounds are electron-deficient due to the empty p-orbital on boron and are isoelectronic with carbocations. Additionally, boron can form negatively charged tetravalent compounds, such as BH_4^-, which adopt a tetrahedral geometry. Unlike boranes, which are strong Lewis acids, borohydrides are nucleophilic.

Borohydrides have garnered significant attention as potential solid-state hydrogen storage materials.[74,75] Recently, our group discovered the porous γ-$Mg(BH_4)_2$, which can sorb up twice the density of liquid H_2 (144 g/L compared to 71 g/L).[76] The hydridic hydrogens in this compound seem to stabilize the H_2 guests within its framework, leading to the development of other promising compounds. However, the low stability of BH_4^- ions, both electronically and upon exposure to water, poses challenges for gas sorption and other applications.[77] Listed below are the decomposition reactions of borohydrides (equations 1-3):

$$BH_4^- + 8\ OH^- \rightarrow BO_2^- + 6H_2O + 8e^- \ (E^\circ = -\ 1.24\ V\ vs\ SHE) \quad (1)$$

$$BH_4^- + H_2O \rightarrow BH_3(OH)^- + H_2 \quad (2)$$

$$BH_3(OH)^- + H_2O \rightarrow BO^{2-} + 3\ H_2 \quad (3)$$

We aimed to retain the hydridic nature of the B-H bond while seeking more stable compounds. This led us to focus on boron clusters, here taking $[B_6H_6]^{2-}$ as an example to showcase the extraordinary stability of those compounds. To understand this phenomenon, it is essential to first examine the valence orbitals of boron, which consist of one s orbital and three p orbitals. The s and p_z orbitals of boron lead to the formation of two sp hybrid orbitals.[78] In the $[B_6H_6]^{2-}$ anion, there are a total of 24 valence orbitals (1s + 3p per boron), divided into 12 sp, 6 p_x, and 6 p_y orbitals. The sp orbitals possess the appropriate symmetry to bond with the s orbitals of hydrogen, resulting in six σ-bonds with hydrogen atoms. The remaining six sp orbitals point towards the center of the octahedron, leading to significant overlap and forming a bonding orbital with A_{1g} symmetry, which greatly stabilizes the core structure. Additional stabilization arises from the interactions between the six sp orbitals and the 12 p orbitals (T_{1u} symmetry), and further from the overlap of the p orbitals (T_{2g} symmetry).[79] *Figure 8* summarizes these stabilizing interactions.[78]

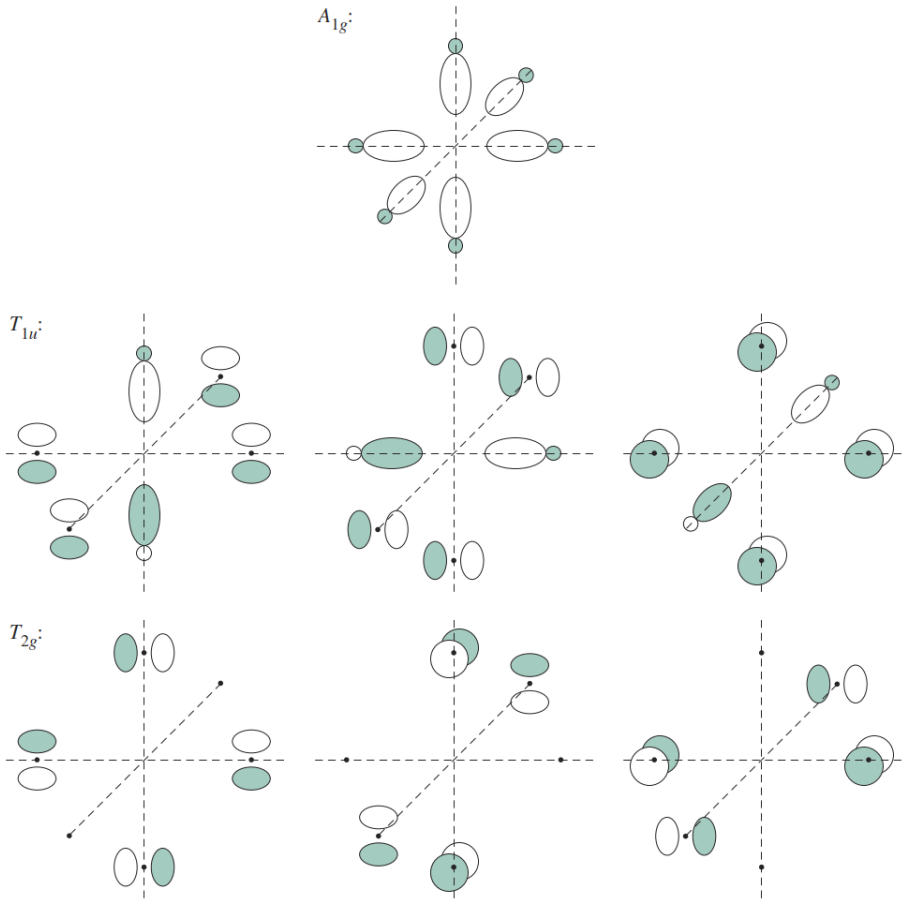

Figure 8. Bonding in $[B_6H_6]^{2-}$. Scheme taken from reference 74.

Counting the bonding orbitals, we obtain six orbitals bonded to hydrogens, three bonding orbitals from sp, p_x, and p_y overlaps (T_{1u}), three from p_x and p_y interactions (T_{2g}), and one directed towards the center with A_{1g} symmetry, totaling 13 bonding orbitals out of 24. The remaining orbitals are either non-bonding or anti-bonding. Boron's electronic configuration is [He] $2s^2$ $2p^1$, and hydrogen's is $1s^1$, giving four valence electrons for each B-H pair. This results in 24 electrons for 13 bonding orbitals. Following Pauli's exclusion principle, two electrons per orbital leave one empty bonding orbital, explaining the two excess negative charges in *closo*-borates. This logic, applied to $[B_6H_6]^{2-}$, holds for all *closo*-borates up to 12 boron atoms. Using the general formula $[B_nH_n]^{2-}$, there are 2n+1 bonding orbitals: n+1 supporting the structure and n bonded with hydrogens (*Figure 9*).

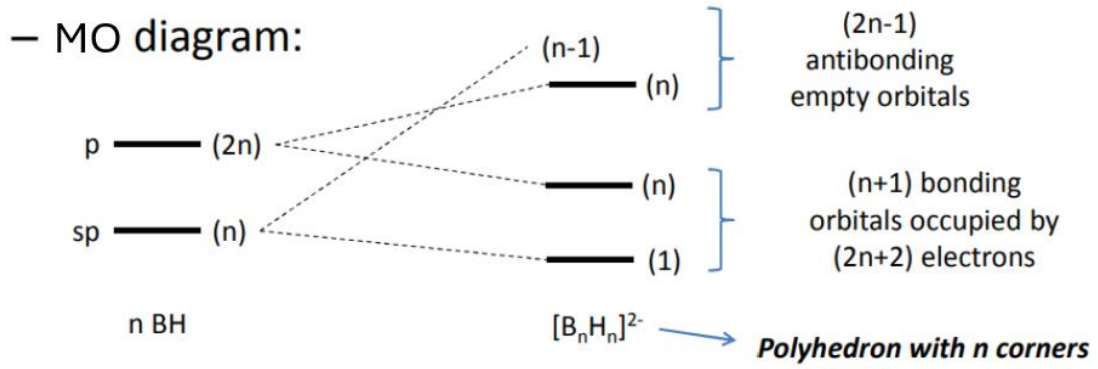

Figure 9. Scheme of the molecular orbital (MO) of the $[B_nH_n]^{2-}$ compounds for n between 6 to 12.

It is noteworthy that the closer the B-H cage symmetry is to spherical, the greater the compound's stability.[80] The icosahedral $[B_{12}H_{12}]^{2-}$ is thus the most stable among *closo*-borate structures.[81] This high stability (thermal, electronic and with respect to hydrolysis) makes it particularly relevant for study in the context of gas sorption.

However, *closo*-dodecaborates are tricky to synthesize in pure form due to the numerous intermediates involved. The reaction proceeds through a sequence of boron fusion and dehydrogenation steps, gradually increasing the boron content, starting with the borohydride, and ending with the dodecaborate. The primary mechanism for buildup involves the addition of BH_4^-/BH_3 species followed by the loss of H_2 or H^-. Once the cluster reaches 3-5 boron atoms, larger fusion reactions predominate, again followed by the loss of H_2 or H^-, and subsequent structural rearrangements.[82] The known intermediates in the synthesis of $[B_{10}H_{10}]^{2-}$ are shown in *Figure 10*, with those experimentally observed circled in red.[83] Consequently, synthesizing pure $[B_{12}H_{12}]^{2-}$ in sufficient yield can be challenging.

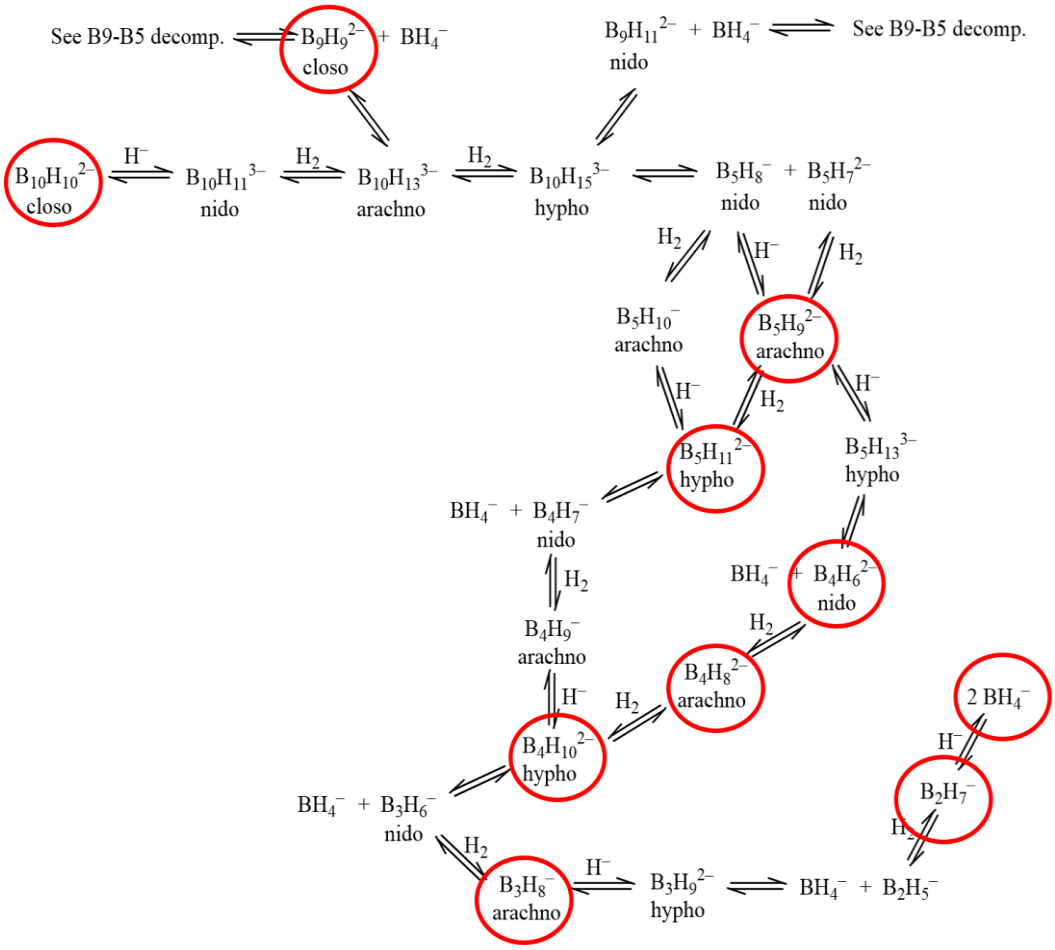

Figure 10. Intermediates involved in the formation of $[B_{10}H_{10}]^{2-}$ starting from BH_4^-. The encircled intermediates have been isolated experimentally. Scheme taken from reference 77.

1.4.2. Alkali metal dodecaborates

There are numerous reported methods for synthesizing $M_2[B_{12}H_{12}]$ (M = Li, K, Na), each with its own advantages and disadvantages. One constant is the use of glymes as solvents, as this solvent family uniquely solubilizes the borohydride and all the reaction intermediates described in the previous section, except for the final product $[B_{12}H_{12}]^{2-}$.[84,85] The main methods for synthesizing dodecaborates are summed up in *Figure 11*.[86]

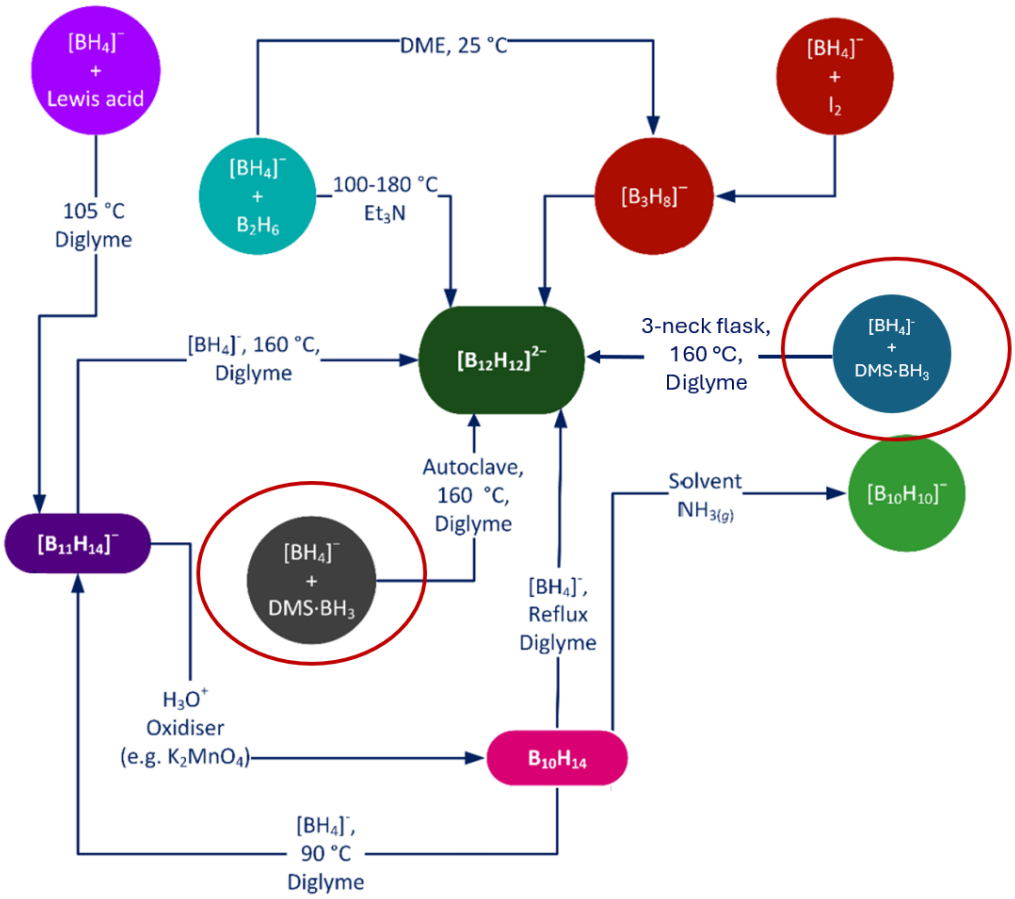

Figure 11. Scheme depicting the main methods for synthesizing $[B_{12}H_{12}]^{2-}$. The methods developed by our research group are encircled in red. DME = monoglyme. This scheme is adapted from reference 87.

The first method involves the reaction of borohydrides with neutral boranes (B_2H_6 or $B_{10}H_{14}$). Given the increasing emphasis on green chemistry, the use of toxic and expensive compounds such as B_2H_6 and $B_{10}H_{14}$ should be avoided whenever possible.[87] The second method is a two-step synthesis that relies on the oxidation of borohydrides by iodine. This route can be made cost-effective and specific, but the yield is not high (around 50 %).[88] The third method, developed by our group, offers two new and convenient one-pot synthesis of sodium and alkali metal dodecaborates (Li^+, Na^+, and K^+) from their respective borohydrides and the borane dimethyl sulfide complex ($DMS{\cdot}BH_3$) in an autoclave or a three-necked round bottom flask.[89,90] This method appears to be the most straightforward and has been refined in our laboratory.

1.4.3. Organic dodecaborates

The ion exchange reaction in water between $Na_2B_{12}H_{12}$ and tetramethylammonium bromide $(NMe_4)_2B_{12}H_{12}$ led to the synthesis of an organic dodecaborate salt, tetramethylammonium dodecaborate (TMAD), marking our group's first PIP discovery. SC-XRD revealed large, interstitial voids in a crystal lattice of the *fcc* anti-CaF_2 type mentioned in section *1.2.3,* between the $[NMe_4]^+$ and $[B_{12}H_{12}]^{2-}$ ions (*Figure 12*). The voids have a volume of 129 $Å^3$, accounting for 5.4 % of the total unit cell volume, a 69 % increase compared to $Cs_2B_{12}H_{12}$. Although the voids in this compound appear isolated, the rotational dynamics of the $[NMe_4]^+$ and $[B_{12}H_{12}]^{2-}$ ions in the solid state may enable guest molecule diffusion.

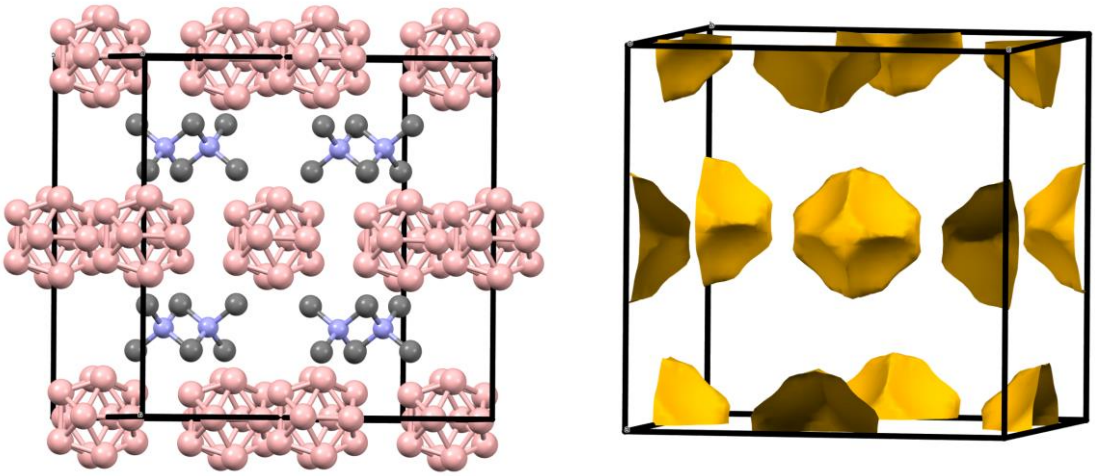

Figure 12. Crystal structure of TMAD (without hydrogens for clarity) on the left and the solvent accessible voids on the right. Color code: B = pinkish, N = blue, C = grey, voids = yellow.

1.5. Research objectives

This master's thesis will focus on three distinct main objectives:

1) Understanding the formation of TMAD and optimizing its synthesis.
2) Exploring the versatility of the PIP concept by modifying the ions to synthesize additional PIPs with different properties.
3) Investigating gas sorption in the PIPs using volumetric and diffraction methods.

Each of these objectives is described in more detail below.

The **first objective** is to further investigate the formation of TMAD, the first PIP synthesized by our group. A key focus will be optimizing the synthesis, as this reaction originates from our group and has not been extensively performed. To achieve this, we will first optimize the synthesis of $Na_2B_{12}H_{12}$ from the reaction of $NaBH_4$ with $DMS{\cdot}BH_3$, by varying the reaction conditions. Following this, we will attempt the ion exchange in water, between the synthesized $Na_2B_{12}H_{12}$ and the NMe_4Br, under various conditions to determine if the yield varies and if different phases are obtained. Moreover, TMAD will be fully characterized by the techniques described in the characterization section.

The **second objective** is to determine whether the PIP concept is broadly applicable or if TMAD is unique. To test this, we will replace the cation NMe_4^+ with its larger phosphorus-containing analog, PMe_4^+. Various reaction conditions will be evaluated to identify the optimal synthesis parameters for this new PIP, since we found an additional polymorph. This compound will be thoroughly characterized using the techniques described in the methodology section. Given the similarity between the cations, we expect this new compound to form a similar *fcc* crystal lattice as TMAD, but with larger pores, and to be capable of gas sorption.

Additionally, we will attempt to synthesize a PIP using a less symmetrical cation, *t*-$BuNH_3^+$. Structurally similar to NMe_4^+, this cation differs by exchanging one of the methyl group carbons with the nitrogen. This change has two main effects: (i) it localizes the charge more on the nitrogen, whereas in NMe_4^+ the charge is delocalized over the entire tetrahedron, and (ii) it reduces steric hindrance around the nitrogen, as *t*-$BuNH_3^+$ has one *t*-butyl group and three hydrogens instead of four methyl groups. These differences could lead to unique interactions and potentially novel properties.

We will also attempt to replace the $[B_{12}H_{12}]^{2-}$ anion with a less symmetrical anion, $[SnCl_4Br_2]^{2-}$, while retaining the NMe_4^+ cation. We are aware that $[NMe_4]_2SnCl_6$ forms a *fcc*-type structure similar to TMAD, and we anticipate that $[NMe_4]_2SnCl_4Br_2$ would be isostructural. We will investigate how the reduced symmetry of the anion affects sorption kinetics, expecting it to yield interesting properties.

The **third objective** will aim to assess the gas sorption properties of all the PIPs synthesized, utilizing the volumetric and diffraction methods described in the characterization

section. We will analyze the results of each PIP to understand the impact of ion symmetry. Additionally, we will compare these outcomes with the gas sorption results from the non-interconnected voids of $Cs_2B_{12}H_{12}$. This will allow us to determine the most promising PIP materials for further development and potential applications.

Furthermore, we will investigate the relationship between the structural features of the PIPs, such as pore size, shape, and connectivity, and their gas sorption performance. We will employ advanced characterization techniques like *in situ* XRD and neutron powder diffraction to elucidate the dynamic behavior of guest molecules within the PIP frameworks during sorption and desorption processes. We will employ Rietveld refinement to locate guest molecules inside the PIP pores.

2. Experimental methodology

2.1. Chemicals

Solid reagents:

- $NaBH_4$: ≥ 98.0 %, Sigma-Aldrich
- $Na_2B_{12}H_{12}$: ≥ 98.0 %, Katchem
- NMe_4Br : 98 %, Thermo Fisher Scientific
- PMe_4Br : 98.0 %, Thermo Fisher Scientific
- $Cs_2B_{12}H_{12}$: ≥ 98.0 %, Katchem
- $SnCl_4 \cdot 5H_2O$: ≥ 98 %, Thermo Scientific Chemicals

Liquid reagents:

- C_7H_7Cl : 99 %, Sigma-Aldrich
- $DMS \cdot BH_3$: 10-10.2M MilliporeSigma

Solvents:

- $C_6H_{14}O_3$: 99.5 %, anhydrous, Sigma-Aldrich

NMR Solvents

- Dimethylsulfoxide-d_6 : 99.8 % D, Eurisotop

Gases:

- CO_2 : ALPHAGAZ 1, Air Liquide
- Ar : ALPHAGAZ 1, Air Liquide
- Xe : ALPHAGAZ 1, Air Liquide

<u>Note:</u> For some experiments, diglyme underwent purification before use, through the addition of solid sodium into the bottle containing the solvent, followed by the extraction of the supernatant by simple decantation. All other reagents were used as received, without prior purification.

2.2. Synthesis

2.2.1. $Na_2B_{12}H_{12}$

The following procedure to obtain sodium dodecahydrododecaborate ($Na_2B_{12}H_{12}$) is adapted from Wang et al.[89] First, it should be emphasized that this reaction poses a serious hazard, requiring utmost caution to ensure safety. Specifically, the involvement of B_2H_6 as an intermediate makes it particularly dangerous, as B_2H_6 is a pyrophoric gas. Simultaneously, H_2 is produced, rendering the reaction potentially explosive.

$NaBH_4$ (0.380 g, 10 mmol) was weighed and added to a 100 mL three-neck round-bottom flask within an argon filled glovebox. The flask was then sealed with rubber septa before being removed from the glovebox. The septum on the middle neck of the flask was quickly exchanged by a condenser and three cycles of vacuum and argon flushes were performed immediately, ensuring that the system remained airtight during the process. Subsequently, 20 mL of diglyme were added to the solid. An empty balloon was placed on top of the condenser, to account for volume expansion during the reaction. The solution was then heated to 80°C and 5.2 mL (52 mmol) of borane dimethyl sulfide complex ($DMS{\cdot}BH_3$) was added to the solution under vigorous stirring (500 rpm). Bubbles started appearing immediately and the initially colorless solution turned yellow after approximately 10 minutes. The temperature was then further increased to 160 °C. During the first hour of reaction, the balloon fitted on top of the condenser was emptied about every 10 minutes to avoid excessive pressure buildup (from DMS and H_2, which are both gases under the reaction conditions). The reaction mixture was then left to stir further at 160 °C for 24 hours and was subsequently cooled down to room temperature. The solution was then placed in the fridge (4°C) for an additional 12 hours. The solid product was filtered using a P3 sintered glass filtration funnel and washed with diglyme (3x5 mL). The solid was finally dried for one day at RT, yielding a white powder. Yield of $Na_2B_{12}H_{12}{\cdot}4$ diglyme: 3.36 g (93 %) = 4.6 mmol.

2.2.2. $(NMe_4)_2B_{12}H_{12}$

The following procedure to obtain tetramethylammonium dodecahydrododecaborate (TMAD) is adapted from a protocol developed in our group.[89] NMe_4Br (0.68 g, 4.4 mmol) and $Na_2B_{12}H_{12}{\cdot}4$diglyme (1.58 g, 2.2 mmol) were separately dissolved in the least possible amount

of cold demineralized water (stored in a fridge at 4°C) to achieve complete solubilization, making solutions of about 2 mL and 7 mL respectively. The two solutions were subsequently mixed together, which led to the immediate formation of a white precipitate. After 10 minutes, two phases could be observed: a small phase consisting of mainly diglyme on top and an aqueous phase with TMAD suspended within in the bottom, with the precipitate being lighter than water (*Figure 13*). The mixture was then filtered using P3 sintered glass filtration funnel and washed using 3x5 mL of deionized water (RT). The obtained fine white powder was dried under vacuum for about 6 hours. Yield of TMAD: 0.39 g (61 %).

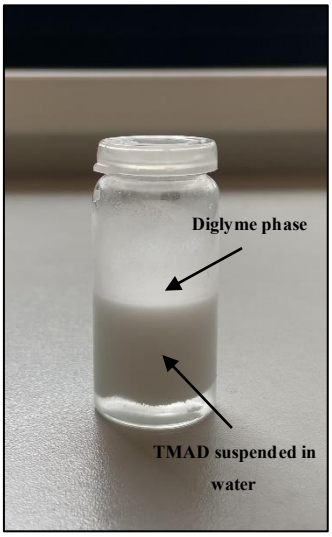

Figure 13. Vial containing the suspension of TMAD in water.

The same procedure was applied using commercial $Na_2B_{12}H_{12}$, or alternatively $Na_2B_{12}H_{12}\cdot 4H_2O$ (0.08 g, 0.3 mmol) instead of $Na_2B_{12}H_{12}\cdot 4$diglyme. $Na_2B_{12}H_{12}$ (0.06 g, 0.3 mmol) and NMe_4Br (0.09 g, 0.6 mmol) were separately dissolved in 0.5 mL of deionized water. The two solutions were subsequently mixed, and a white precipitate was obtained. The mixture was put to the fridge (4°C) for an hour, leading to the formation of a biphasic mixture consisting of diglyme on top and TMAD suspended in water at the bottom. The precipitate was then washed with 3x5 mL of deionized water, and the resulting powder was dried under vacuum for 4 hours. Yield of TMAD: 0.05 g (58 %) = 0.17 mmol.

2.2.3. $(PMe_4)_2B_{12}H_{12}$

The following procedure to obtain tetramethylphosphonium dodecahydrododecaborate (TMPD) is adapted from the protocol described in section *1*. PMe_4Br (0.47 g, 2.7 mmol) and $Na_2B_{12}H_{12}\cdot 4$diglyme (0.99 g, 1.4 mmol) were separately dissolved in the least possible volume of cold water (at about 4°C) to achieve complete solubilization; roughly 2.5 mL and 7 mL, respectively. The two solutions were then mixed together, and a white precipitate appeared instantly. After 10 minutes in the fridge, the same two phases described in the *Figure 13* could be observed. Subsequently, the precipitate was filtered using a P3 sintered glass filtration funnel and washed using 3x5 mL of deionized water. The resulting powder was then left to dry under vacuum for about 6 hours. Yield of TMPD: 0.29 g (66 %) = 0.9 mmol.

The same method was applied with commercial $Na_2B_{12}H_{12}$ (0.02 g, 0.1 mmol), instead of $Na_2B_{12}H_{12}$·4diglyme, and PMe_4Br (0.03 g, 0.2 mmol), separately dissolved in 0.5 mL of cold deionized water (4°C). The solutions were subsequently mixed, and immediately, a white precipitate formed. The same two phases described in section *2.2.2* appeared. The mixture was cooled to the fridge (4°C) for about an hour. The solid was filtered using a P3 sintered glass filtration funnel and subsequently washed with deionized water (3 x 5 mL) and dried for 4 hours. Yield of TMPD: 0.02 g (61 %) = 0.06 mmol.

2.2.4. Crystals of (*t*-$BuNH_3)_3B_{12}H_{12}$·H_2O for XRD

The following procedure to obtain *tert*-butylammonium dodecahydrododecaborate monohydrated is adapted from the protocol described in section *1*. The reagent, *t*-$BuNH_3Br$, obtained from the reaction between *t*-butylamine and *t*-butylbromide, was readily available in the lab (synthesized by a coworker). $Na_2B_{12}H_{12}$·4diglyme (0.51 g, 0.7 mmol) and *t*-$BuNH_3Br$ (0.21 g, 1.4 mmol) were separately dissolved in 1 mL and 7 mL of cold deionized water (about 4°C), respectively. The two solutions were subsequently mixed and heated to 100 °C until the evaporation of 7 mL of water. The solution was then placed in the fridge (4 °C) for 10 days. A few white single crystals suitable for single crystal XRD analysis were recovered.

2.2.5. $(NMe_4)_2SnCl_{4.7}Br_{1.3}$

NMe_4Br (3.82 g, 25 mmol) and $SnCl_4·5H_2O$ (4.35 g, 12 mmol) were separately dissolved in water (previously cooled in the fridge at 4°C). The solutions were subsequently mixed, leading to a slow formation of big white crystals. Those were recovered for subsequent SC-XRD measurement. The solution was then put back to the fridge for an additional 14 days. The white solid was then filtered and washed using 3x5 mL of deionized water. The white flakes were then left to dry for about one day, under air. Yield of $(NMe_4)_2SnCl_{4.7}Br_{1.3}$: 4.00 g (62 %) = 7.4 mmol.

2.3. Instruments for characterization

Powder X-Ray diffraction (PXRD) analyses were performed using a MAR345 diffractometer with X-rays generated by an Incoatec Microfocus Source ($I\mu S^{High\ Brillance}$) Mo ELM47 operating at 50 kV and 1000 µA (λ = 0.71073 Å). Powdered samples were loaded in glass capillaries (0.7 mm, Hilgenberg GmbH). For *in situ* analyses, the samples were placed in

a capillary and pressurized using a home-made gas dosing system made from Swagelok parts (*Figure 14*) equipped with a Keller Control center Serie 30 interface for monitoring the pressure up to 10 bar (higher pressures might result in explosion of the capillary). Temperature control was achieved using a Cryostream 700 temperature regulator (Oxford Cryosystems). For the *in situ* measurements involving temperature variation during the scans, we employed the following method: initially, the temperature was set to 300 K and maintained for approximately 10 minutes before the measurements began. Subsequently, a ramp rate of 42 K per hour was applied, gradually increasing the temperature from 300 K to 400 K. Data collection involved 20 scans, each lasting 5 minutes, with an acquisition time of approximately 2 minutes per scan (one pattern every 7 minutes, meaning every 5 K). Diffraction data were integrated using the Fit2D software (a 0.3 mm diameter capillary filled with LaB_6 was used as a calibrant) and analyzed using the FullProf suite.[92,93] It underwent further processing with the addsigma software, enabling the conversion from .chi to .dat format. The resulting files were then visualized using the Medved software.[94] Rietveld refinement was performed using the FullProf suite. The visual representation of the crystal structures was generated using the software Mercury 4.0.[95]

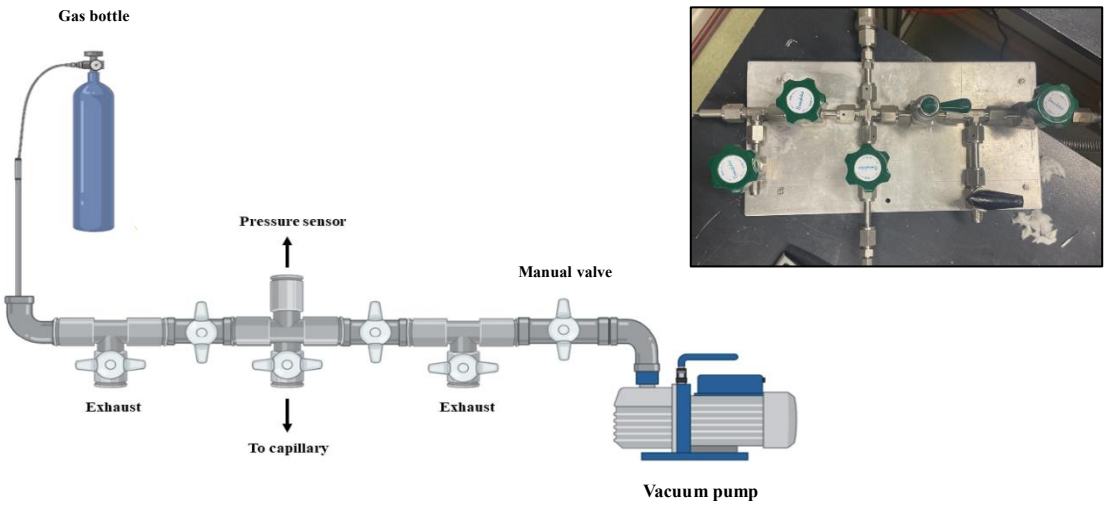

Figure 14. Gas dosing system used for *in situ* PXRD experiments under gas pressure (realized using the website Biorender). A picture of the system made from Swagelok parts is shown in the upper right corner.

Single crystal X-Ray diffraction (SC-XRD) data was acquired on a MAR345 image plate detector using Mo K_α radiation (λ = 0.71073 Å), generated by an Incoatec iSG250 source,

operating at 50 kV and 600 μA, equipped with Montel mirrors. Crystals were measured at ambient temperature or flash cooled to 150 K in a nitrogen gas stream (using a 800 Series Cryostream cooler). Data indexation, integration and reduction was done with CrysAlis^{PRO}, incorporating an empirical absorption correction. Structures were solved by dual space direct methods (SHELXT), followed by refinement using full-matrix least squares based on $|F^2|$ with SHELXL 2014/7.[96] Non-hydrogen atoms were anisotropically refined, while hydrogen atoms were positioned at calculated positions and refined in riding mode, with temperature factors constrained to 1.2 times Ueq of the parent atoms (1.5 times Ueq for methyl hydrogens).

Neutron diffraction experiments were performed at the Institut Laue-Langevin (ILL) in Grenoble at the D20 instrument, a medium to high resolution two-axis diffractometer capable of producing a neutron flux of 10^8 s^{-1} cm^{-2} at the sample position.[97] A wavelength of 1.54 Å was used for the experiment, using a germanium monochromator (115) for higher take-off angles. Measurements were carried out at 0.05° intervals within the detector range of 9° to 6°, resulting in a 20-minute exposure for the sample. The probed range of 2θ extended from 5° to 150°. The sample was inserted between two sheets of aluminum foil, subsequently rolled in a cylindrical shape before being introduced into a sample container of 8 mm of diameter made in aluminum. The sample contained was then affixed to a sample stick specifically designed to allow measurements under gas pressure. The stick was then placed inside an Orange Cryostat.[98] Activation of the sample was performed at 400 K, followed by the introduction of 9.6 bar of D_2 into the setup by using an IMI-HTP Sievert's apparatus from Hiden Isochema dosage system. Subsequently, the system was gradually cooled down to 77 K, while regularly adding D_2 gas to maintain a pressure around 10 bar.

Nuclear magnetic resonance (NMR) spectra were acquired using a Bruker Avance 500 or a Jeol JNM-ECZL G series spectrometer. The Bruker Avance 500 spectrometer (^{1}H: 500.13 MHz, ^{11}B: 160.46 MHz) was equipped with a BBO {^{1}H, X} probe head and a *z*-gradient coil, operating at room temperature. The experiments were controlled using the TopSpin 1.3 software (Bruker). The JEOL JNM-ECZL G series spectrometer operates at 600.09 MHz for ^{1}H and 192.56 MHz for ^{11}B. Experiments were conducted using a 5 mm HFX probe equipped with a *z*-gradient coil and data was acquired using the Delta 6.2 software (JEOL). Solid samples were dissolved in deuterated DMSO-d_6, and filtrates were diluted in the same solvent. Quartz NMR tubes (Norell, S600 QTZ) with a 5 mm internal diameter were used for sample containment. The spectra were treated using the MestReNova (version 14.1.0-24037) software.[99] ^{1}H chemical

shifts were referenced to the residual peaks of the deuterated solvent (δ = 2.50 ppm for DMSO-d_6). The splitting patterns in the NMR spectra were reported as *s* = singlet, *d* = doublet, *t* = triplet, and *m* = multiplet.

Thermogravimetric – differential thermal analyses (TG-DTA) under nitrogen were performed on a Mettler Toledo TGA/DSC 3+ STAR^e System. Samples were placed in a 70 µL alumina crucibles, nitrogen gas flow of 100 mL/min and heating rates of 5°C/min were used up to 400 or 500°C for the analyses.

Attenuated total reflectance Fourier transform infrared (ATR-FTIR) spectra were obtained using a Bruker Alpha spectrometer equipped with a Platinum ATR module (Bruker, diamond crystal, single bounce) housed in an argon-filled glovebox. Each spectrum was recorded within the 370-4000 cm^{-1} range at a resolution of 4 cm^{-1}, averaged over 96 scans.

Dynamic vapor sorption (DVS) measurements were performed on a TA Instruments Q5000SA. The samples were pretreated at 25°C under a relative humidity of 10 % until equilibrium was attained. Equilibrium conditions were set as a rate of weight change inferior to 0.1 wt.%/5 min; alternatively, the next step was initiated if those conditions were not attained after 60 min. The weight change was then recorded isothermally at 25°C in steps of 2.5 % RH, up to 90 % RH for sorption, and then back to 10 % for desorption.

X-Ray fluorescence (XRF) analysis was performed using a SPECTRO XEPOS C (SPECTRO Analytical Instruments) spectrometer operating at 50 kV with a direct excitation and a HAPG polarizer. The samples were prepared using Ultra High Precision model XRS-24-32 cups which were then introduced in the spectrometer with no further treatment.

Volumetric gas sorption experiments were performed on an IMI-HTP Sievert's apparatus from Hiden Isochema. For the experiments, 100 to 200 mg of sample were used. Approximately 0.02 cm^3 of carefully weighed displacer (Thermal Ceramics Cerafiber type 520 quartz wool) was added on top of the sample to secure it into the pre-weighed reactor. The sample was then activated under vacuum at 100°C (heating rate of 10°C/min) for 10 hours before prior to the sorption measurement. The excess uptake values (originally in µmol) were subsequently converted to µmol/g of dry sample, based on the sample's weight after activation (determined by weighing the filled reactor immediately after the experiment).

3. Results and discussion

3.1. Inorganic dodecaborates

3.1.1. $Na_2B_{12}H_{12}$

Sodium dodecaborate was obtained through the following reaction (4):

$$2\ NaBH_4 + 10\ DMS{\cdot}BH_3 \rightarrow Na_2B_{12}H_{12} + 10\ DMS + 13\ H_2 \quad (4)$$

It is important to highlight that a significant amount of H_2 and $DMS{\cdot}BH_3$ gases were generated during the first step of the reaction, which is leading to the intermediate $[B_{11}H_{14}]^-$, following this equation (5):

$$NaBH_4 + 10\ DMS{\cdot}BH_3 \rightarrow NaB_{11}H_{14} + 10\ DMS + 10\ H_2 \quad (5)$$

This claim is further supported by the ^{11}B-NMR spectrum of the reaction solution (***A1***). The $NaB_{11}H_{14}$ subsequently reacts with $NaBH_4$, leading to the formation of $Na_2B_{12}H_{12}$ (6):

$$NaBH_4 + NaB_{11}H_{14} \rightarrow Na_2B_{12}H_{12} + 3\ H_2 \quad (6)$$

A series of experimental conditions were explored in pursuit of achieving the highest feasible yield, the parameters that were varied during those trials are reported in *Table 2*.

Table 2. Experimental conditions used for the optimization of the synthesis of $Na_2B_{12}H_{12}{\cdot}4$diglyme.

Entry	Excess $DMS{\cdot}BH_3$ (%)	Volume of the flask (mL)	Temperature (°C)	Yield (%)
A	10	100	160	0
B	10	100	170	0
C	10	100	180	0
D	10	100	150	0
E	0	100	160	43
F	2	100	160	67

G	4	100	160	93
H	4	100	160	91
I	4	250	160	14

Initially, the reaction was conducted according to the methodology previously developed in our lab,[90] employing a 10 % excess of $DMS{\cdot}BH_3$ (5.5 mL, 55 mmol). These attempts were unsuccessful, resulting in the absence of precipitate and the generation of degradation products that are soluble in diglyme. Subsequent adjustments involved variations in reaction temperature while maintaining the 10 % excess, all of which yielded negative outcomes. The $DMS{\cdot}BH_3$ excess has been modified, keeping the temperature constant, improving the yield to 43 %, 67 % and 93 % using 0 %, 2 % and 4 % excess, respectively. Additionally, it was observed that utilizing identical conditions in either 100 mL or 250 mL flasks yielded a consistent yield around 91-93 % in the former case and only 14 % yield in the latter case. This underscores the importance of the flask volume, relative to the volume of the reaction mixture, on the outcome of the synthesis.

The resulting optimized parameters for the synthesis of $Na_2B_{12}H_{12}$ are: the use of a 100 mL three-necked flask containing 20 mL of diglyme, 0.38 g of $NaBH_4$ (10 mmol), and 5.2 mL of $DMS{\cdot}BH_3$ (52 mmol) at a reaction temperature of 160°C for a duration of 24 hours. The results furthermore demonstrate that the synthesis process to obtain $Na_2B_{12}H_{12}$ is highly responsive to various parameters, such as minor changes in temperature, stoichiometry and even the volume of the three-neck round-bottom flask.

Due to the use of diglyme, and considering its coordinating nature, unsolvated $Na_2B_{12}H_{12}$ is not obtained directly from the synthesis as shown by powder X-ray diffraction in *Figure 15*. However, the experimental powder pattern bears no resemblance to the theoretical pattern of $Na_2B_{12}H_{12}{\cdot}4$diglyme. It must be emphasized that the crystal structure used to calculate the theoretical pattern was solved from a single crystal measured at 150K while the powder was measured at RT. This may result in a change in the crystal lattice between the two samples and consequently alter the diffraction pattern significantly. Additionally, this analysis also demonstrated the absence of unsolvated $Na_2B_{12}H_{12}$ in the obtained sample.

^{1}H- and ^{11}B-NMR were performed to confirm the purity of the compound. The spectra are depicted in *Figure 16* and ***A2,*** respectively. Analysis of the ^{1}H-NMR spectrum of the synthesized $Na_2B_{12}H_{12}$ further confirms the incorporation of diglyme in the compound,

indicated by signals at 3.38 (*t*), 3.42 (*t*) and 3.20 (*s*) ppm (3.33 ppm is the water peak). Integrating the signals gives a ratio of 5.96 diglyme to $Na_2B_{12}H_{12}$. As NMR spectra can pose quantification problems (see *section 1.3.1*), a TGA was carried out to check the solvation rate of the sample. The signal at -16.5 ppm (*s*) on the ^{11}B-NMR spectrum (***A2***) serves as further evidence for the successful formation of $[B_{12}H_{12}]^{2-}$, with however some trace impurities of $[B_{11}H_{14}]^-$ and $[B_3H_8]^-$ indicated by signals at -18.5 (*d*) and -29.5 (*s*) ppm, respectively.

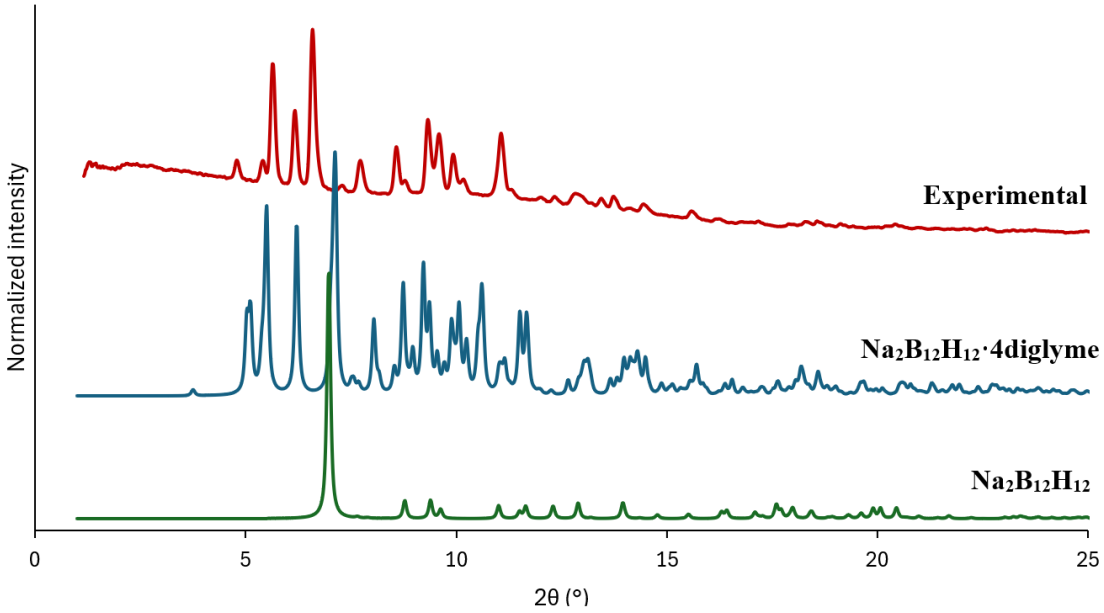

Figure 15. X-ray powder diffraction patterns of the as-synthesized sample and simulated theoretical patterns of $Na_2B_{12}H_{12}$ and $Na_2B_{12}H_{12}$·4diglyme (entry G).

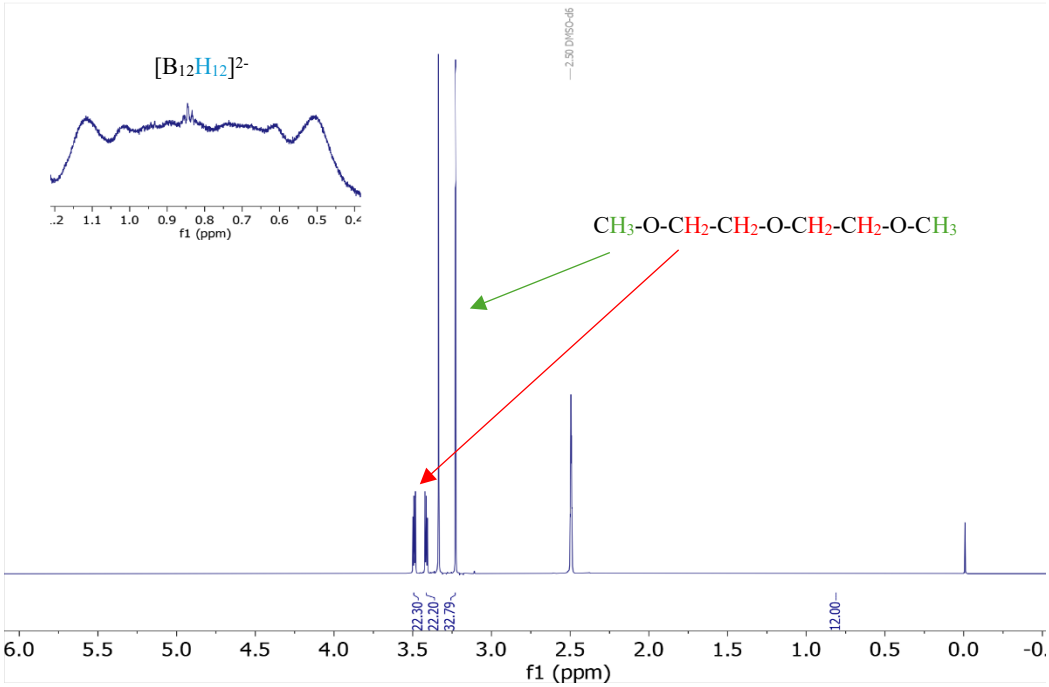

Figure 16. ^{1}H-NMR spectrum of $Na_2B_{12}H_{12}$·4diglyme (sample G).

To accurately determine the quantity of diglyme within the synthesized $Na_2B_{12}H_{12}$, a TG-DTA was conducted (*Figure 17*). The total mass loss at 193° C was approximately 74 %. Given that the final product is known to be unsolvated $Na_2B_{12}H_{12}$,[89] the amount of diglyme in the sample (x) could be calculated using the following formula (7):

$$x = \frac{\left(\frac{100 \,.\, M_{Na_2B_{12}H_{12}}}{Residual\ weight\ (\%)} - M_{Na_2B_{12}H_{12}}\right)}{M_{diglyme}} \qquad (7)$$

The initial endothermic mass loss, approximately 35 %, was attributed to the synchronized release of two diglyme molecules at 60 °C, while the subsequent two endothermic mass losses (15 % and 20 %) at 130 °C and 150 °C respectively were presumably associated with the release of approximately one molecule of diglyme each. The calculations utilizing *equation 7* resulted in an estimate of 3.98 diglyme molecules per $Na_2B_{12}H_{12}$, which agrees with the aforementioned claim.

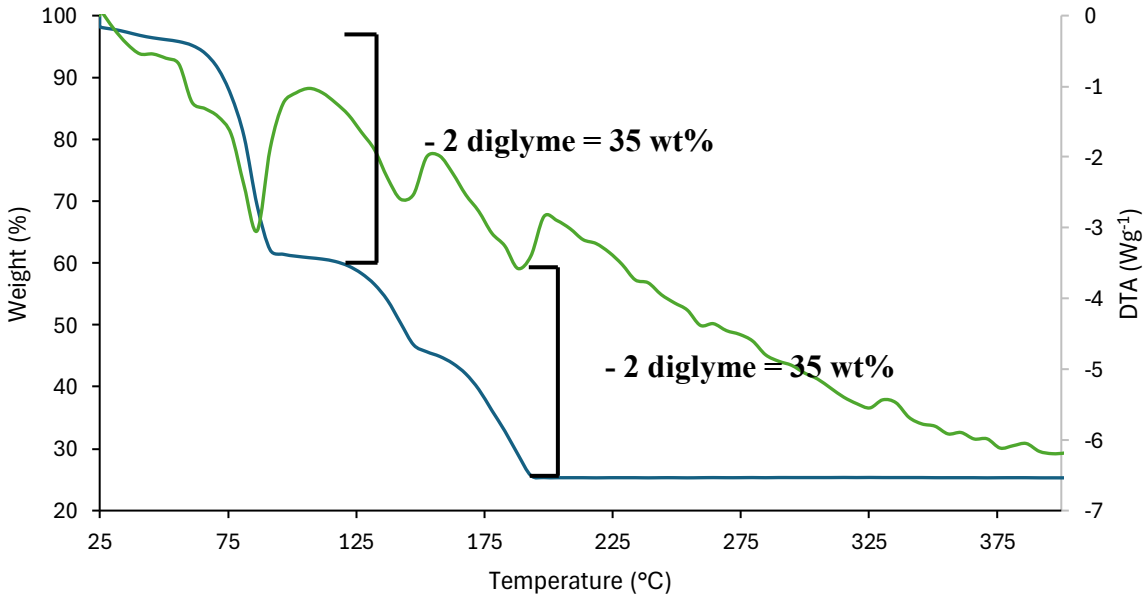

Figure 17. TG-DTA of the as-synthesized $Na_2B_{12}H_{12}$·4diglyme (sample G). Color code: blue = TGA, green = DTA.

3.1.2. $Cs_2B_{12}H_{12}$

The potential for CO_2 sorption in porous ionic packing composed of uniformly spherical cations was investigated using commercial $Cs_2B_{12}H_{12}$ as model compound. Prior to gas sorption, the sample purity was assessed by ^{11}B- and ^{1}H-NMR spectroscopy, ATR-IR and PXRD. The sample shows no impurities detectable by these analyses, the XRD shows that it is the right phase (***A3-A5***).

A TG-DTA (*Figure* 18) was conducted to evaluate whether the compound contained any adsorbed substances and to detect any phase transitions induced by temperature changes. The results showed virtually no mass loss, meaning the compound did not adsorb any guest, even when exposed to air during the sample preparation for analysis. The DTA however revealed a minor endothermic peak at approximately 55°C, without any associated mass loss, which could indicate a possible phase transition. As no such phase transitions are reported in existing literature, to the best of our knowledge, PXRD measurements were conducted at 300 K and 400 K, experimentally confirming the absence of any discernible phase transitions, as shown in *Figure 19*.

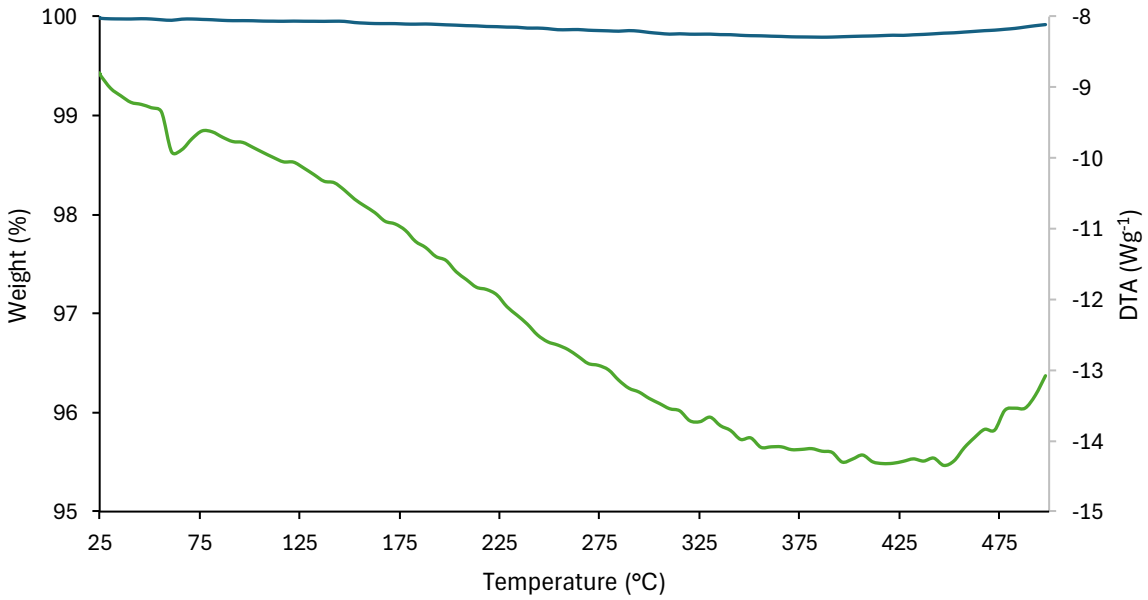

Figure 18. TG-DTA measurement of the commercial $Cs_2B_{12}H_{12}$. Color code : blue = TGA, green = DTA.

After confirming the purity and the phase of the sample, we investigated the sorption of CO_2 by conducting an *in situ* PXRD measurement, following the procedure described in section *2.3*, under a pressure of 10.3 bar of CO_2 gas between 300 and 400 K (*Figure 20*). The

experiment shows no appreciable modification of the PXRD pattern, due either to the absence of gas sorption, or to the poor electron density of CO_2 compared to that of $Cs_2B_{12}H_{12}$, not enabling to witness any changes in relative intensities upon CO_2 incorporation.

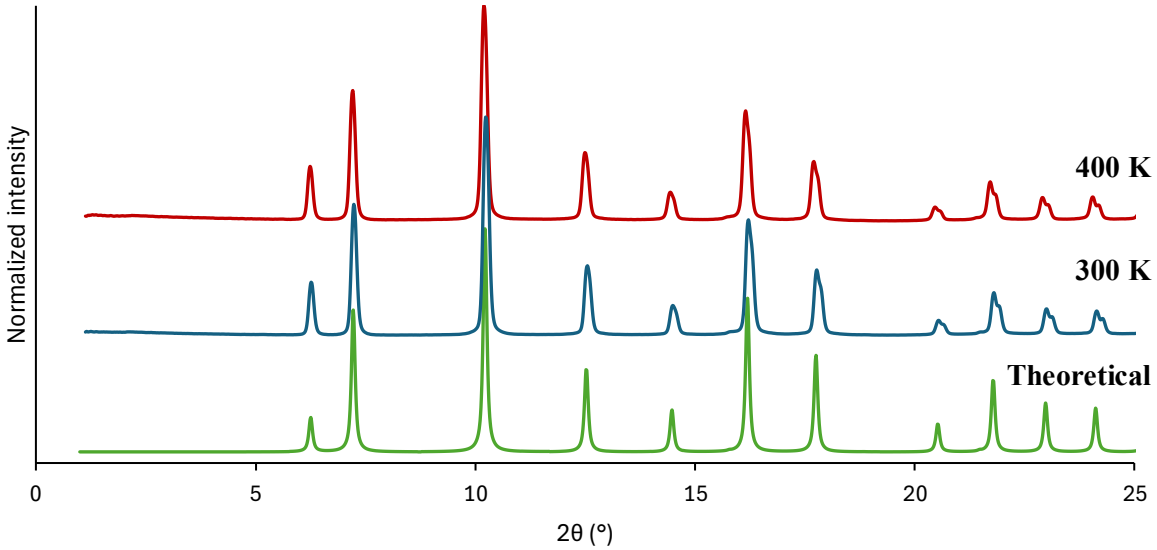

Figure 19. Theoretical and experimental powder patterns of $Cs_2B_{12}H_{12}$ measured at 300 K and at 400 K.

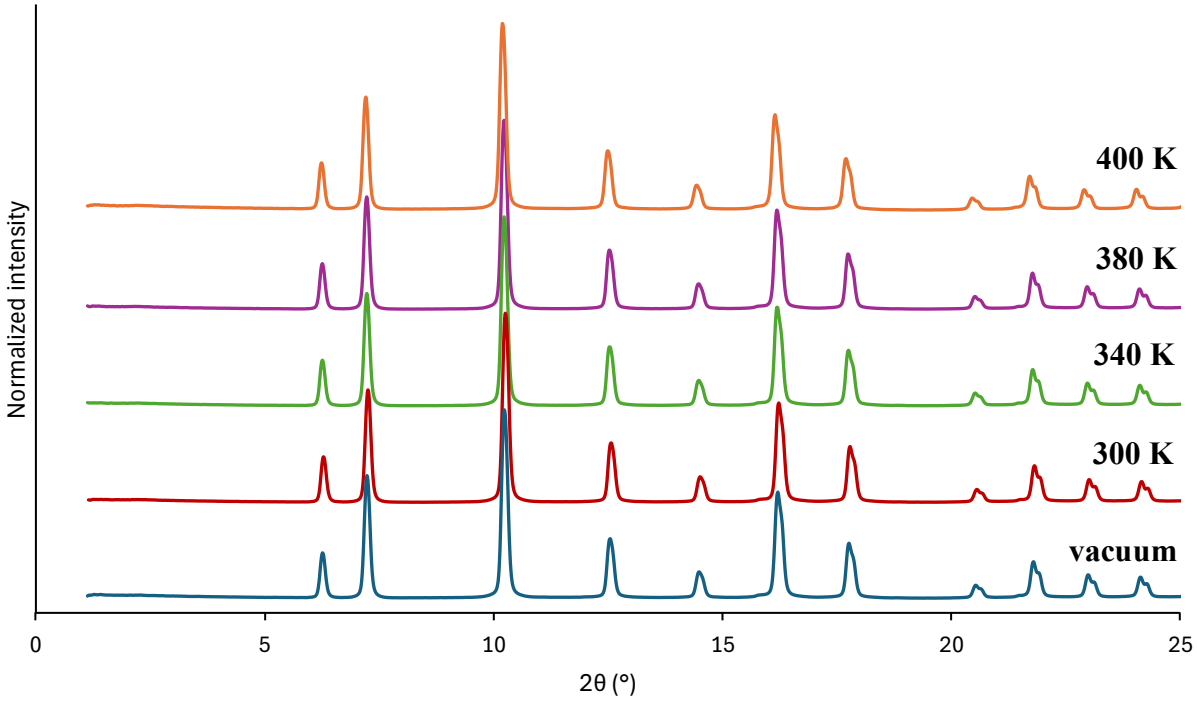

Figure 20. Powder patterns of $Cs_2B_{12}H_{12}$ under vacuum (300 K) and under a pressure of 10.3 bar of CO_2, at 300, 340, 380 and 400 K.

To test these two hypotheses, volumetric measurements were carried out at RT up to an equilibrium pressure of 12.5 bar CO_2. As depicted in the Appendix (***A6-A7***), there was little to no uptake of CO_2 (uptake is in the error-range of the machine), despite the pores being large enough to accommodate guest CO_2 (the kinetic diameter of CO_2 is 3.30 Å).[100] The measurements therefore confirm that, in these conditions, a spherical cation such as Cs^+ does not induce CO_2 sorption in *closo*-dodecaborates, despite the presence of voids within the crystal structure. This led us to further investigate other cations with different symmetries, such as tetrahedral, in order to evaluate the impact of cation symmetry variation on the gas sorption properties of dodecaborates, in the same conditions.

3.2. Dodecaborates with T_d organic cations

3.2.1. $(NMe_4)_2B_{12}H_{12}$

As previously mentioned (in section *2.2.2*), the synthesis of TMAD involves the ion exchange between NMe_4Br and $Na_2B_{12}H_{12}\cdot$4diglyme, $Na_2B_{12}H_{12}\cdot 4H_2O$ or unsolvated $Na_2B_{12}H_{12}$ in cold water (8):

$$Na_2B_{12}H_{12} + 2\ NMe_4Br \rightarrow [NMe_4]_2B_{12}H_{12} + 2\ NaBr \qquad (8)$$

The purity of TMAD was assessed with ^{1}H- and ^{11}B-NMR spectroscopy (*Figure 21*) and ATR-IR (*Figure 22*). The ^{11}B-NMR shows the characteristic $[B_{12}H_{12}]^{2-}$ peak at -16.5 ppm, while the ^{1}H-NMR spectrum demonstrates the signal of $[NMe_4]^+$ at 3.1 ppm (*s*) and residual water in the pores at 3.3 ppm (*s*) or in the DMSO. The integration of the $[B_{12}H_{12}]^{2-}$ indicates 2.65 $[NMe_4]^+$ per dodecaborate, further demonstrating the quantification problems raised previously in *section 3.1.1*. The peaks in the IR spectrum of TMAD indicated the presence of water at 3600 cm^{-1}, which appeared at an unusually high wavenumber. We hypothesize it is due to an interaction between the proton of the water and the hydridic hydrogen of the borate, leading to the shift.[101] Additionally, we observe the C-H stretching of the methyl groups at 3000 cm^{-1}, B-H stretching at 2480 cm^{-1} and the B-B breathing modes of the dodecaborate around 1050 cm^{-1}.

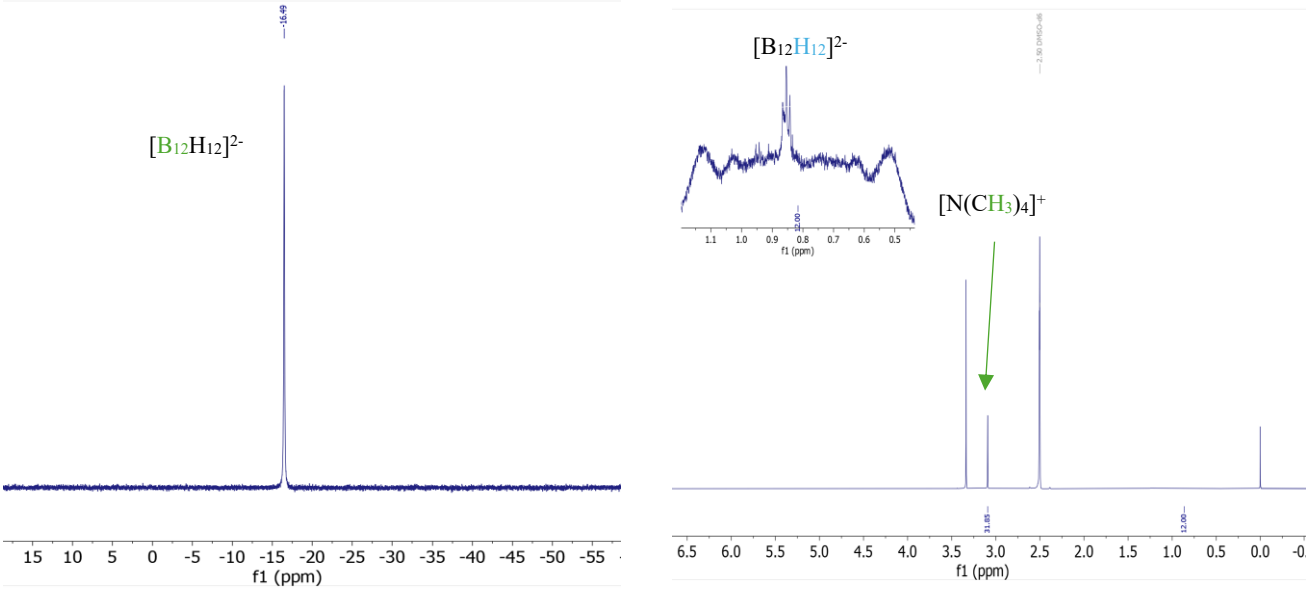

Figure 21. ^{11}B- (left) and ^{1}H- (right) NMR spectra of TMAD.

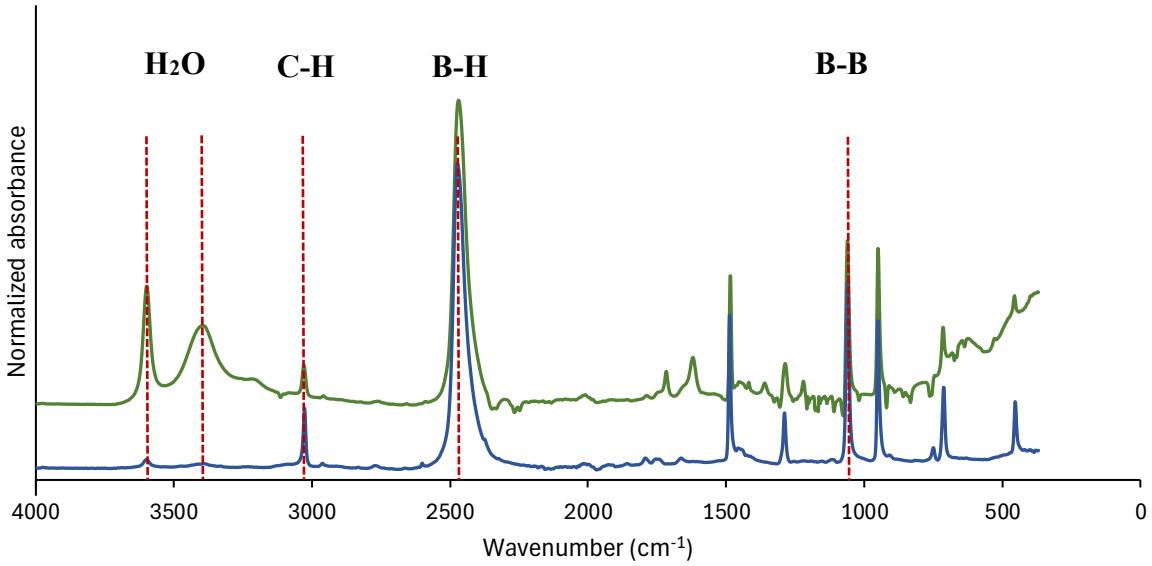

Figure 22. Infrared spectra of TMAD synthesized in cold water before (blue) and after air exposure for three weeks (green).

The X-ray diffraction powder pattern of TMAD synthesized in cold water is illustrated in *Figure 23*, exhibiting phase purity, with however some minor alterations in the 2θ values, indicative of lattice expansion. This phenomenon can be attributed to the sorption of guest molecules, supposedly water from the synthesis process, into the lattice voids.

Subsequently, the powder was subjected to vacuum at 400 K for three hours, before being re-analyzed by PXRD, revealing changes in the relative intensities of the peaks. This observation further supports the presence of guest molecules within the pores, that can be removed through vacuum and heat treatment.

Surprisingly, conducting the exchange reaction in hot water (close to the boiling point) instead of cold water, and letting the solution cool down to RT resulted in the appearance of additional peaks (5.5 and 9 °) and in a substantial change in relative intensities in the powder patterns (*Figure 23*). This alteration of relative peak intensities strongly suggests that there is a significantly higher amount of water present in the pores when synthesized in hot water compared to cold water. The appearance of new peaks strongly suggests the existence of another polymorph, for which the structure remains unsolved at the moment. For clarity, we will designate the porous phase of interest as *fcc*. Interestingly, when subjected to vacuum at 400 K for three hours, the peak related to the secondary phase disappear, while observing the loss of the guests from the porous phase, leading to the restauration of unsolvated TMAD.

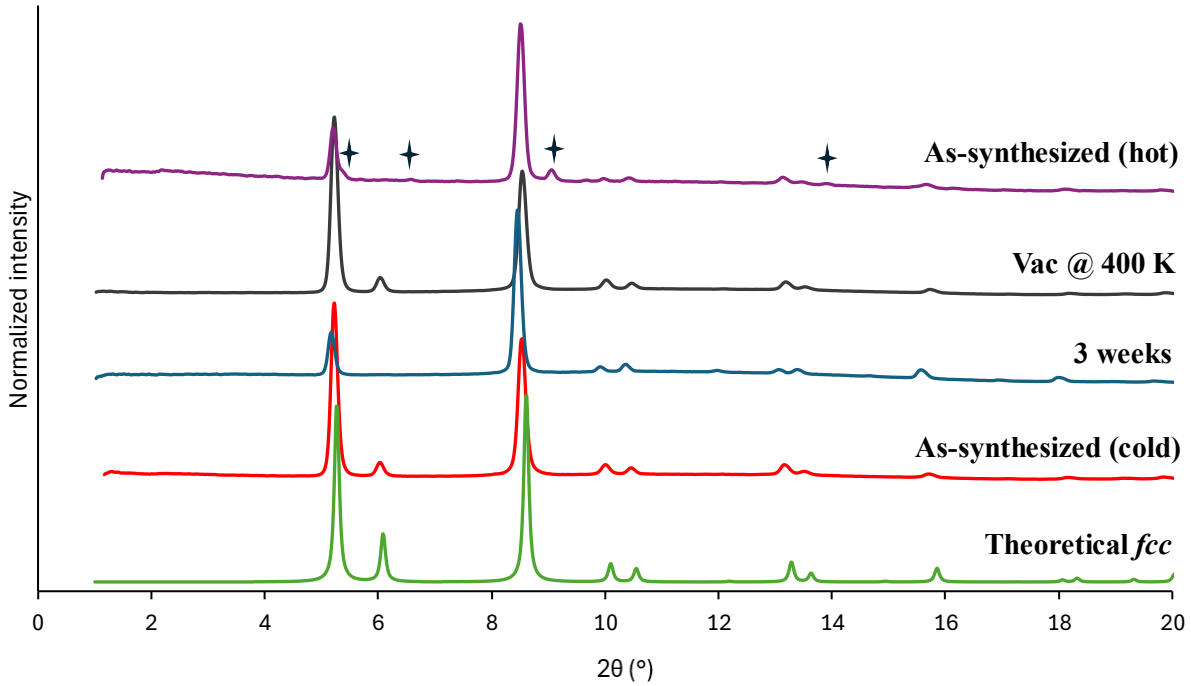

Figure 23. Theoretical *fcc* and experimental powder patterns of TMAD as-synthesized in cold water, left under air for 3 weeks, put under vacuum at 400 K for 3 hours and as-synthesized in hot water. The peak marked by a black star belong to an unknown phase of TMAD.

When unsolvated TMAD is exposed to air for approximately three weeks, its powder pattern changes to closely resemble that of TMAD synthesized in hot water. The relative intensities and 2θ shifts are nearly identical, though slightly higher, and it lacks the additional phase observed in the hot water synthesis. This indicates that TMAD is capable of effectively sorbing moisture, though slowly, from the surrounding air. The lattice parameter *a* is reported in *Table 3* ^for various samples. Since the *fcc* TMAD is cubic, the lattice constant can be determined from the first Bragg reflection corresponding to the (100) plane. By applying Bragg's law, we can convert the 2θ angle into an interplanar distance (d), where the (100) reflection directly provides the lattice parameter *a*. We observe a gradual expansion of the unit cell corresponding to the increasing amount of water sorbed by the TMAD.

Table 3. Lattice parameter for the fcc TMAD for samples shown in *Figure 11*.

Sample	**Lattice parameter *a* (Å)**
Theoretical *fcc*	13.39
As-synthesized (cold)	13.27
After 3 weeks on air	13.09
After vacuum @ 400 K	13.32
As-synthesized (hot)	13.17

TG-DTA was carried out on the TMAD sample exposed to air for three weeks. This helped us to find the temperature at which guest molecules are released, assessing the quantity of the guest present, and to determine the temperature range within which TMAD remains stable prior to the decomposition. The results are shown in *Figure 24*. The initial mass loss of 19 % begins directly from the onset temperature of 25°C and continues until 65°C. This mass loss coincides with the endothermic peak, suggesting the release of guests, presumed to be 4 molecules of water. The compound maintains stability up to approximately 310°C, beyond which a further mass loss of 10 % occurs, accompanied by an exothermic peak, indicating the decomposition of our compound.

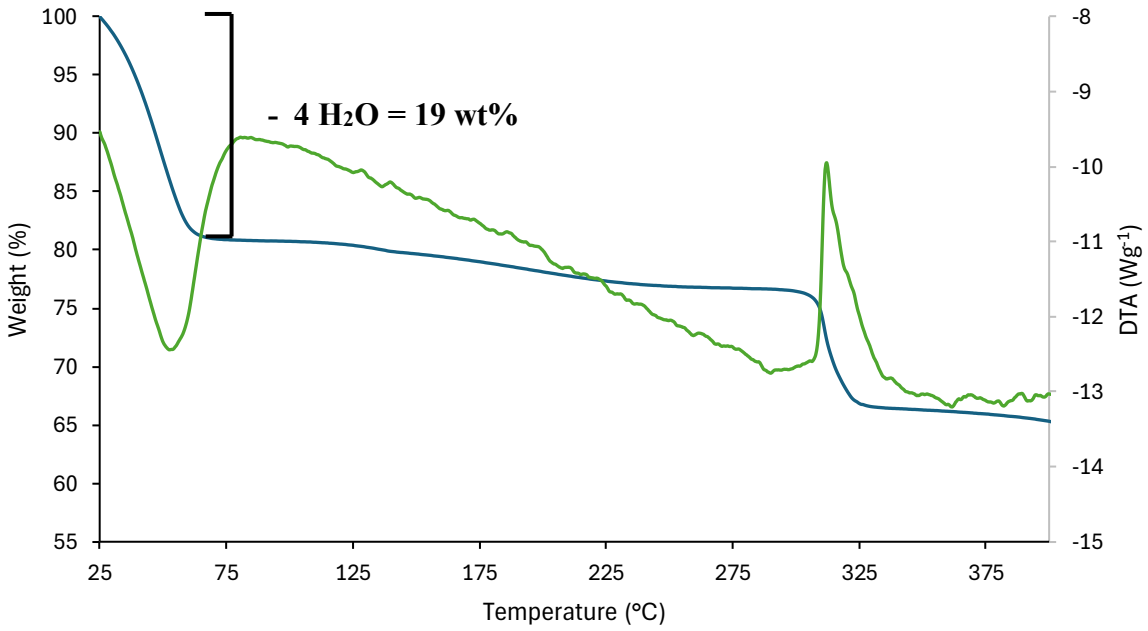

Figure 24. TG-DTA measurement of the TMAD sample exposed to air for three weeks. Color code: blue = TGA and green = DTA.

To assess the maximum amount of water the TMAD can sorb, we conducted a DVS experiment. The results are illustrated in *Figure 25*, revealing an approximately 15 % increase in mass over the measurement period. This indicates the compound's capability to effectively adsorb water, under certain relative humidity. Additionally, a notable consideration in this measurement is the incomplete desorption of water. Upon restoring the relative humidity (RH) to 10 %, the mass remains approximately 2 % higher than in the initial measurement, thereby illustrating the slow process of desorption.

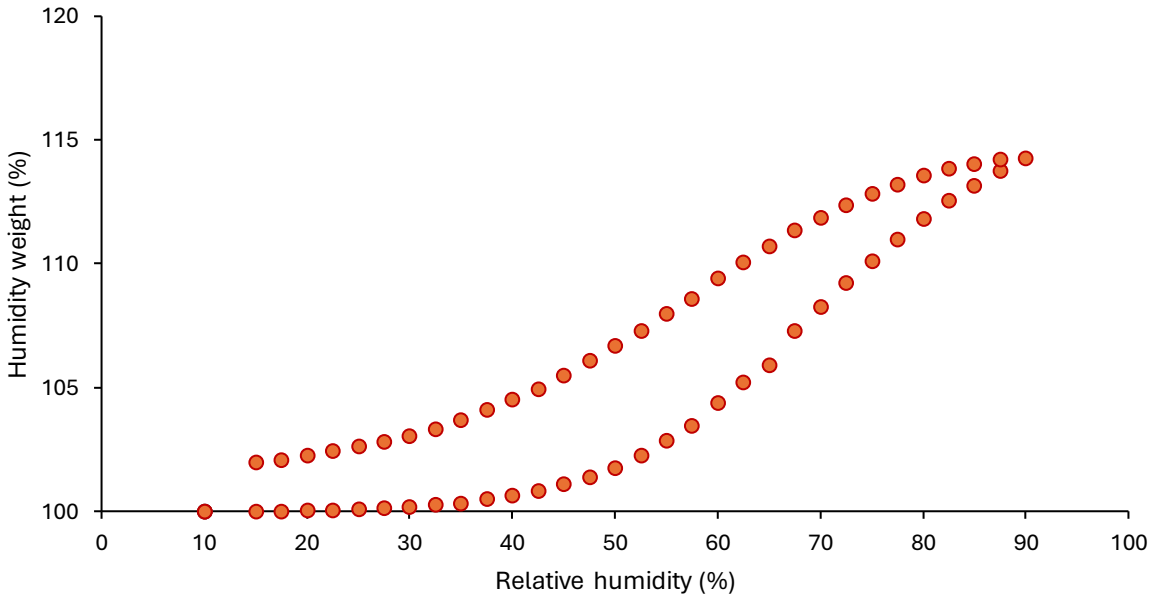

Figure 25. DVS measurement of the unsolvated TMAD.

The main objective of this master's thesis was to demonstrate that the large organic cation counterbalancing the dodecaborates allowed for a gas sorption in the resulting compounds. To validate this hypothesis, *in situ* PXRD measurements were conducted. In *Figure 26*, the evolution of TMAD powder patterns under isotherm and isobar conditions of 10.3 bar CO_2 and 300 K is depicted. A remarkable difference in peak relative intensity is observed while maintaining consistent 2θ values. This suggests that the porous cubic phase of TMAD remains unchanged, while modifications in the electronic density within the crystal lattice occurred, revealing substantial CO_2 adsorption. Specifically, attention must be drawn to the two most prominent peaks, at 5.2° and 8.5°. The significant variation in relative intensity between these two peaks after five minutes of exposure to the gas and to the vacuum allows to confirm this claim. The pattern of the two first peaks shrinking and the third one amplifying persists until the final measurement conducted after two hours of exposure, indicating a rather slow but continuous CO_2 uptake. It's worth noting that this alteration in peak intensity mirrors that observed in fully hydrated TMAD. The powder pattern on top of the *Figure 26* illustrates that similar behavior is observed, though at an accelerated rate when the *in situ* diffraction measurement is conducted at higher temperatures. This suggests that the kinetics of gas sorption may be enhanced by elevating the temperature (as it is often the case). Our hypothesis is that sorption is governed by the coupling of the rotational motion of ions and the diffusion of the guest inside the lattice. Therefore, we attempted to increase gas sorption capacity/kinetics by

enhancing the rotational motion by ultrasound but did not get successful results. Future efforts will focus on identifying external stimuli capable of enhancing sorption kinetics. Our endeavors to determine the precise position and occupancy of CO_2 were unsuccessful, attributed to the complexity in the disorder of CO_2 within the pores. However, from these trials, we could deduce that under conditions of full CO_2 saturation, each pore likely contains two CO_2 molecules positioned along the pore surface.

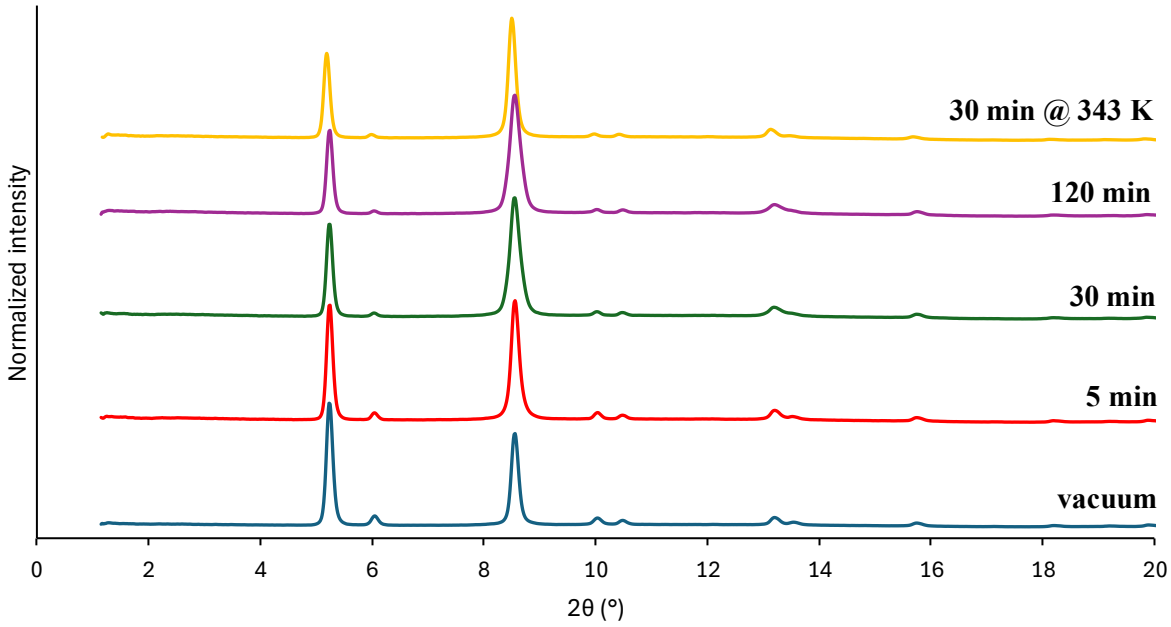

Figure 26. Evolution of the PXRD pattern of TMAD under the pressure of 10.3 bar of CO_2 at 300 K. In orange is shown the PXRD pattern of TMAD after 30 minutes at 343 K at 10.3 bar of CO_2.

To better characterize the amount of CO_2 adsorbed by TMAD, volumetric measurements were conducted (*Figure 27*). We initially started the measurement with CO_2, gradually going up to 12.5 bar, and recording the uptake at each equilibrium pressure point, followed by a desorption measurement. First, we observed CO_2 uptake, indicating that the replacement of Cs^+ with $[NMe_4]^+$ indeed facilitated the sorption. Second, we did not reach the saturation at the last sorption point, suggesting that the maximum CO_2 sorption capacity is far from being attained. Third, during the desorption process, the compound continued to adsorb CO_2, reinforcing the conclusion that the sorption kinetics is slow. This is also illustrated in ***Figure A8***, which shows that the equilibrium pressure is never reached at any point. This implies that a much longer measurement would be necessary to reach the CO_2 saturation plateau, or higher temperatures should be used to improve the kinetics. We can then calculate the percentage weight of CO_2

sorbed by multiplying the highest uptake by 10^{-4} (to account for the change in units) and the molar mass of CO_2, resulting in 5.92 wt%. For comparison, MIL-101 (Cr, Mg) sorbs 14.4 wt% of CO_2.[102] Let's however keep in mind that we haven't yet reached the maximum amount of CO_2 that can be sorbed, making direct comparisons challenging.

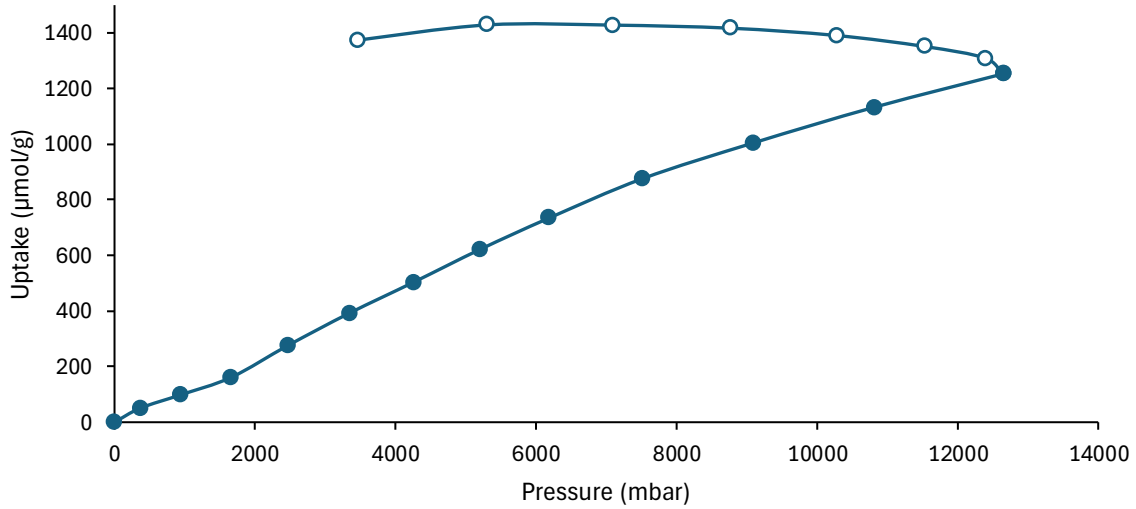

Figure 27. CO_2 sorption isotherm of TMAD measured at RT. Sorption is depicted by the full circles, the empty circles picturing the desorption.

Following the measurements, we recovered the sample and conducted PXRD analysis to assess potential reactions with CO_2. *Figure 28* illustrates that the TMAD remains unchanged, although there are noticeable shifts in relative intensities, indicating incomplete desorption.

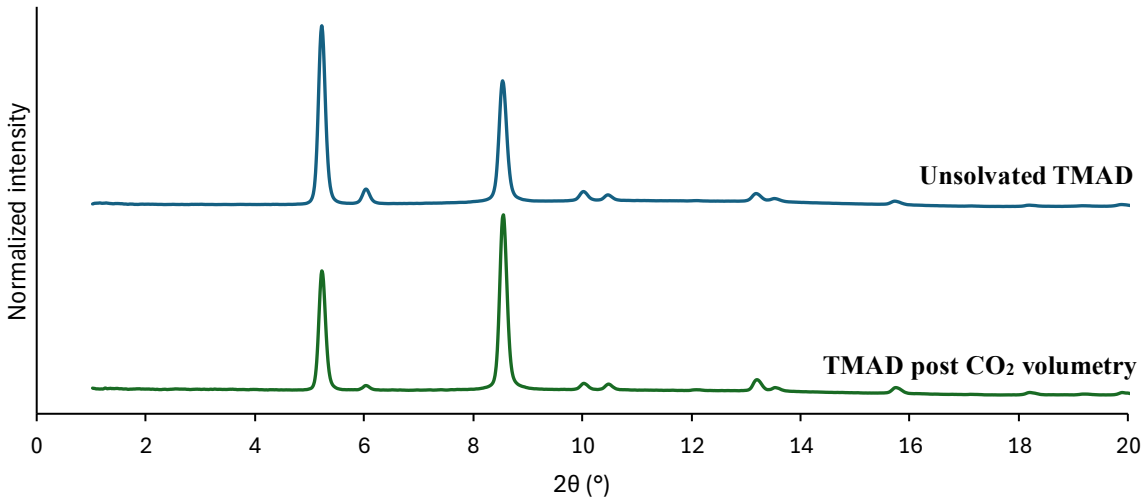

Figure 28. Comparison of the powder patterns of the TMAD after the volumetric measurement under CO_2 and the unsolvated TMAD.

We also conducted volumetric measurement with hydrogen at 20°C, to probe the TMAD H_2 storage capacity (***Figure 29***). We initially started the measurement going gradually up to an equilibrium pressure of 93 bar. We recorded the uptake at each stable equilibrium pressure point, followed by a desorption measurement. The results indicate effective H_2 sorption with a maximum uptake of 1064 µmol/g at 93 bar. However, we did not reach the maximum H_2 sorption, although kinetics are way better this time around (***A9***), equilibrium pressure being reached, as demonstrated by the plateaus obtained. An interesting aspect of the data is the faster desorption rate compared to CO_2 sorption, and the observation that the uptake was negative during desorption. This could suggest: i) the compound began decomposing under H_2 pressure, ii) the pores were not empty at the start of the measurement, or iii) there was an issue with the equipment. To investigate, we performed a subsequent PXRD analysis of the compound (***A10***). The results showed no decomposition of the TMAD, although there were differences in relative intensities compared to the guest-free TMAD. This indicates that despite the negative uptake in the volumetric measurement, H_2 remained in the pores, implying that desorption was not complete. Therefore, the amount of H_2 sorbed is most likely underestimated. The methodology employed for CO_2 sorption can be similarly applied to assess the amount of H_2 into the pores, leading to 0.21 wt% (for comparison, HKUST-1 can store up to 0.47 wt.% of H_2 at 303 K and 35 bar).[45]

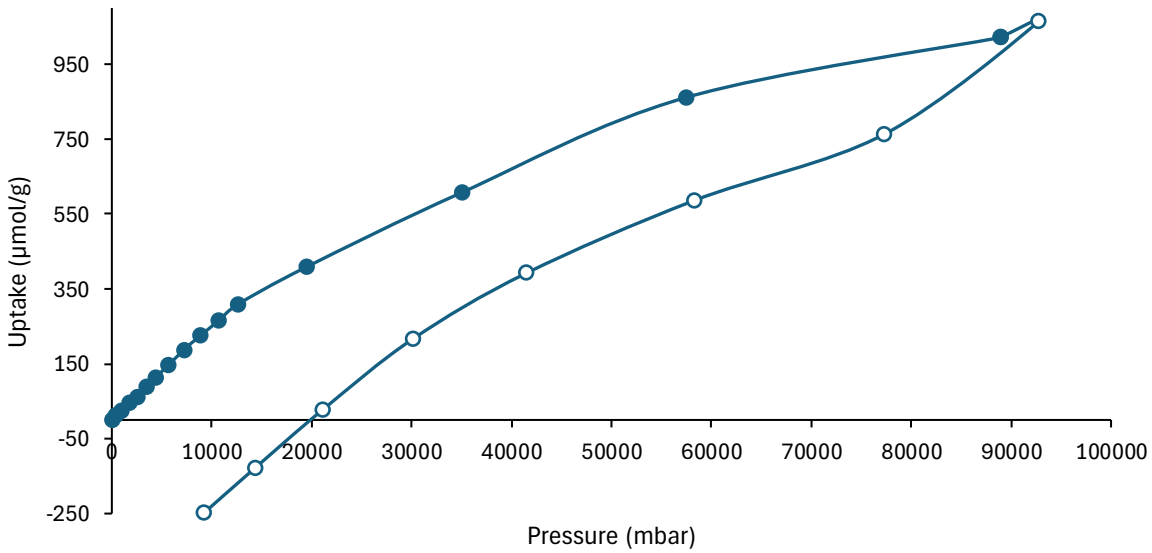

Figure 29. H_2 sorption isotherm of TMAD measured at 20°C. Sorption is depicted by the full circles, the empty circles picturing the desorption.

To complement the data obtained in volumetry, we had the privilege to conduct neutron diffraction experiments in Grenoble, at the ILL. This sample was one of the three selected for this remarkable technique. Therefore, prior to the sample preparation, we conducted X-ray fluorescence to ensure that there was no bromide contamination from the synthesis. Indeed, bromine has a relatively high neutron absorption cross-section, meaning that it tends to absorb neutrons rather than scatter them. This can lead to attenuation of the neutron beam and distortion of the diffraction pattern, making it more difficult to accurately interpret the results. *Table 4* shows the results obtained, displaying only the three elements with the highest concentrations. The sample exhibited slight bromine contamination, certainly stemming from the synthesis conditions, likely in the form of NaBr. This contamination is insufficient to justify any concern. It is noteworthy that the sodium and magnesium concentrations may be subject to some inaccuracies, owing to their limited X-ray absorption capabilities. Since the natural mixture of boron isotopes also adsorbs neutrons, we used a thin-walled cylinder to contain the sample, reducing the adsorption of neutrons substantially.

Table 4. XRF elemental analysis of TMAD.

Element	Concentration (%)
^{35}Br	2.14 %
^{11}Na	1.65%
^{12}Mg	0.27%

We conducted NPD experiment at 77 K, loading D_2 up to the maximum pressure of 60 bar. Unfortunately, the relative peak intensities did not change significantly, indicating that hydrogen adsorption in the pores was too slow at the given pressure-temperature conditions. This suggests that the gas adsorption kinetics by *fcc* TMAD is exceptionally slow, and we need to do a detailed preparation of the gas loading protocol for the NPD measurements which are very limited in time.

3.2.2. $(PMe_4)_2B_{12}H_{12}$

Next, we decided to substitute $[NMe_4]^+$ by its phosphorated homologue, $[PMe_4]^+$, resulting in the synthesis of TMPD. The same process used for TMAD is employed here, which involved the cation exchange in cold water between the $Na_2B_{12}H_{12}$·4diglyme, $Na_2B_{12}H_{12}$·$4H_2O$ or unsolvated $Na_2B_{12}H_{12}$ and PMe_4Br (9):

$$Na_2B_{12}H_{12} + 2\ PMe_4Br \rightarrow [PMe_4]_2B_{12}H_{12} + 2\ NaBr \quad (9)$$

Obtaining a single crystal of the compound enabled the identification and structure determination of the two distinct phases. One phase closely resembles the porous structure of TMAD, with the nitrogen atom being replaced by phosphorus in the same anti-CaF_2 *fcc* type of lattice (***A11***). The other phase, however, shows no similarity with the *fcc* type. The lattice parameters of the porous cubic TMAD and TMPD are highly similar (a = 13.3887 and 13.3695 Å, respectively). The volume of the solvent-accessible surface in TMPD is 67.79 $Å^3$, accounting for 2.8 % of the total lattice volume (smaller than in TMAD). The second phase TMPD phase exhibits monoclinic symmetry and is characterized by twinning, complicating the process of structure determination. The structure is shown in *Figure 30*, with a significant disorder remaining, possibly stemming from not fully modelled twinning. Furthermore, this phase does not display porosity.

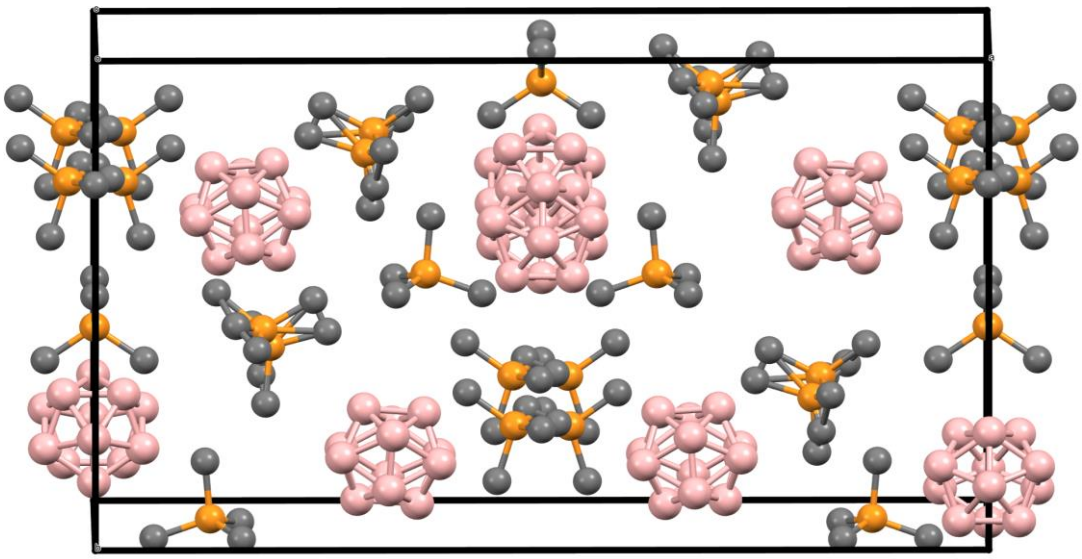

Figure 30. Monoclinic phase of TMPD shown without hydrogens for clarity. Color code: B = pinkish, C = grey and P = orange.

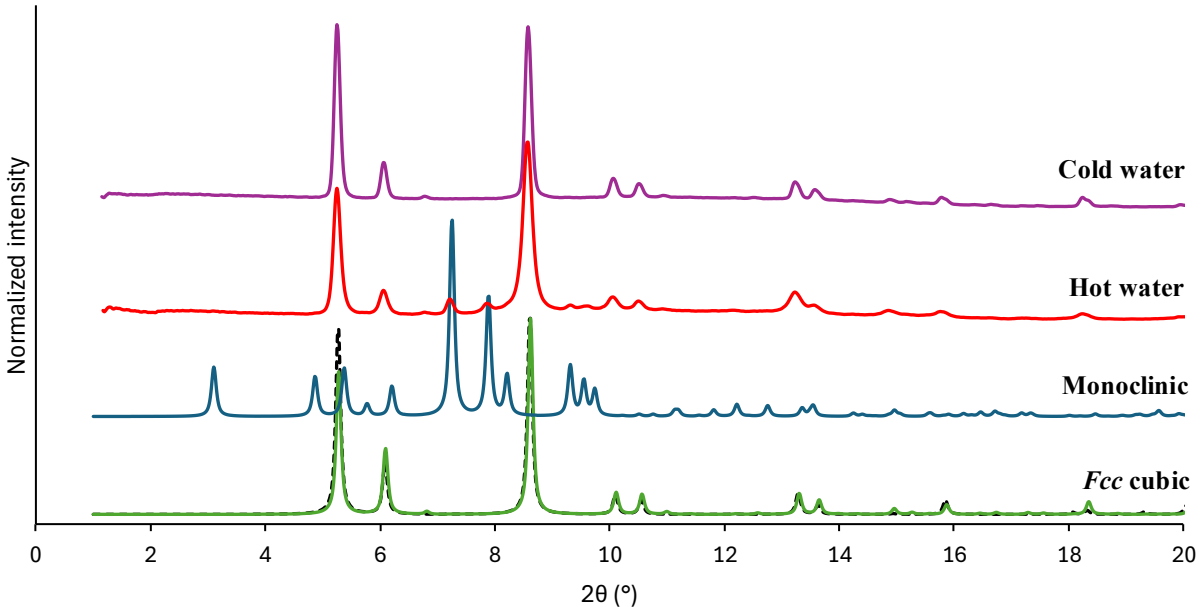

Figure 31. Powder patterns of the theoretical cubic, theoretical monoclinic, as-synthesized in hot water cold water TMPD. The black dashed line represents theoretical cubic TMAD.

The powder patterns of the as-synthesized TMPD in both cold and hot water are depicted alongside theoretical (simulated) cubic and monoclinic TMPD in *Figure 31*. From this data, it was apparent that TMPD, much like TMAD, manifested different behaviors depending on whether the ionic exchange occurred in hot or cold water. The TMPD that arose from cold water was single phased pure (*fcc*), while the TMPD that came from hot water contained the two aforementioned phases. The comparison of peak intensities between the two phases in hot water clearly indicated that the cubic phase is more stable. Moreover, we found a difference in peak intensities between the TMPD synthesized under hot and cold conditions, much like we observed for TMAD. This suggests that the TMPD synthesized in hot conditions has adsorbed more water compared to its counterpart synthesized under cold conditions. It is also worth mentioning the near perfect similarity observed in the powder patterns of both *fcc* TMAD and TMPD.

The purity was further assessed with ^{1}H- and ^{11}B-NMR spectroscopy (*Figure 32*) and ATR-IR (*S18-S19*). The ^{11}B-NMR shows the characteristic $[B_{12}H_{12}]^{2-}$ peak at -16.5 ppm (*s*) and a bump between 25 and -10 ppm caused by the glass NMR tube (not made of quartz). The ^{1}H NMR spectrum demonstrates the presence of $[PMe_4]^{+}$ at 1.8 ppm (*d*) and water at 3.3 ppm (*s*). An expansion on the 0.4-1.1 ppm region is shown on the top left of the ^{1}H NMR, revealing the distinctive pattern of hydrogen coupling in the $[B_{12}H_{12}]^{2-}$ molecule. The infrared spectrum of

TMPD is compared to the spectrum of TMAD in *Figure 33*. The characteristic peaks in the spectra of both compounds align at nearly identical wavenumbers, again showcasing the similarity between the two compounds. The water peak at 3600 cm^{-1} is absent from the TMPD spectrum, indicating the emptiness of the pores.

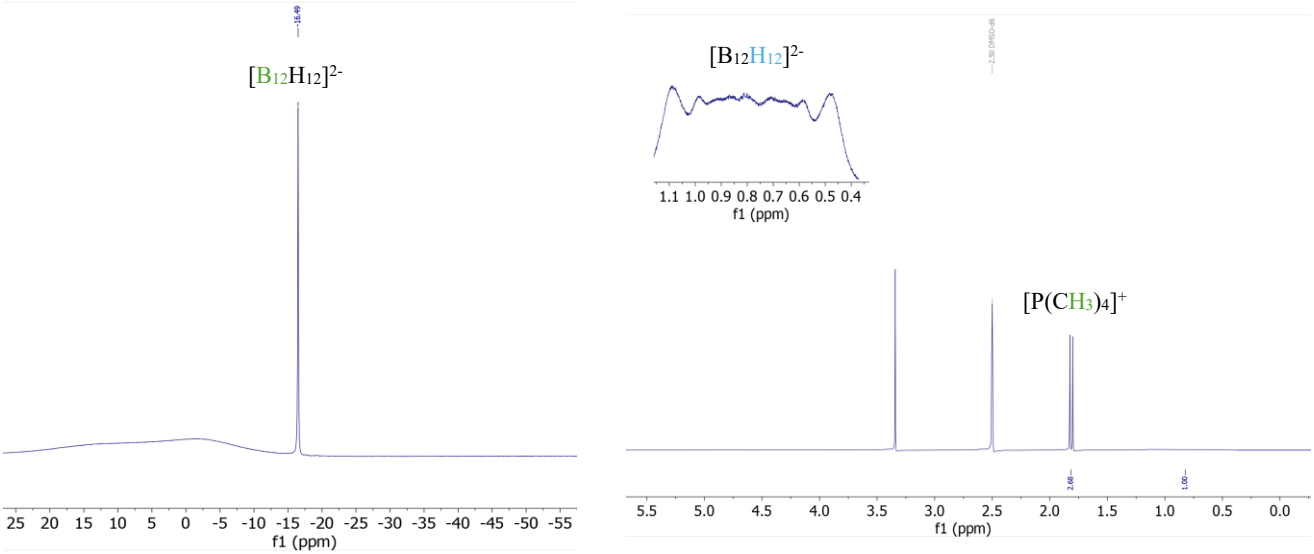

Figure 32. ^{11}B- (left) and ^{1}H- (right) NMR spectra of TMPD. In the upper left corner, there is an enlargement focusing on the characteristic region of the $[B_{12}H_{12}]^{2-}$, between 0.4 and 1.2 ppm.

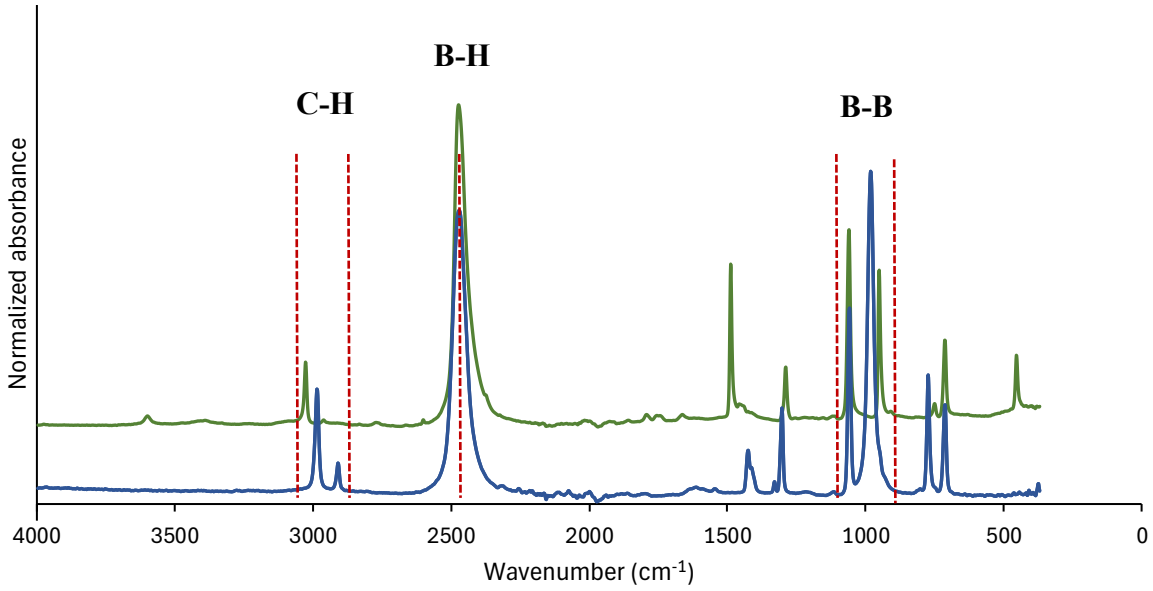

Figure 33. Infrared spectra of TMPD (blue) and TMAD (green).

A TG-DTA was carried out on TMPD and displayed in *Figure 34*. The first mass loss is negligible, about 1 %, meaning the sample may have adsorbed water during the sample preparation. The mass remained constant up to about 400°C, showcasing the stability of TMPD, surpassing that of TMAD by 100°C. The exothermic peak at 420°C accompanied by a variation in mass of about 5 % is attributable to the decomposition of the TMPD.

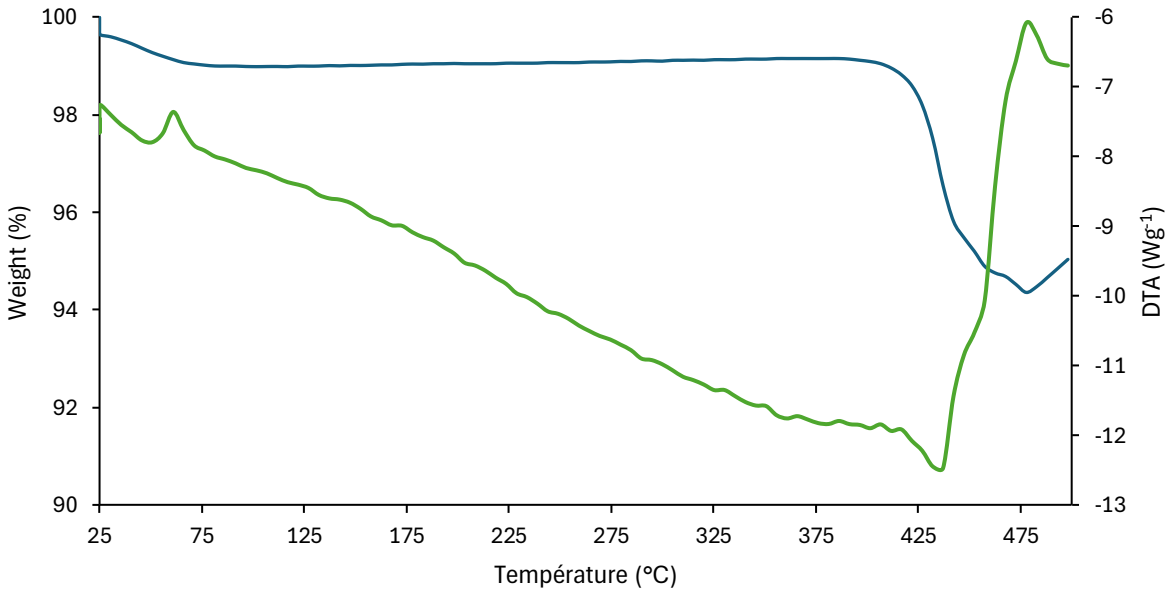

Figure 34. TG-DTA measurement of the TMPD. Color code: blue = TGA and green = DTA.

In the following measurements, we led an investigation to better understand the behavior of TMPD concerning phase transitions and compare the results to TMAD. A comparative analysis was facilitated by the prior elucidation of the structures of both initial TMPD phases. Initially, the compound was put under vacuum at 300 K for ten minutes, followed by exposure to 10 bar of CO_2 for one hour, maintaining the temperature at 300 K throughout the experiment. XRD measurements were performed at intervals of five minutes of exposure to the X-ray beam. The resulting data, presented in *Figure 35*, indicated a distinct transition from the monoclinic phase to the porous cubic TMPD upon CO_2 exposure. Additionally, it is noted that at 300 K, there is only a modest change in peaks relative intensity following an hour of CO_2 exposure, further indicating the slow sorption kinetics under these specific conditions.

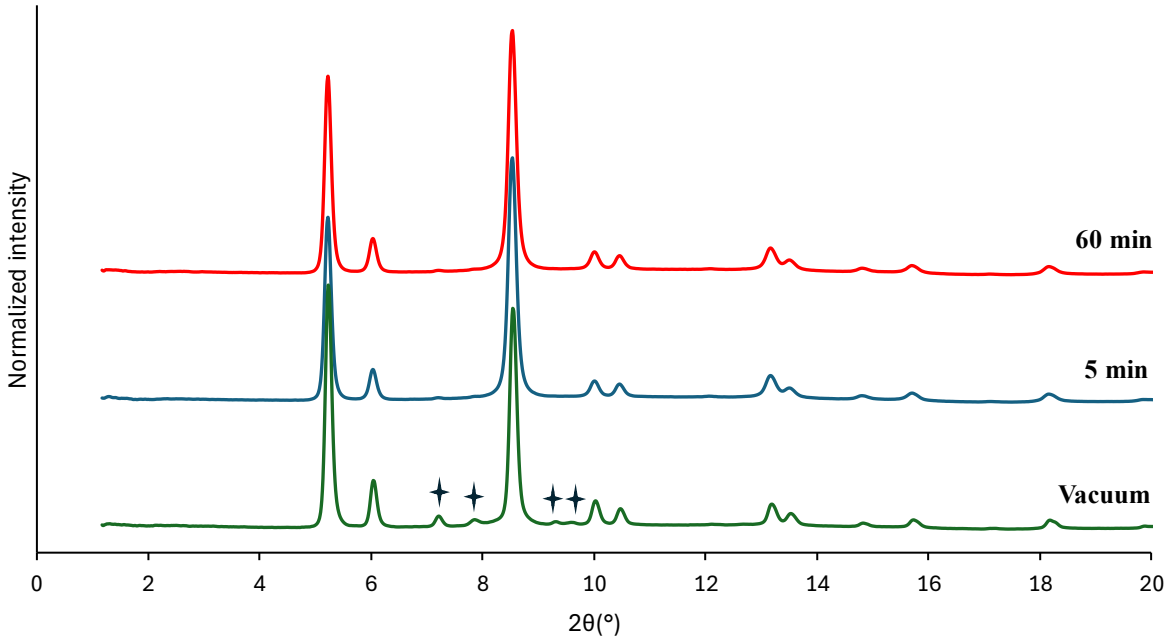

Figure 35. Powder patterns of the TMPD under vacuum and under 10 bar of CO_2 at 300 K for five minutes and an hour. The black stars indicate the peaks related to the non-porous TMPD phase.

In situ PXRD experiments were performed to validate the gas sorption capability of TMPD, with initial focus on CO_2. The measurements were conducted under a CO_2 pressure of 7.2 bar, utilizing the temperature protocol described in the *section 2.3*. The compound was initially subjected to ten minutes of vacuum exposure at 300 K to ensure thermal stabilization. The resulting data, depicted in *Figure 36*, revealed variations in peak intensities, indicative of effective CO_2 sorption, though with minimal changes observed.

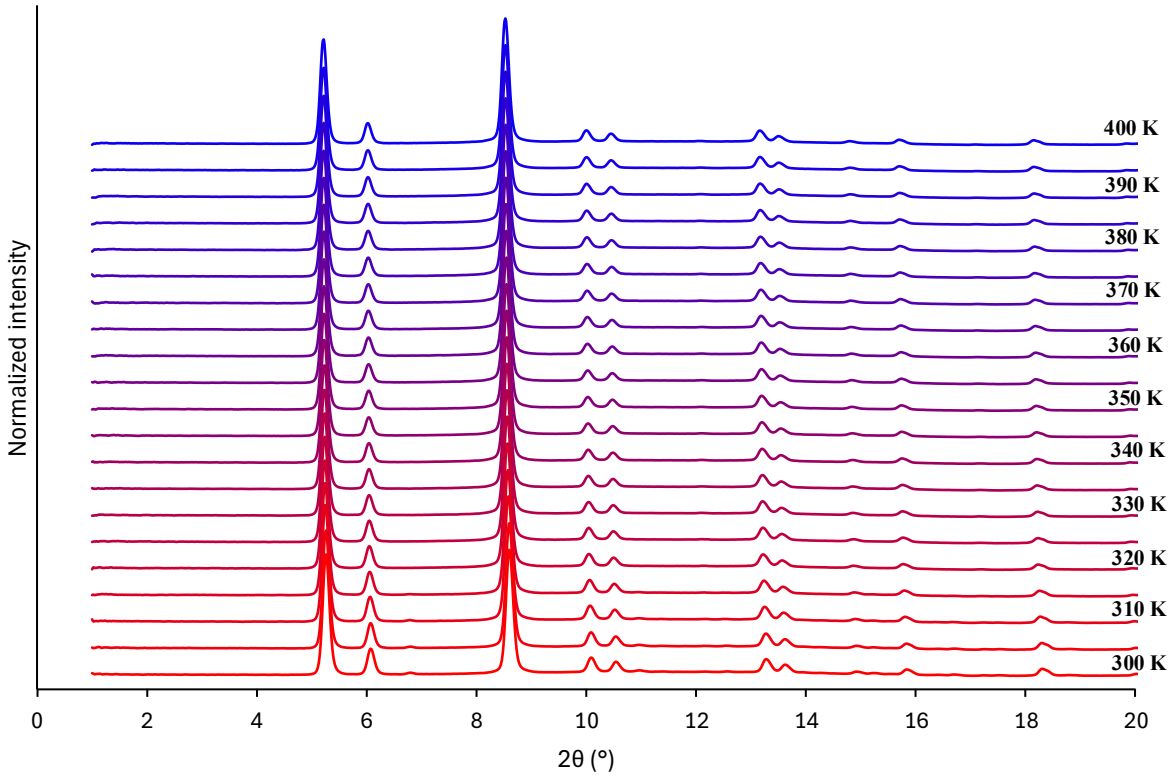

Figure 36. In situ powder patterns of TMPD measured under 11 bar of CO_2, starting at 300 K and gradually heating to end at 400 K.

Therefore, we attempted similar *in situ* measurements between 300 and 400 K, using an inert gas xenon abundant in electrons (i.e. X-ray scattering power), offering two key advantages. Firstly, its abundance of electrons makes it easily detectable in XRD and therefore the alterations in electronic densities are more pronounced, and secondly, being a single atom simplifies modeling in FOX for subsequent refinement. We implemented the temperature ramp protocol, as previously described, for conducting *in situ* measurements, under 11 bar of xenon. The resulting powder patterns are illustrated in *Figure 37*. Initially, the TMPD sample consisted of the two phases, including a small amount of the second polymorph. Surprisingly, upon the application of pressure, the simultaneous disappearance of the peaks related to the non-porous phase (at 7.3°, 8.0°, 9.3°, and 9.7°) was observed, suggesting a phase transition of the monoclinic TMPD towards the porous TMPD structure. Indeed, this behavior was not observed when heated without applying pressure. Moreover, a progressive modification in the relative intensities of the initial peaks at 5.2° and 6.1° with increasing time implies effective xenon sorption.

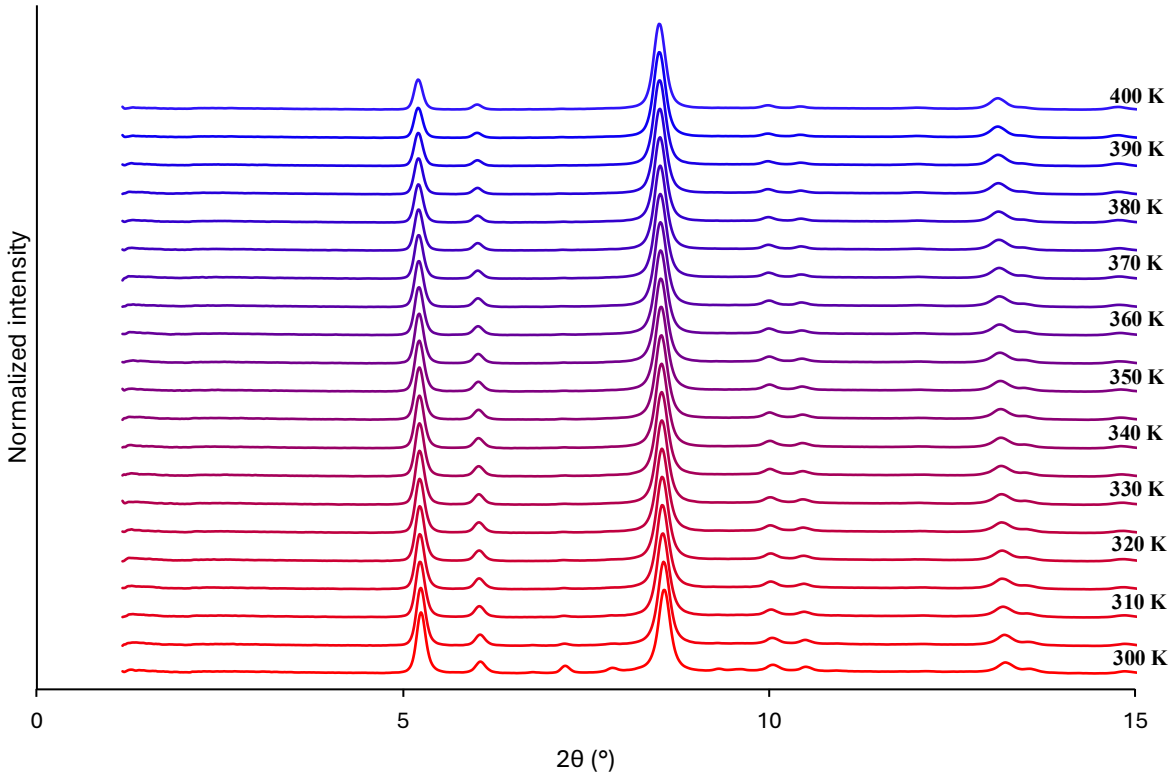

Figure 37. In situ powder patterns of TMPD, measured under 11 bar of Xe, starting at 300 K and gradually heating to end at 400 K.

Subsequent sequential refinement was performed on the occupancy of the Xe atom, revealing the increase of occupancy by 100 % between 320 and 400 K, further confirming sorption (*Figure 38*). TMPD crystallizes in the space group 205 ($P\,a\,\bar{3}$), whose special sites are depicted in the Appendix ***A12***. The multiplicity of a general site of this space group is 24, while the refined position of the Xe atom in the lattice is at coordinates 0, ½, 0 with a corresponding site multiplicity of 4. In FullProf, the maximum occupancy of a special site is determined by dividing the multiplicity of the special site by the multiplicity of the general site. Therefore, to find the amount of Xe atom per unit cell, the following formula was employed (10):

$$\text{Xe per unit cell} = \frac{Z\,.multiplicity\ of\ general\ site\ .\ Xe\ occupancy}{multiplicity\ of\ special\ site} \qquad (10)$$

Where Z is the number of formula unit present in the unit cell, which in our case is equal to 4 (refer to *S16*). We find 1.02 Xe per unit cell, meaning it has an occupancy of approximately 25 % of the available pores. This reveals a particularly interesting characteristic of the PIP

compound studied here: the amount of Xe sorbed increases with temperature, which goes against the typical behavior of most of the porous materials. Furthermore, the sorption plateau was never reached, indicating that the sorption process was not complete. This supports our conclusion that the adsorption kinetics is very slow, and that higher temperature is needed to improve it. The heavier Xe adsorbs well at higher temperatures, unlike lighter H_2 and CO_2, allowing to complete the experimental picture, validating our understanding of this unique system.

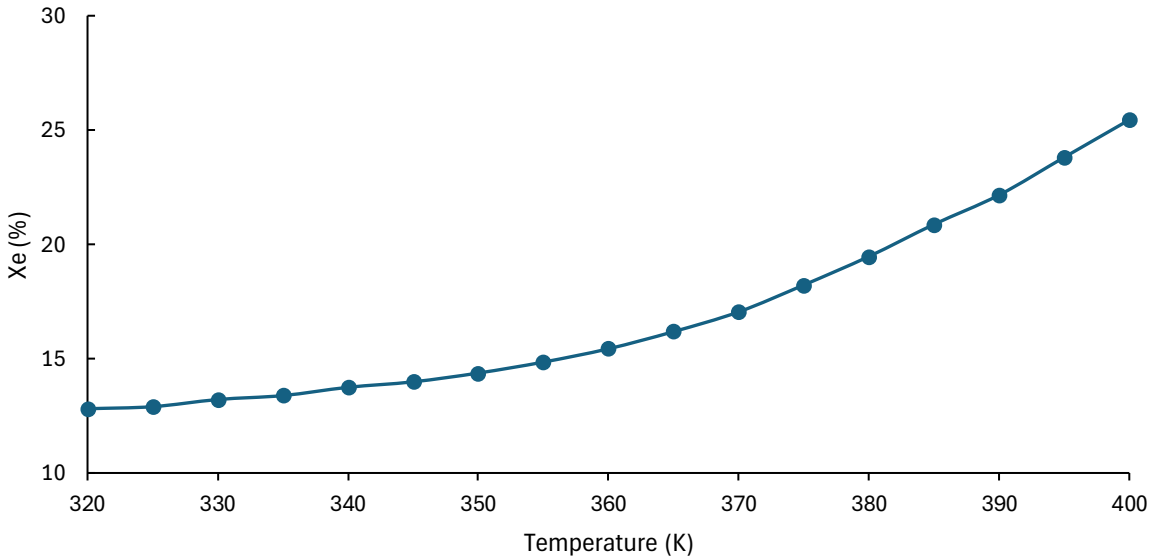

Figure 38. Sequential refinement of the Xenon occupancy between 320 and 400 K, under a constant 11 bar pressure of Xe. The saturation is not reached even at the highest temperature.

3.3. Dodecaborates with lower symmetry cations

3.3.1. (*t*-BuNH$_3$)$_3$B$_{12}$H$_{12}$·H$_2$O

We aimed to investigate the impact of lowering the symmetry of the cation on sorption kinetics, trying (*t*-BuNH$_3$)$^+$ as a cation. Regrettably, insufficient sample retrieval prevented us from conducting *in situ* PXRD measurements under gas pressure. However, we successfully solved the structure of the white single crystals mentioned in the synthesis section. The (*t*-BuNH$_3$)$_2$B$_{12}$H$_{12}$ crystallizes in a tetragonal cell, with a = 10.6 Å and c = 18.8 Å. As illustrated in the *Figure 39*, water becomes integrated into the crystal lattice, impeding pore formation.

The separation of 1.99 Å between the $H^{\delta+}$ atoms of the two *t*-$BuNH_3$ cations and the O of water molecule indicates the presence of a hydrogen bond. Additionally, the distance of 1.88 Å between the $H^{\delta-}$ of the dodecaborate and the $H^{\delta+}$ of H_2O implies the existence of dihydrogen bonds, further confirming the highly stabilized inclusion of water within this crystal structure. This knowledge of the hydrogen bonds has shed light on the significant solubility contrast between TMAD/TMPD and (*t*-$BuNH_3)_2B_{12}H_{12}$.

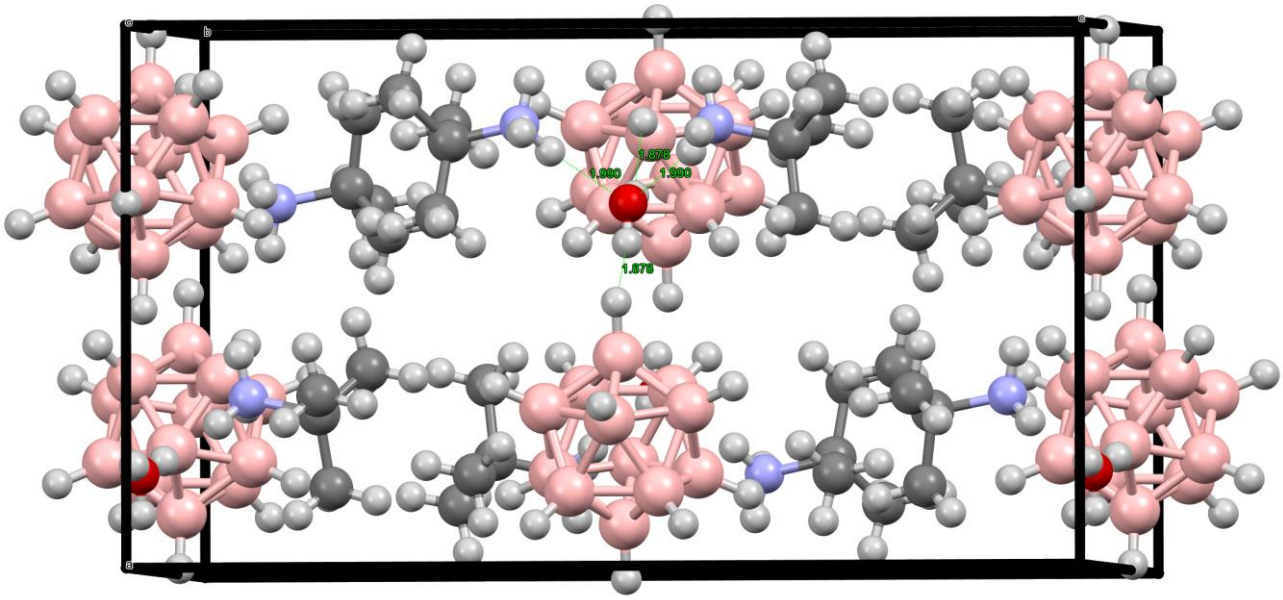

Figure 39. Crystal structure of (*t*-$BuNH_3)_2B_{12}H_{12}$. The hydrogen bonds are depicted in green. Color code: B = pinkish, C = dark grey, N = blue, O = red and H = light grey.

It is important to highlight that, following the full evaporation of the water solvent during synthesis, whitish single crystals were produced. The structure of these single crystals was also elucidated, revealing (*t*-$BuNH_3)_3B_{12}H_{12}Br$, whose structure is depicted in *Figure 40*. This structure adopts the P $2_1/c$ monoclinic space group and is characterized by lattice parameters a = 10.4 Å, b = 11.6 Å, c = 22.6 Å, and β = 93.5°. The bromide ions are impeding pore formation, making gas sorption impossible. Currently, attempts are ongoing to design a method for removing this bromine from the structure.

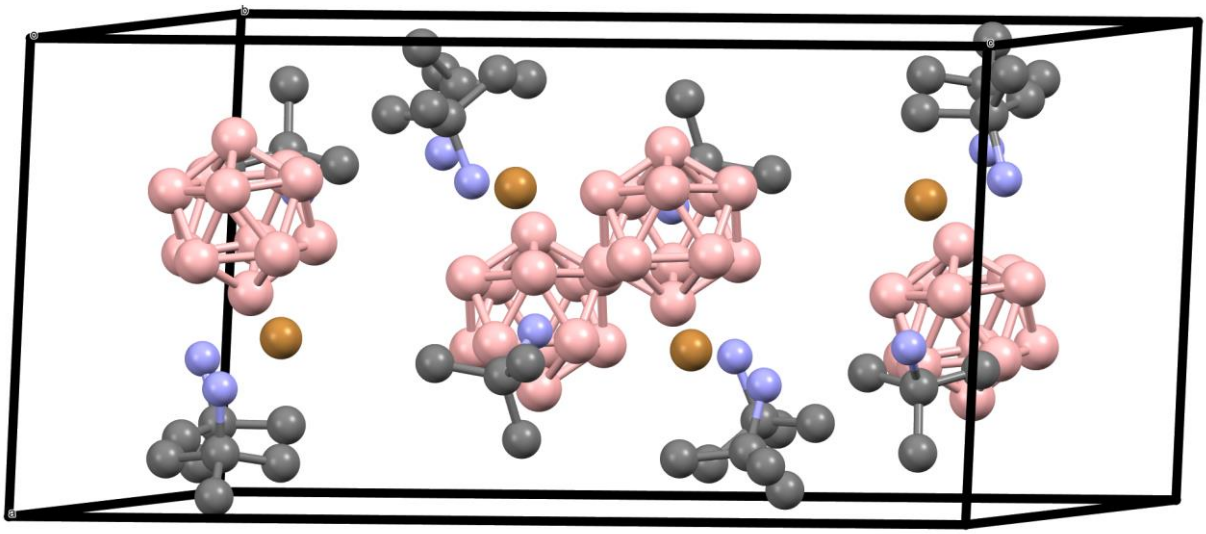

Figure 40. Crystal structure of (t-$BuNH_3$)$_3B_{12}H_{12}Br$ (hydrogens were removed for clarity). Color code: B = pinkish, C = grey, N = blue and Br = brown.

3.4. Other porous ionic packings

3.4.1. $(NMe_4)_2SnCl_4Br_2$

We conducted searches within crystallographic databases to explore the potential extension of the PIPs among non-boron compounds. Subsequently, we sought an isomorphous structure to TMAD and found $(NMe_4)_2SnCl_6$ (***A13***). The voids within this structure constitute roughly 2 % of the unit cell volume. Given the availability of NMe_4Br among our reagents (for the other syntheses), we proceeded with the synthesis according to the following equation (11):

$$SnCl_4 \cdot 5H_2O + 2\ NMe_4Br \rightarrow (NMe_4)_2SnCl_{4.7}Br_{1.3} \qquad (11)$$

We anticipated that the structure would resemble that of $(NMe_4)_2SnCl_6$. Following SC-XRD analysis on the single crystal obtained, our hypothesis was confirmed, the structure matching precisely, with 22 % of Br^- substituting Cl^-. The powder patterns are presented alongside a comparison of the diffractogram with the cubic TMAD and TMPD structures, in *Figure 41*. We could indeed notice that the powder patterns are close to identical.

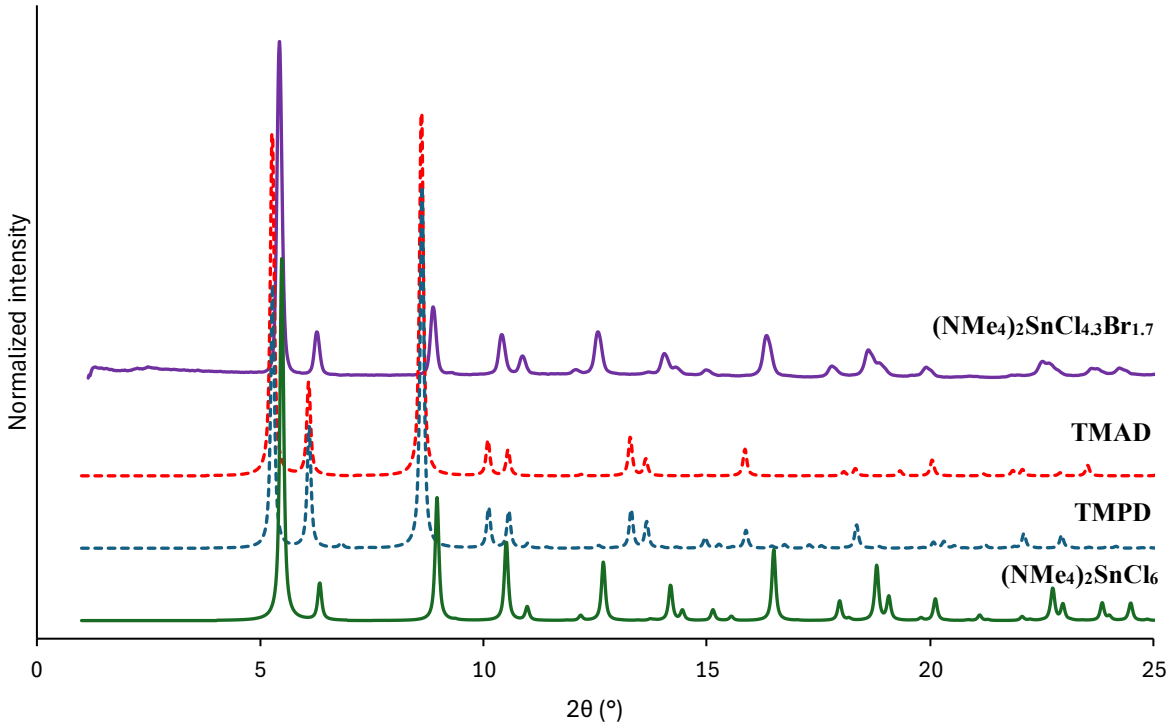

Figure 41. Comparison of the powder pattern of the synthesized $(NMe_4)_2SnCl_{4.3}Br_{1.7}$ with the theoretical powder patterns of TMAD, TMPD and $(NMe_4)_2SnCl_6$.

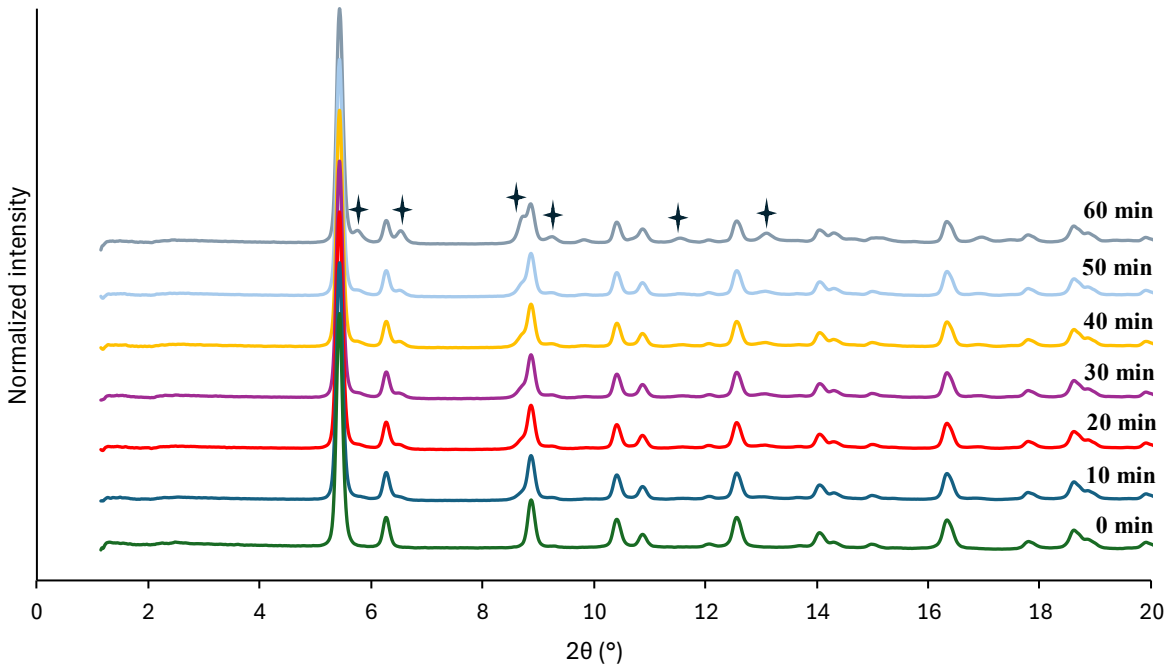

Figure 42. Evolution of the powder pattern of $(NMe_4)_2SnCl_{4.3}Br_{1.7}$ at 30 °C under a 7.1 bar of CO_2 pressure. One measurement was conducted every ten minutes, for an hour. The black stars indicate the formation of a new phase.

Following this, CO_2 sorption experiments were conducted on the $(NMe_4)_2SnCl_{4.7}Br_{1.3}$ under specific conditions: 30 °C at 7.1 bar of CO_2 pressure, with one measurement every ten minutes, for an hour. The results of the PXRD experiment are shown in *Figure 42*. Although there was no noticeable change in the relative intensity of peaks, the emergence of additional peaks at 5.7, 6.5, 8.7, 11.5 and 13.2 ° were observed, indicating a pressure-induced phase transition once again. Given the absence of the gas sorption by the main phase, we stopped further studies of this system.

4. Conclusion and perspectives

4.1. Summary of findings

The focus of this master's thesis revolved around three primary objectives related to PIP synthesis, characterization, and sorption performance: (1) understanding the formation of TMAD and optimizing its synthesis, (2) exploring the versatility of the PIP concept by modifying ions to synthesize additional PIPs, and (3) investigating gas sorption in the PIPs using volumetric and diffraction methods.

Concerning the first objective, characterization techniques (XRD, NMR, IR) confirmed the successful synthesis of *fcc* TMAD. We observed that synthesis conditions play a crucial role. Specifically, variations in water temperature during synthesis resulted in different relative intensities of *fcc* TMAD peaks, accompanied by a shift of the first peak to lower 2θ values, indicating lattice expansion attributed to water present within the pores. Notably, TMAD synthesized in hot water revealed an additional phase whose structure remains unidentified. Hence, this study revealed that to maximize the yield of *fcc* TMAD, the synthesis should be conducted in cold water, using the minimum amount necessary to dissolve $Na_2B_{12}H_{12}$·4diglyme and NMe_4Br, followed by the mixing of these cold solutions.

Concerning the second objective, demonstration of the robustness of the PIP concept was evidenced by the successful synthesis of another PIP, $(PMe_4)_2B_{12}H_{12}$ (TMPD). This compound exhibited two distinct phases, both solved through SC-XRD: an *fcc* porous phase, akin to TMAD, and a monoclinic non-porous phase, characterized by twinning. Remarkably, the *fcc* porous phase proved more stable than the non-porous one. Similar to TMAD, this compound displayed varying relative peak intensities depending on whether it was synthesized in hot or cold water, meaning they possessed different water contents within their respective pores. Furthermore, synthesis in hot water resulted in the appearance of the second phase, whereas synthesis in cold water exclusively yielded the *fcc* TMPD. The TG-DTA reveals that TMPD remains stable up to 420°C, surpassing the stability of TMAD by approximately 100°C. Very similar unit cell volumes for the *fcc* TMAD and TMPD seen along the smaller pores in TMPD suggest that the unit cell volume is defined by the repulsive packing of anions and the larger PMe_4^+ cations are taking more remaining space, leaving smaller voids.

We also conducted the synthesis using the lower symmetry cation *t*-$BuNH_3^+$. Unfortunately, we were unable to synthesize (*t*-$BuNH_3)_2B_{12}H_{12}$; however, we successfully obtained tetragonal (*t*-$BuNH_3)_2B_{12}H_{12}\cdot H_2O$ and monoclinic (*t*-$BuNH_3)_3B_{12}H_{12}Br$. We demonstrated that water is significantly stabilized within the framework of (*t*-$BuNH_3)_2B_{12}H_{12}\cdot H_2O$ due to the presence of both hydrogen and dihydrogen bonds, facilitated by the availability of the charge of the nitrogen of *t*-$BuNH_3^+$, compared to NMe_4^+. In the absence of methyl groups, there is reduced steric hindrance, allowing the charge to be more accessible on the nitrogen atom. Additionally, the charge is less delocalized compared to NMe_4^+, where it is spread throughout the entire tetrahedron. Therefore, in *t*-$BuNH_3^+$, the charge is more localized on the nitrogen atom, facilitating such hydrogen interactions. Both structures are non-porous, the former contains H_2O while the latter contains Br^-, hindering the formation of pores within the crystal lattice. Upon exposure to air for three weeks, TMAD effectively sorbed water. DVS measurements further demonstrated TMAD's ability to sorb water under specific relative humidities, albeit exhibiting slow desorption.

Concerning the third objective, we confirmed the gas sorption in PIPs. The process is much slower than for classical porous materials, well in accord with the fact that the pores are not interconnected in PIPs, creating great obstacles for gas diffusion. Despite the presence of similarly sized voids, no effective sorption was observed on $Cs_2B_{12}H_{12}$, validating the theory that the nature of the cation is crucial for gas sorption. We hypothesize that the paddle-and-wheel mechanism involving the organic cation allows for the slow gas diffusion and thus adsorption in the title PIPs. Cesium atoms has a spherical symmetry and is not allowing for this mechanism.

We conducted CO_2 and H_2 PXRD and sorption measurements on TMAD at room temperature, demonstrating its ability to sorb 5.92 and 0.21 wt%, respectively. However, refinement of the data to determine the exact amount and location of CO_2 inside the pores was hindered by structural disorder. Neutron diffraction at 77 K was unfortunately too slow to get any notable D_2 adsorption. The kinetics for CO_2 sorption was very slow, failing to reach a plateau during measurement; thus, we plan to restart the measurement with extended equilibrium pressure times or elevating the temperature, to increase the sorption rate, at the expense of the amounts adsorbed. Conversely, H_2 sorption kinetics at room temperature was satisfactory, reaching equilibrium pressure for each measurement point.

Both TMAD and TMPD exhibit a phase transition when subjected to 10 bar of CO_2 or Xe pressure, transitioning from a non-porous to the *fcc* porous phase. XRD measurements on TMPD to probe CO_2 and Xe sorption revealed a change in relative intensities, indicating effective sorption of both gases. Although CO_2 refinement was hindered by disorder similarly to TMAD, sequential refinement on Xe was possible, providing valuable insights: sorption reached 25 % of pore availability when TMPD was subjected to 11 bar of Xe for one hour at temperatures increasing from 300 K to 400 K, with sorption increasing as temperature rose - a behavior not commonly observed for porous materials.

As the crystal structures of $(t\text{-BuNH}_3)_2B_{12}H_{12}\cdot H_2O$ and $(t\text{-BuNH}_3)_3B_{12}H_{12}Br$ lacked pores, conducting gas sorption on these compounds was not feasible. Current endeavors are focused on removing the H_2O and Br^- from the crystal structure of these compounds to yield $(t\text{-BuNH}_3)_2B_{12}H_{12}$. Consequently, we were unable to evaluate the impact of lowering the cation symmetry on the gas sorption of the PIPs.

Finally, we attempted to exchange the anion to investigate the impact of the lower symmetry anion $[SnCl_{4.7}Br_{1.3}]^{2-}$ on gas sorption. The structure obtained corresponded to a *fcc* anti-CaF_2-type lattice with voids, as solved by SC-XRD. Upon attempting CO_2 sorption on this new compound at 7.1 bar, instead of observing gas sorption as anticipated, we encountered a phase transition, the structure of which remains unidentified to date.

4.2. Future directions

The possibilities are vast for this emerging class of compounds. By adjusting the size ratio between ions, for instance, substituting $B_{12}H_{12}$ with $B_{12}X_{12}$ or $B_{12}(OR)_{12}$, we could customize pore size, envisioning a diverse series of porous ionic packings (*Figure 43*). Varying ion sizes should enable not only pore size adjustment but also modulation of the chemical properties of the inner pore surface, enhancing interaction with guest molecules in the PIPs.

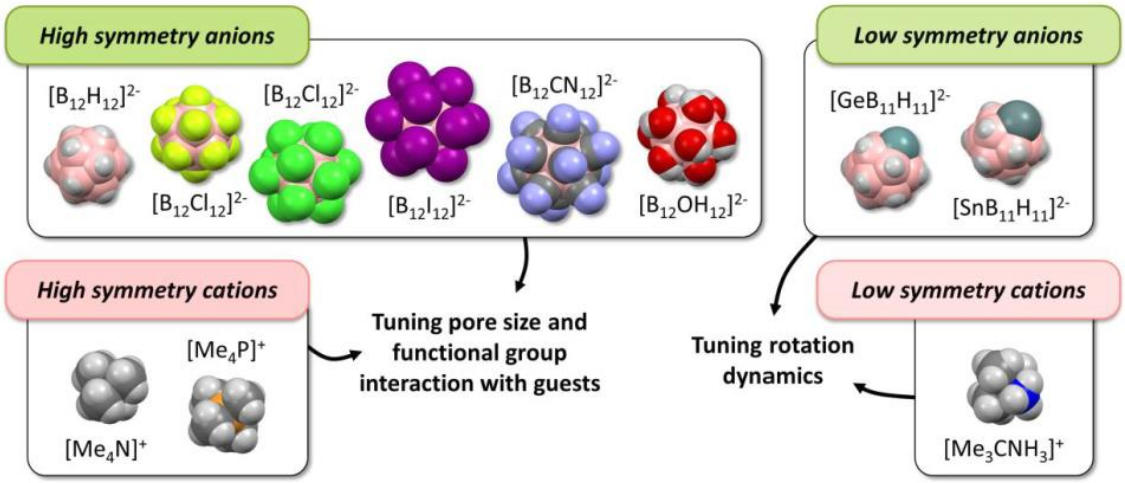

Figure 43. Selection of ions for building future porous ionic packings.

Furthermore, the slow kinetics observed could be leveraged as an advantage. If we identify an external stimulus capable of controlling PIPs' sorption kinetics, such as electromagnetic irradiation or vibrational energy, we could foresee their application in separation processes or for storage of gasses in a “trapped” state. Study of structural dynamics, such as reorientational motion by spin-lattice relaxation with solid-state NMR or by quasi-elastic neutron scattering can answer if the paddle-and-wheel mechanism is driving gas diffusion and adsorption in the title Pips. We are on the brink of an exciting, unknown realm, and it is undeniable that the discussion surrounding PIPs is just getting started.

5. References

(1) Mota, J. P. B. Impact of Gas Composition on Natural Gas Storage by Adsorption. *AIChE J.* **1999**, *45* (5), 986–996. https://doi.org/10.1002/aic.690450509.

(2) Wang, Y.; Li, Y. Sorption-Enhanced Steam Gasification of Biomass for H2-Rich Gas Production and in-Situ CO2 Capture by CaO-Based Sorbents: A Critical Review. *Appl. Energy Combust. Sci.* **2023**, *14*, 100124. https://doi.org/10.1016/j.jaecs.2023.100124.

(3) Choi, K. M.; Jeong, H. M.; Park, J. H.; Zhang, Y.-B.; Kang, J. K.; Yaghi, O. M. Supercapacitors of Nanocrystalline Metal-Organic Frameworks. *ACS Nano* **2014**, *8* (7), 7451–7457. https://doi.org/10.1021/nn5027092.

(4) *Energy Technology Perspectives 2016 – Analysis*. IEA. https://www.iea.org/reports/energy-technology-perspectives-2016 (accessed 2024-04-19).

(5) *Global Status of CCS Report: 2020*. Global CCS Institute. https://www.globalccsinstitute.com/resources/publications-reports-research/global-status-of-ccs-report-2020/ (accessed 2024-04-19).

(6) Waller, L.; Rayner, T.; Chilvers, J.; Gough, C.; Lorenzoni, I.; Jordan, A.; Vaughan, N. Contested Framings of Greenhouse Gas Removal and Its Feasibility: Social and Political Dimensions. *Wiley Interdiscip. Rev. Clim. Change* **2020**, *11* (4). https://doi.org/10.1002/wcc.649.

(7) Fridahl, M.; Lehtveer, M. Bioenergy with Carbon Capture and Storage (BECCS): Global Potential, Investment Preferences, and Deployment Barriers. *Energy Res. Soc. Sci.* **2018**, *42*, 155–165. https://doi.org/10.1016/j.erss.2018.03.019.

(8) *Commission opens €4 billion call for proposals for net-zero technologies under the Innovation Fund - European Commission*. https://managenergy.ec.europa.eu/managenergy-discover/news/commission-opens-eu4-billion-call-proposals-net-zero-technologies-under-innovation-fund-2024-04-05_en (accessed 2024-05-15).

(9) Palys, M. J.; Daoutidis, P. Power-to-X: A Review and Perspective. *Comput. Chem. Eng.* **2022**, *165*, 107948. https://doi.org/10.1016/j.compchemeng.2022.107948.

(10) Abreu, J. M.; Câmara Pereira, F.; Ferrão, P. Using Pattern Recognition to Identify Habitual Behavior in Residential Electricity Consumption. *Energy Build.* **2012**, *49*, 479–487. https://doi.org/10.1016/j.enbuild.2012.02.044.

(11) Niaz, S.; Manzoor, T.; Pandith, A. H. Hydrogen Storage: Materials, Methods and Perspectives. *Renew. Sustain. Energy Rev.* **2015**, *50*, 457–469. https://doi.org/10.1016/j.rser.2015.05.011.

(12) Yang, M.; Hunger, R.; Berrettoni, S.; Sprecher, B.; Wang, B. A Review of Hydrogen Storage and Transport Technologies. *Clean Energy* **2023**, *7* (1), 190–216. https://doi.org/10.1093/ce/zkad021.

(13) Arcos, J. M. M.; Santos, D. M. F. The Hydrogen Color Spectrum: Techno-Economic Analysis of the Available Technologies for Hydrogen Production. *Gases* **2023**, *3* (1), 25–46. https://doi.org/10.3390/gases3010002.

(14) *The Geopolitics of Hydrogen*. Stiftung Wissenschaft und Politik (SWP). https://www.swp-berlin.org/publikation/the-geopolitics-of-hydrogen (accessed 2024-05-16).

(15) Dou, Y.; Sun, L.; Ren, J.; Dong, L. Chapter 17 - Opportunities and Future Challenges in Hydrogen Economy for Sustainable Development. In *Hydrogen Economy (Second Edition)*; Scipioni, A., Manzardo, A., Ren, J., Eds.; Academic Press, 2023; pp 537–569. https://doi.org/10.1016/B978-0-323-99514-6.00008-X.

(16) Dincer, I.; Acar, C. Innovation in Hydrogen Production. *Int. J. Hydrog. Energy* **2017**, *42* (22), 14843–14864. https://doi.org/10.1016/j.ijhydene.2017.04.107.

(17) Tarhan, C.; Çil, M. A. A Study on Hydrogen, the Clean Energy of the Future: Hydrogen Storage Methods. *J. Energy Storage* **2021**, *40*, 102676. https://doi.org/10.1016/j.est.2021.102676.

(18) Nazir, G.; Rehman, A.; Hussain, S.; Aftab, S.; Heo, K.; Ikram, M.; Patil, S. A.; Aizaz Ud Din, M. Recent Advances and Reliable Assessment of Solid-State Materials for Hydrogen Storage: A Step Forward toward a Sustainable H2 Economy. *Adv. Sustain. Syst.* **2022**, *6* (11), 2200276. https://doi.org/10.1002/adsu.202200276.

(19) Calvert, J. G. Glossary of Atmospheric Chemistry Terms (Recommendations 1990). *Pure Appl. Chem.* **1990**, *62* (11), 2167–2219. https://doi.org/10.1351/pac199062112167.

(20) Králik, M. Adsorption, Chemisorption, and Catalysis. *Chem. Pap.* **2014**, *68*. https://doi.org/10.2478/s11696-014-0624-9.

(21) Choi, J.-G.; Do, D. D.; Do, H. D. Surface Diffusion of Adsorbed Molecules in Porous Media: Monolayer, Multilayer, and Capillary Condensation Regimes. *Ind. Eng. Chem. Res.* **2001**, *40* (19), 4005–4031. https://doi.org/10.1021/ie010195z.

(22) Thommes, M.; Kaneko, K.; Neimark, A. V.; Olivier, J. P.; Rodriguez-Reinoso, F.; Rouquerol, J.; Sing, K. S. W. Physisorption of Gases, with Special Reference to the Evaluation of Surface Area and Pore Size Distribution (IUPAC Technical Report). *Pure Appl. Chem.* **2015**, *87* (9–10), 1051–1069. https://doi.org/10.1515/pac-2014-1117.

(23) Chorover, J.; Brusseau, M. L. Kinetics of Sorption—Desorption. In *Kinetics of Water-Rock Interaction*; Brantley, S. L., Kubicki, J. D., White, A. F., Eds.; Springer: New York, NY, 2008; pp 109–149. https://doi.org/10.1007/978-0-387-73563-4_4.

(24) Murphy, C. M.; O'Brien, F. J. Understanding the Effect of Mean Pore Size on Cell Activity in Collagen-Glycosaminoglycan Scaffolds. *Cell Adhes. Migr.* **2010**, *4* (3), 377–381. https://doi.org/10.4161/cam.4.3.11747.

(25) Mohammed Mohammed, A. H.; Shariff, K. A.; Wahjuningrum, D. A.; Bakar, M. H. A.; Mohamad, H. A Comprehensive Review of the Effects of Porosity and Macro- and

Micropore Formations in Porous β-TCP Scaffolds on Cell Responses. *J. Aust. Ceram. Soc.* **2023**, *59* (4), 865–879. https://doi.org/10.1007/s41779-023-00880-0.

(26) Sing, K. S. W. Characterization Of Porous Solids: An Introductory Survey. In *Studies in Surface Science and Catalysis*; Rodriguez-Reinoso, F., Rouquerol, J., Sing, K. S. W., Unger, K. K., Eds.; Characterization of Porous Solids II; Elsevier, 1991; Vol. 62, pp 1–9. https://doi.org/10.1016/S0167-2991(08)61303-8.

(27) Rigby, S. P. Gas Sorption. In *Structural Characterisation of Natural and Industrial Porous Materials: A Manual*; Rigby, S. P., Ed.; Springer International Publishing: Cham, 2020; pp 15–48. https://doi.org/10.1007/978-3-030-47418-8_2.

(28) Strangfeld, C.; Wiehle, P.; Munsch, S. M. About the Dominance of Mesopores in Physisorption in Amorphous Materials. *Molecules* **2021**, *26* (23), 7190. https://doi.org/10.3390/molecules26237190.

(29) Grebennikov, S. F.; Ibragimova, R. I.; Lysenko, A. A. Application of the Theory of Volume Filling of Micropores to Analysis of the Structure of Nanoporous Fibers and Properties of Swelling Fiber-Forming Polymers. *Fibre Chem.* **2019**, *51* (1), 45–56. https://doi.org/10.1007/s10692-019-10045-0.

(30) Cychosz, K.; Thommes, M. Progress in the Physisorption Characterization of Nanoporous Gas Storage Materials. *Engineering* **2018**, *4*. https://doi.org/10.1016/j.eng.2018.06.001.

(31) Kordala, N.; Wyszkowski, M. Zeolite Properties, Methods of Synthesis, and Selected Applications. *Molecules* **2024**, *29* (5), 1069. https://doi.org/10.3390/molecules29051069.

(32) Steenhaut, T.; Filinchuk, Y.; Hermans, S. Aluminium-Based MIL-100(Al) and MIL-101(Al) Metal–Organic Frameworks, Derivative Materials and Composites: Synthesis, Structure, Properties and Applications. *J. Mater. Chem. A* **2021**, *9* (38), 21483–21509. https://doi.org/10.1039/D1TA04444C.

(33) Severino, M. I.; Gkaniatsou, E.; Nouar, F.; Pinto, M. L.; Serre, C. MOFs Industrialization: A Complete Assessment of Production Costs. *Faraday Discuss.* **2021**, *231* (0), 326–341. https://doi.org/10.1039/D1FD00018G.

(34) Pérez-Pellitero, J.; Pirngruber, G. D. Industrial Zeolite Applications for Gas Adsorption and Separation Processes. In *New Developments in Adsorption/Separation of Small Molecules by Zeolites*; Valencia, S., Rey, F., Eds.; Springer International Publishing: Cham, 2020; pp 195–225. https://doi.org/10.1007/430_2020_75.

(35) Salahudeen, N. A Review on Zeolite: Application, Synthesis and Effect of Synthesis Parameters on Product Properties. *Chem. Afr.* **2022**, *5* (6), 1889–1906. https://doi.org/10.1007/s42250-022-00471-9.

(36) Bacakova, L.; Vandrovcova, M.; Kopova, I.; Jirka, I. Applications of Zeolites in Biotechnology and Medicine – a Review. *Biomater. Sci.* **2018**, *6* (5), 974–989. https://doi.org/10.1039/C8BM00028J.

(37) Gao, Z. R.; Yu, H.; Chen, F.-J.; Mayoral, A.; Niu, Z.; Niu, Z.; Li, X.; Deng, H.; Márquez-Álvarez, C.; He, H.; Xu, S.; Zhou, Y.; Xu, J.; Xu, H.; Fan, W.; Balestra, S. R. G.; Ma, C.; Hao, J.; Li, J.; Wu, P.; Yu, J.; Camblor, M. A. Interchain-Expanded Extra-Large-Pore Zeolites. *Nature* **2024**, *628* (8006), 99–103. https://doi.org/10.1038/s41586-024-07194-6.

(38) Vinaches, P.; Bernardo-Gusmao, K.; Pergher, S. An Introduction to Zeolite Synthesis Using Imidazolium-Based Cations as Organic Structure-Directing Agents. *Molecules* **2017**, *22*, 1307. https://doi.org/10.3390/molecules22081307.

(39) Wang, S.; Peng, Y. Natural Zeolites as Effective Adsorbents in Water and Wastewater Treatment. *Chem. Eng. J.* **2010**, *156* (1), 11–24. https://doi.org/10.1016/j.cej.2009.10.029.

(40) Li, J.; Gao, M.; Yan, W.; Yu, J. Regulation of the Si/Al Ratios and Al Distributions of Zeolites and Their Impact on Properties. *Chem. Sci.* **2023**, *14* (8), 1935–1959. https://doi.org/10.1039/D2SC06010H.

(41) Smith, D. W. B., J. V. *Molecular Sieves*. Scientific American. https://www.scientificamerican.com/article/molecular-sieves/ (accessed 2024-05-18).

(42) *IUPAC Provisional Recommendations on Metal-Organic Framework and Coordination Polymer Terminology – CrystEngComm Blog*. https://blogs.rsc.org/ce/2013/01/08/iupac-provisional-recommendations-on-metal-organic-framework-and-coordination-polymer-terminology/ (accessed 2024-05-24).

(43) Fonseca, J.; Gong, T.; Jiao, L.; Jiang, H.-L. Metal–Organic Frameworks (MOFs) beyond Crystallinity: Amorphous MOFs, MOF Liquids and MOF Glasses. *J. Mater. Chem. A* **2021**, *9* (17), 10562–10611. https://doi.org/10.1039/D1TA01043C.

(44) Bennett, T. D.; Cheetham, A. K. Amorphous Metal–Organic Frameworks. *Acc. Chem. Res.* **2014**, *47* (5), 1555–1562. https://doi.org/10.1021/ar5000314.

(45) Lin, K.-S.; Adhikari, A. K.; Ku, C.-N.; Chiang, C.-L.; Kuo, H. Synthesis and Characterization of Porous HKUST-1 Metal Organic Frameworks for Hydrogen Storage. *Int. J. Hydrog. Energy* **2012**, *37* (18), 13865–13871. https://doi.org/10.1016/j.ijhydene.2012.04.105.

(46) Hamon, L.; Serre, C.; Devic, T.; Loiseau, T.; Millange, F.; Férey, G.; Weireld, G. D. Comparative Study of Hydrogen Sulfide Adsorption in the MIL-53(Al, Cr, Fe), MIL-47(V), MIL-100(Cr), and MIL-101(Cr) Metal−Organic Frameworks at Room Temperature. *J. Am. Chem. Soc.* **2009**, *131* (25), 8775–8777. https://doi.org/10.1021/ja901587t.

(47) Peng, X.; Chen, L.; Li, Y. Ordered Macroporous MOF-Based Materials for Catalysis. *Mol. Catal.* **2022**, *529*, 112568. https://doi.org/10.1016/j.mcat.2022.112568.

(48) Chakraborty, D.; Musib, D.; Saha, R.; Das, A.; Raza, M. K.; Ramu, V.; Chongdar, S.; Sarkar, K.; Bhaumik, A. Highly Stable Tetradentate Phosphonate-Based Green Fluorescent Cu-MOF for Anticancer Therapy and Antibacterial Activity. *Mater. Today Chem.* **2022**, *24*, 100882. https://doi.org/10.1016/j.mtchem.2022.100882.

(49) Felix Sahayaraj, A.; Joy Prabu, H.; Maniraj, J.; Kannan, M.; Bharathi, M.; Diwahar, P.; Salamon, J. Metal–Organic Frameworks (MOFs): The Next Generation of Materials for

Catalysis, Gas Storage, and Separation. *J. Inorg. Organomet. Polym. Mater.* **2023**, *33* (7), 1757–1781. https://doi.org/10.1007/s10904-023-02657-1.

(50) Zhao, D.; Thallapally, P. K.; Petit, C.; Gascon, J. Advanced Porous Materials: Design, Synthesis, and Applications in Sustainability. *ACS Sustain. Chem. Eng.* **2019**, *7*, 7997–7998. https://doi.org/10.1021/acssuschemeng.9b02021.

(51) Ding, M.; Cai, X.; Jiang, H.-L. Improving MOF Stability: Approaches and Applications. *Chem. Sci.* **2019**, *10* (44), 10209–10230. https://doi.org/10.1039/C9SC03916C.

(52) Introduction to Metal–Organic Frameworks. *Chem. Rev.* **2012**, *112* (2), 673–674. https://doi.org/10.1021/cr300014x.

(53) Liu, X.; Qian, B.; Zhang, D.; Yu, M.; Chang, Z.; Bu, X. Recent Progress in Host–Guest Metal–Organic Frameworks: Construction and Emergent Properties. *Coord. Chem. Rev.* **2023**, *476*, 214921. https://doi.org/10.1016/j.ccr.2022.214921.

(54) Guo, K. Applications of Metal-Organic Frameworks in Methane Storage. *Highlights Sci. Eng. Technol.* **2023**, *58*, 338–343. https://doi.org/10.54097/hset.v58i.10120.

(55) Healy, C.; Patil, K. M.; Wilson, B. H.; Hermanspahn, L.; Harvey-Reid, N. C.; Howard, B. I.; Kleinjan, C.; Kolien, J.; Payet, F.; Telfer, S. G.; Kruger, P. E.; Bennett, T. D. The Thermal Stability of Metal-Organic Frameworks. *Coord. Chem. Rev.* **2020**, *419*, 213388. https://doi.org/10.1016/j.ccr.2020.213388.

(56) Antwi-Baah, R.; Liu, H. Recent Hydrophobic Metal-Organic Frameworks and Their Applications. *Mater. Basel Switz.* **2018**, *11* (11), 2250. https://doi.org/10.3390/ma11112250.

(57) Low, J. J.; Benin, A. I.; Jakubczak, P.; Abrahamian, J. F.; Faheem, S. A.; Willis, R. R. Virtual High Throughput Screening Confirmed Experimentally: Porous Coordination Polymer Hydration. *J. Am. Chem. Soc.* **2009**, *131* (43), 15834–15842. https://doi.org/10.1021/ja9061344.

(58) Kroto, H. W.; Heath, J. R.; O'Brien, S. C.; Curl, R. F.; Smalley, R. E. C60: Buckminsterfullerene. *Nature* **1985**, *318* (6042), 162–163. https://doi.org/10.1038/318162a0.

(59) Smalley, R. E. Great Balls of Carbon. *The Sciences* **1991**, *31* (2), 22–28. https://doi.org/10.1002/j.2326-1951.1991.tb02291.x.

(60) Shevlin, P. B. Lecture Notes on Fullerene Chemistry: A Handbook for Chemists By Roger Taylor (University of Sussex). Imperial College Press: London. 1999. Xiv + 268 Pp. $48.00. ISBN 1-86094-104-4. *J. Am. Chem. Soc.* **2000**, *122* (19), 4846–4846. https://doi.org/10.1021/ja9957635.

(61) Pan, Y.; Liu, X.; Zhang, W.; Liu, Z.; Zeng, G.; Shao, B.; Liang, Q.; He, Q.; Yuan, X.; Huang, D.; Chen, M. Advances in Photocatalysis Based on Fullerene C60 and Its Derivatives: Properties, Mechanism, Synthesis, and Applications. *Appl. Catal. B Environ.* **2020**, *265*, 118579. https://doi.org/10.1016/j.apcatb.2019.118579.

(62) Coro, J.; Suárez, M.; Silva, L. S. R.; Eguiluz, K. I. B.; Salazar-Banda, G. R. Fullerene Applications in Fuel Cells: A Review. *Int. J. Hydrog. Energy* **2016**, *41* (40), 17944–17959. https://doi.org/10.1016/j.ijhydene.2016.08.043.

(63) Bosi, S.; Da Ros, T.; Spalluto, G.; Prato, M. Fullerene Derivatives: An Attractive Tool for Biological Applications. *Eur. J. Med. Chem.* **2003**, *38* (11), 913–923. https://doi.org/10.1016/j.ejmech.2003.09.005.

(64) Omacrsawa, E. *Perspectives of Fullerene Nanotechnology*; Springer Science & Business Media, 2012.

(65) Fowler, P. W. Fullerene Stability and Structure. *Contemp. Phys.* **1996**, *37* (3), 235–247. https://doi.org/10.1080/00107519608217530.

(66) Tong, W. M.; Ohlberg, D. A. A.; You, H. K.; Williams, R. S.; Anz, S. J.; Alvarez, M. M.; Whetten, R. L.; Rubin, Y.; Diederich, F. N. X-Ray Diffraction and Electron Spectroscopy of Epitaxial Molecular Buckminsterfullerene Films. *J. Phys. Chem.* **1991**, *95* (12), 4709–4712. https://doi.org/10.1021/j100165a022.

(67) Gadd, G. E.; Evans, P. J.; Kennedy, S.; James, M.; Elcombe, M.; Cassidy, D.; Moricca, S.; Holmes, J.; Webb, N.; Dixon, A.; Prasad, P. Gas Storage in Fullerenes. *Fuller. Sci. Technol.* **1999**, *7* (6), 1043–1143. https://doi.org/10.1080/10641229909350304.

(68) Shannon, R. D. Revised Effective Ionic Radii and Systematic Studies of Interatomic Distances in Halides and Chalcogenides. *Acta Crystallogr. A* **1976**, *32* (5), 751–767. https://doi.org/10.1107/S0567739476001551.

(69) Verdal et al, N. Hydrogen Dynamics of the Dodecahydro-Closo-Dodecaborate Crystals. *Am. Chem. Soc.* **2011**, *Division fuel chemistry*.

(70) Cerny, R.; Brighi, M.; Murgia, F. The Crystal Chemistry of Inorganic Hydroborates. *Chemistry* **2020**, *2*, 805–826. https://doi.org/10.3390/chemistry2040053.

(71) Akrouchi, A.; Benzidi, H.; Al-Shami, A.; Kenz, A. E.; Benyoussef, A.; Kharbachi, A. E.; Mounkachi, O. First-Principles Study of Closo-Dodecaborates M2B12H12 (M = Li, Na, K) as Solid-State Electrolyte Materials. *Phys. Chem. Chem. Phys.* **2021**, *23* (47), 27014–27023. https://doi.org/10.1039/D1CP03215A.

(72) He, L.; Li, H.-W.; Nakajima, H.; Tumanov, N.; Filinchuk, Y.; Hwang, S.-J.; Sharma, M.; Hagemann, H.; Akiba, E. Synthesis of a Bimetallic Dodecaborate LiNaB12H12 with Outstanding Superionic Conductivity. *Chem. Mater.* **2015**, *27* (16), 5483–5486. https://doi.org/10.1021/acs.chemmater.5b01568.

(73) Kaneko, K.; Ishii, C.; Arai, T.; Suematsu, H. Defect-Associated Microporous Nature of Fullerene C60 Crystals. *J. Phys. Chem.* **1993**, *97* (26), 6764–6766. https://doi.org/10.1021/j100128a002.

(74) Bannenberg, L. J.; Heere, M.; Benzidi, H.; Montero, J.; Dematteis, E. M.; Suwarno, S.; Jaroń, T.; Winny, M.; Orłowski, P. A.; Wegner, W.; Starobrat, A.; Fijałkowski, K. J.; Grochala, W.; Qian, Z.; Bonnet, J.-P.; Nuta, I.; Lohstroh, W.; Zlotea, C.; Mounkachi, O.; Cuevas, F.; Chatillon, C.; Latroche, M.; Fichtner, M.; Baricco, M.; Hauback, B. C.; El

Kharbachi, A. Metal (Boro-) Hydrides for High Energy Density Storage and Relevant Emerging Technologies. *Int. J. Hydrog. Energy* **2020**, *45* (58), 33687–33730. https://doi.org/10.1016/j.ijhydene.2020.08.119.

(75) Liu, J.; Ma, Y.; Yang, J.; Sun, L.; Guo, D.; Xiao, P. Recent Advance of Metal Borohydrides for Hydrogen Storage. *Front. Chem.* **2022**, *10*, 945208. https://doi.org/10.3389/fchem.2022.945208.

(76) Oh, H.; Tumanov, N.; Ban, V.; Li, X.; Richter, B.; Hudson, M. R.; Brown, C. M.; Iles, G. N.; Wallacher, D.; Jorgensen, S. W.; Daemen, L.; Balderas-Xicohténcatl, R.; Cheng, Y.; Ramirez-Cuesta, A. J.; Heere, M.; Posada-Pérez, S.; Hautier, G.; Hirscher, M.; Jensen, T. R.; Filinchuk, Y. Small-Pore Hydridic Frameworks Store Densely Packed Hydrogen. *Nat. Chem.* **2024**, 1–8. https://doi.org/10.1038/s41557-024-01443-x.

(77) Ma, J.; Choudhury, N. A.; Sahai, Y. A Comprehensive Review of Direct Borohydride Fuel Cells. *Renew. Sustain. Energy Rev.* **2010**, *14* (1), 183–199. https://doi.org/10.1016/j.rser.2009.08.002.

(78) Miessler, G. L. *Inorganic Chemistry*; Pearson Education, 2008.

(79) *Inorganic Chemestry*; Rex Bookstore, Inc.

(80) King, R. B. Three-Dimensional Aromaticity in Polyhedral Boranes and Related Molecules. *Chem. Rev.* **2001**, *101* (5), 1119–1152. https://doi.org/10.1021/cr000442t.

(81) 0479-0489.Pdf. https://www.ias.ac.in/public/Volumes/jcsc/093/03/0479-0489.pdf (accessed 2024-05-22).

(82) Shameema, O.; Jemmis, E. D. Relative Stability of Closo-Closo, Closo-Nido, and Nido-Nido Macropolyhedral Boranes: The Role of Orbital Compatibility. *Chem. – Asian J.* **2009**, *4* (8), 1346–1353. https://doi.org/10.1002/asia.200900153.

(83) H. Hagemann, H. (2022). Chemistry of Boron Hydrogen Species in Relation to Hydrogen Storage and the Synthesis of Novel Ionic Conductors [PowerPoint Slides]. Dépt. De Chimie Physique, Université de Genève.).

(84) Moury, R.; Gigante, A.; Hagemann, H. An Alternative Approach to the Synthesis of NaB3H8 and Na2B12H12 for Solid Electrolyte Applications. *Int. J. Hydrog. Energy* **2017**, *42* (35), 22417–22421. https://doi.org/10.1016/j.ijhydene.2017.02.044.

(85) Gavrilova, L. A.; Titov, L. V.; Petrovskii, P. V. Synthesis of $Bu_4NB_{11}H_{14}$ by the Reaction of Tetrabutylammonium Octahydrotriborate with Diborane in Diglyme. *Russ. J. Coord. Chem.* **2004**, *30* (5), 307–308. https://doi.org/10.1023/B:RUCO.0000025997.76929.34.

(86) Berger, A. N. Synthesis of Metal Carborane Electrolytes for New Solid-State Battery Applications.

(87) Naeger, L. Mechanisms of Decaborane Toxicity*1. *Toxicol. Appl. Pharmacol.* **1972**, *22* (4), 517–527. https://doi.org/10.1016/0041-008X(72)90281-5.

(88) Geis, V.; Guttsche, K.; Knapp, C.; Scherer, H.; Uzun, R. Synthesis and Characterization of Synthetically Useful Salts of the Weakly-Coordinating Dianion [B12Cl12]2−. *Dalton Trans.* **2009**, No. 15, 2687. https://doi.org/10.1039/b821030f.

(89) Wang, J.; Steenhaut, T.; Robeyns, K.; Li, H.-W.; Filinchuk, Y. A Simple and Efficient Preparation of High-Purity and High-Yield Unsolvated Lithium Dodecaborate. ChemRxiv April 12, 2024. https://doi.org/10.26434/chemrxiv-2024-7vf8d.

(90) Wang, J.; Steenhaut, T.; Li, H.-W.; Filinchuk, Y. High Yield Autoclave Synthesis of Pure M2B12H12 (M = Na, K). *Inorg. Chem.* **2023**, *62* (5), 2153–2160. https://doi.org/10.1021/acs.inorgchem.2c03810.

(92) Hammersley, A. P.; Svensson, S. O.; Thompson, A. Calibration and Correction of Spatial Distortions in 2D Detector Systems. *Nucl. Instrum. Methods Phys. Res. Sect. Accel. Spectrometers Detect. Assoc. Equip.* **1994**, *346* (1), 312–321. https://doi.org/10.1016/0168-9002(94)90720-X.

(93) Rodriguez-Carvajal, J. Introduction to the Program FULLPROF: Refinement of Crystal and Magnetic Structures from Powder and Single Crystal Data.

(94) Chernyshov, D.; Dyadkin, V.; van Beek, W.; Urakawa, A. Frequency Analysis for Modulation-Enhanced Powder Diffraction. *Acta Crystallogr. Sect. Found. Adv.* **2016**, *72* (4), 500–506. https://doi.org/10.1107/S2053273316008378.

(95) Macrae, C. F.; Sovago, I.; Cottrell, S. J.; Galek, P. T. A.; McCabe, P.; Pidcock, E.; Platings, M.; Shields, G. P.; Stevens, J. S.; Towler, M.; Wood, P. A. Mercury 4.0: From Visualization to Analysis, Design and Prediction. *J. Appl. Crystallogr.* **2020**, *53* (Pt 1), 226–235. https://doi.org/10.1107/S1600576719014092.

(96) Hübschle, C. B.; Sheldrick, G. M.; Dittrich, B. ShelXle: A Qt Graphical User Interface for SHELXL. *J. Appl. Crystallogr.* **2011**, *44* (6), 1281–1284. https://doi.org/10.1107/S0021889811043202.

(97) Hansen, T. C.; Henry, P. F.; Fischer, H. E.; Torregrossa, J.; Convert, P. The D20 Instrument at the ILL: A Versatile High-Intensity Two-Axis Neutron Diffractometer. *Meas. Sci. Technol.* **2008**, *19* (3), 034001. https://doi.org/10.1088/0957-0233/19/3/034001.

(98) *Le Cryostat Orange - ILL Neutrons for Society*. https://www.ill.eu/fr/users/support-labs-infrastructure/sample-environment/services-for-advanced-neutron-environments/historique/cryogenie/le-cryostat-orange/ (accessed 2024-05-08).

(99) Willcott, M. R. MestRe Nova. *J. Am. Chem. Soc.* **2009**, *131* (36), 13180–13180. https://doi.org/10.1021/ja906709t.

(100) Zeolite Molecular Sieves: Structure, Chemistry, and Use D. W. Breck (Union Carbide Corporation, Tarrytown, New York) John Wiley and Sons, New York, London, Sydney, and Toronto. 1974. 771 Pp. $11.95. *J. Chromatogr. Sci.* **1975**, *13* (4), 18A. https://doi.org/10.1093/chromsci/13.4.18A-c.

(101) Kleeberg, F. M.; Zimmermann, L. W.; Schleid, T. The Crystal Structures of Two Hydro-Closo-Borates with Divalent Tin in Comparison: Sn(H2O)3[B10H10] · 3 H2O and

Sn(H2O)3[B12H12] · 4 H2O. *J. Clust. Sci.* **2022**, *33* (6), 2489–2497. https://doi.org/10.1007/s10876-021-02166-6.

(102) Zhou, Z.; Mei, L.; Ma, C.; Xu, F.; Xiao, J.; Xia, Q.; Li, Z. A Novel Bimetallic MIL-101(Cr, Mg) with High CO2 Adsorption Capacity and CO2/N2 Selectivity. *Chem. Eng. Sci.* **2016**, *147*, 109–117. https://doi.org/10.1016/j.ces.2016.03.035.

6. Appendix

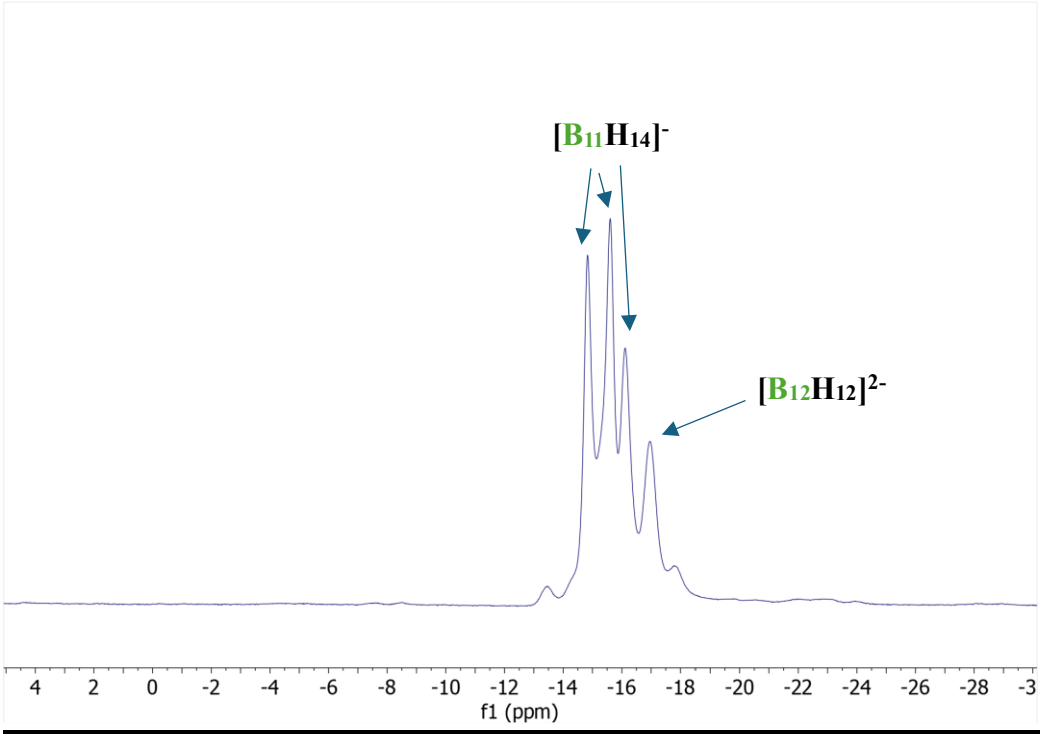

A1. ^{11}B-NMR spectrum of the reaction mixture after one hour for the synthesis of $Na_2B_{12}H_{12}\cdot 4$diglyme.

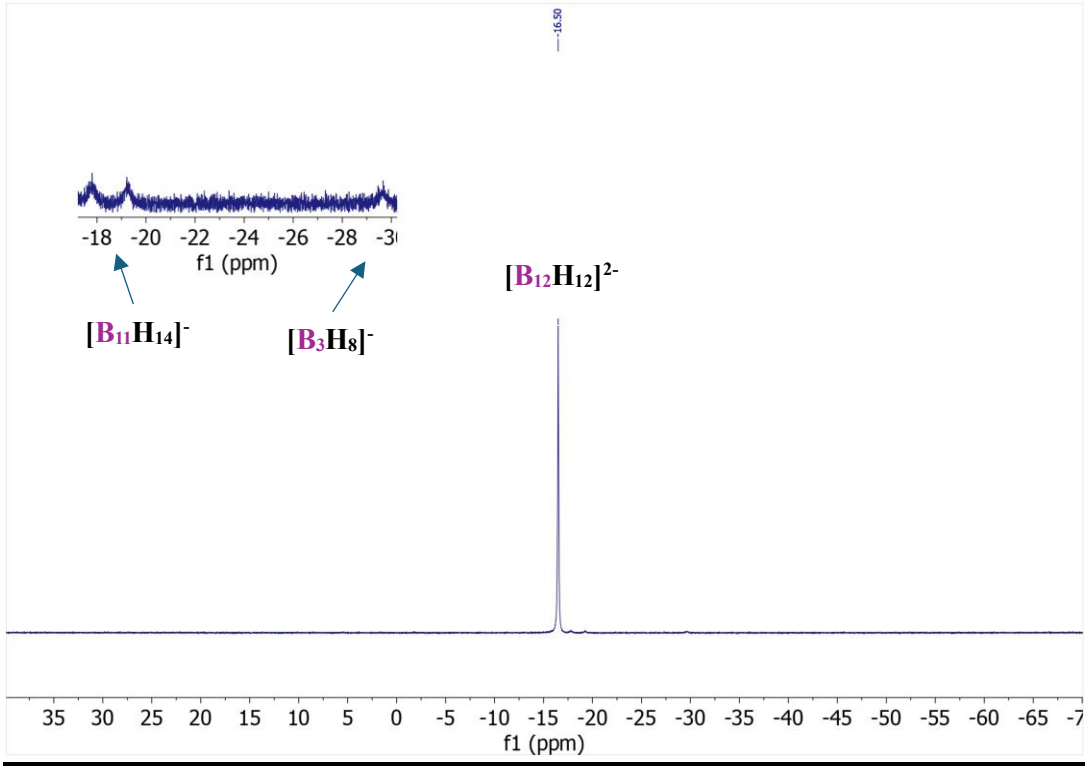

A2. ^{11}B-NMR spectrum of the solid retrieved after synthesis.

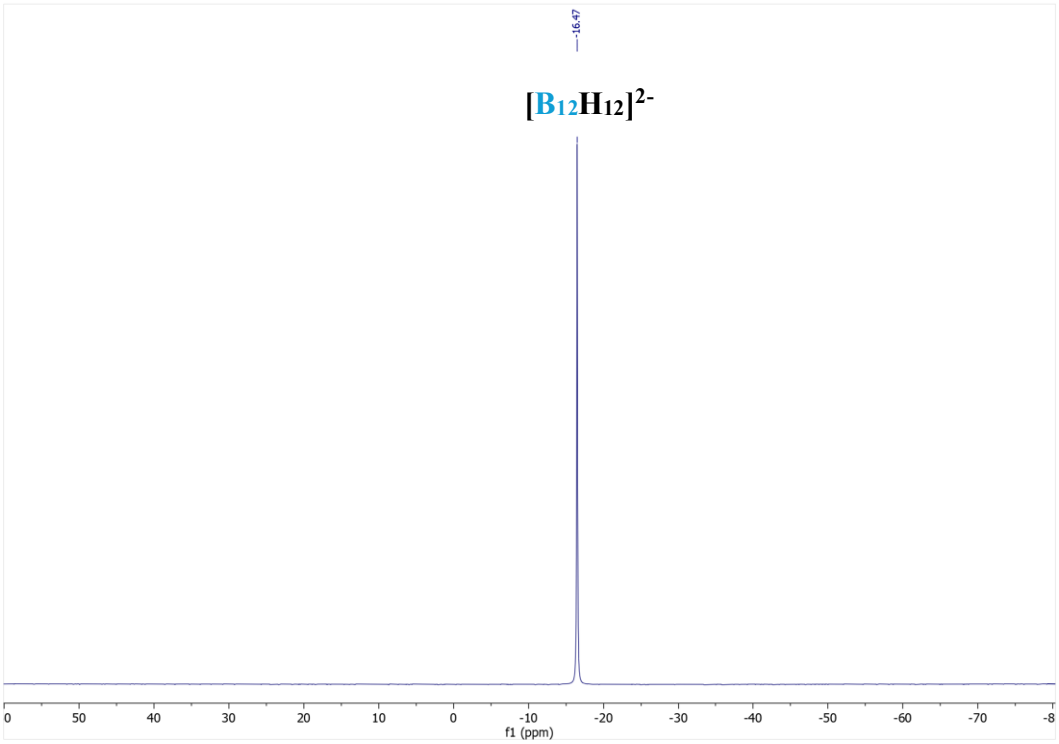

A3. ^{11}B-NMR spectrum of the $Cs_2B_{12}H_{12}$.

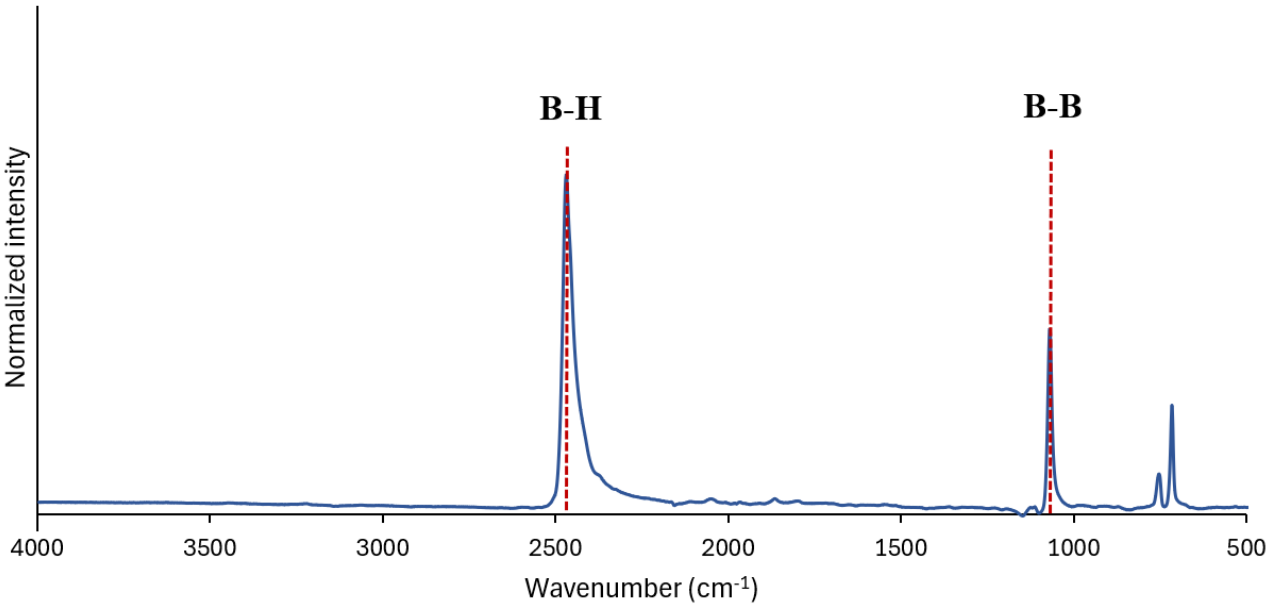

A4. ATR-IR spectrum of $Cs_2B_{12}H_{12}$.

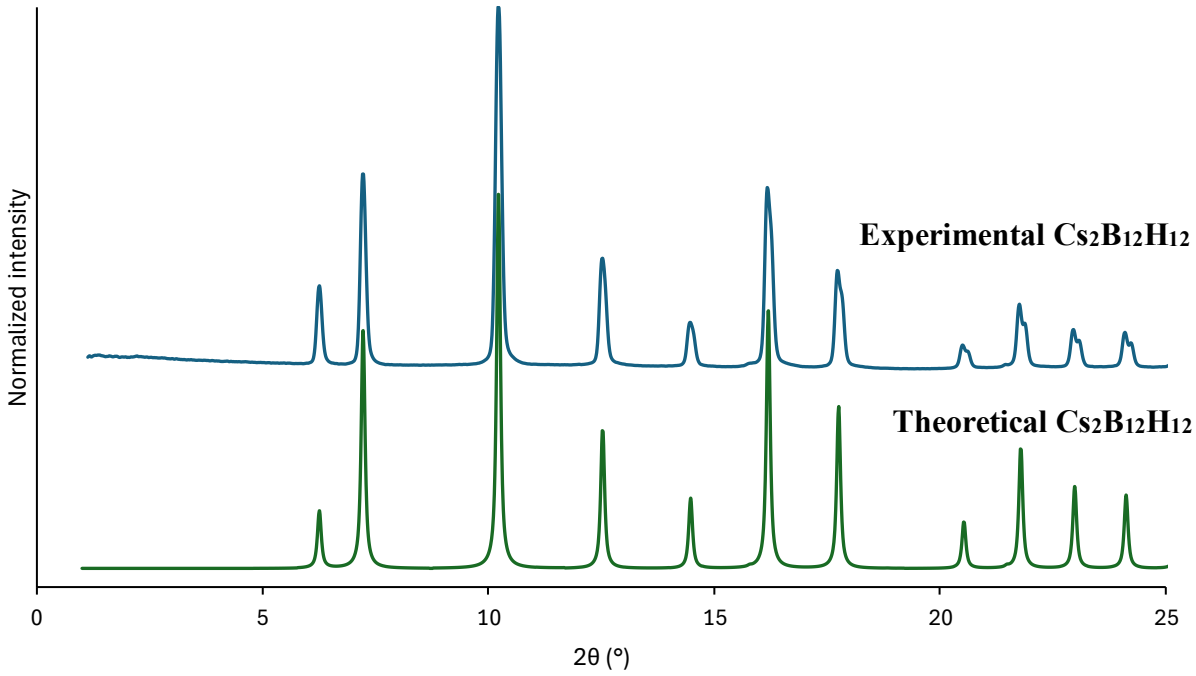

A5. Powder patterns of the theoretical and experimental $Cs_2B_{12}H_{12}$.

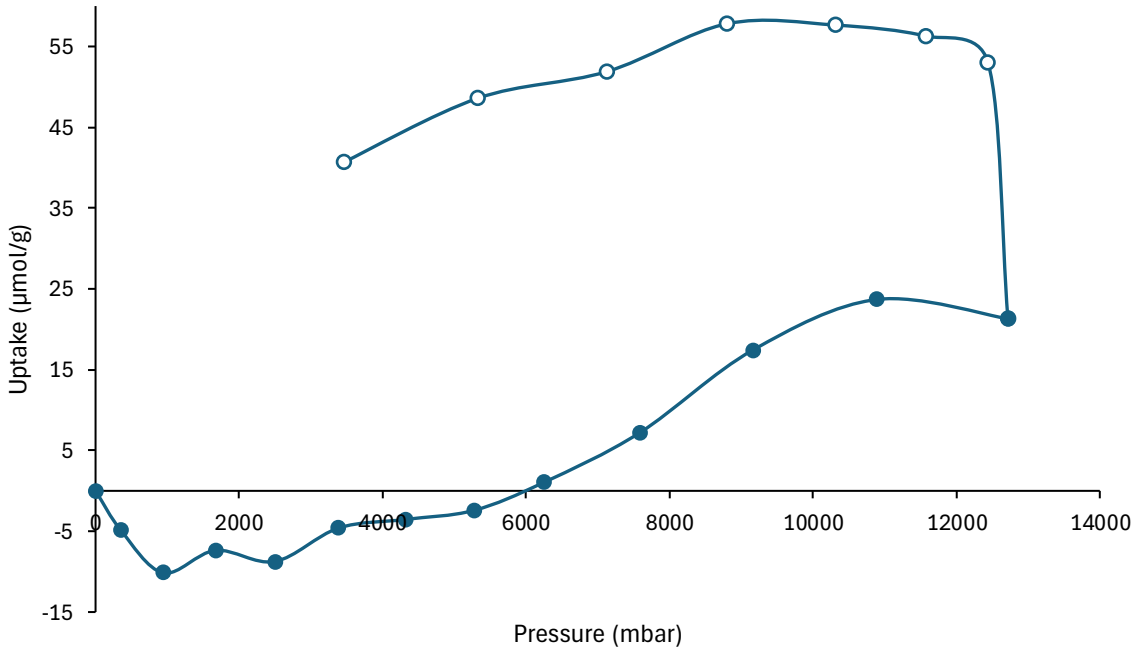

A6. CO_2 sorption isotherm of $Cs_2B_{12}H_{12}$ measured at RT. Sorption is depicted by the full circles, the empty circles picturing the desorption.

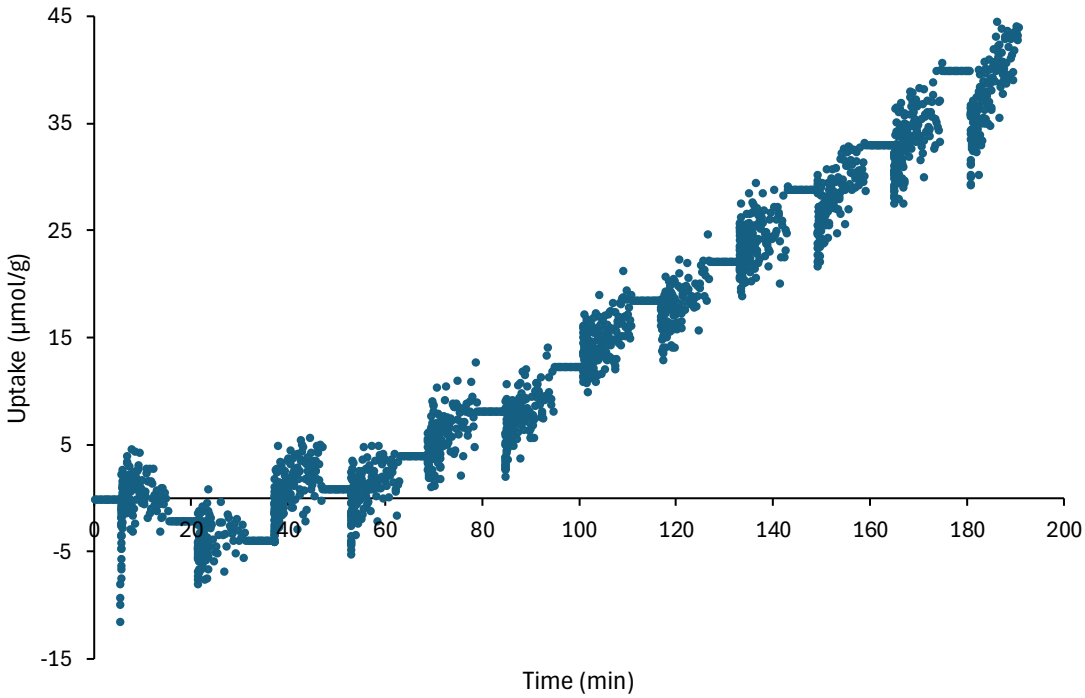

A7. CO_2 sorption kinetics of $Cs_2B_{12}H_{12}$ measured at RT.

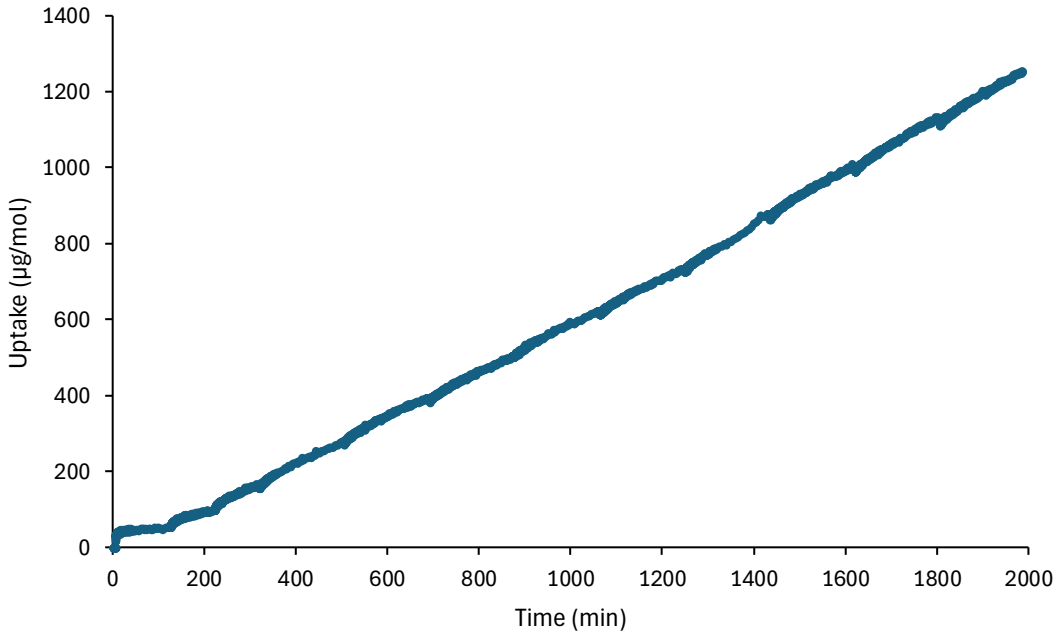

A8. CO_2 sorption kinetics of TMAD.

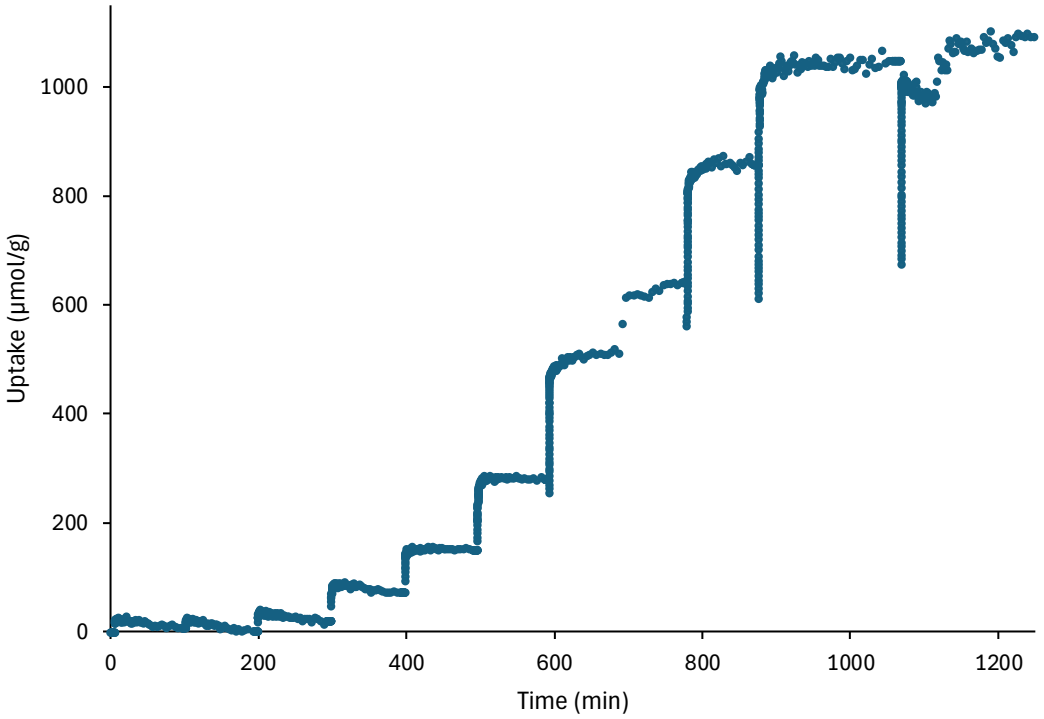

A9. H_2 sorption kinetics of TMAD.

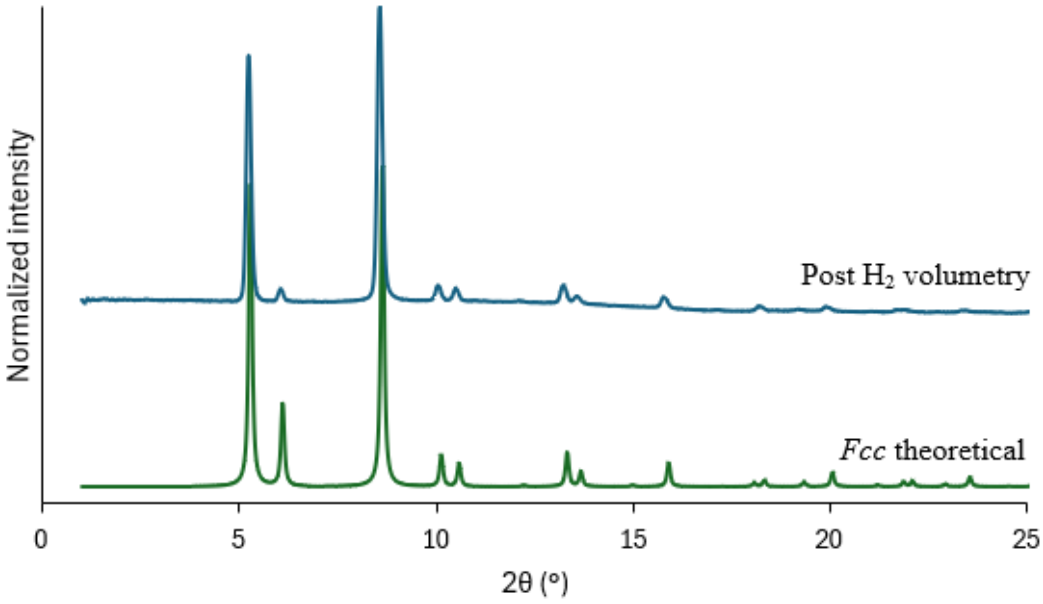

A10. Powder patterns of the *fcc* theoretical and post H_2 volumetry TMAD.

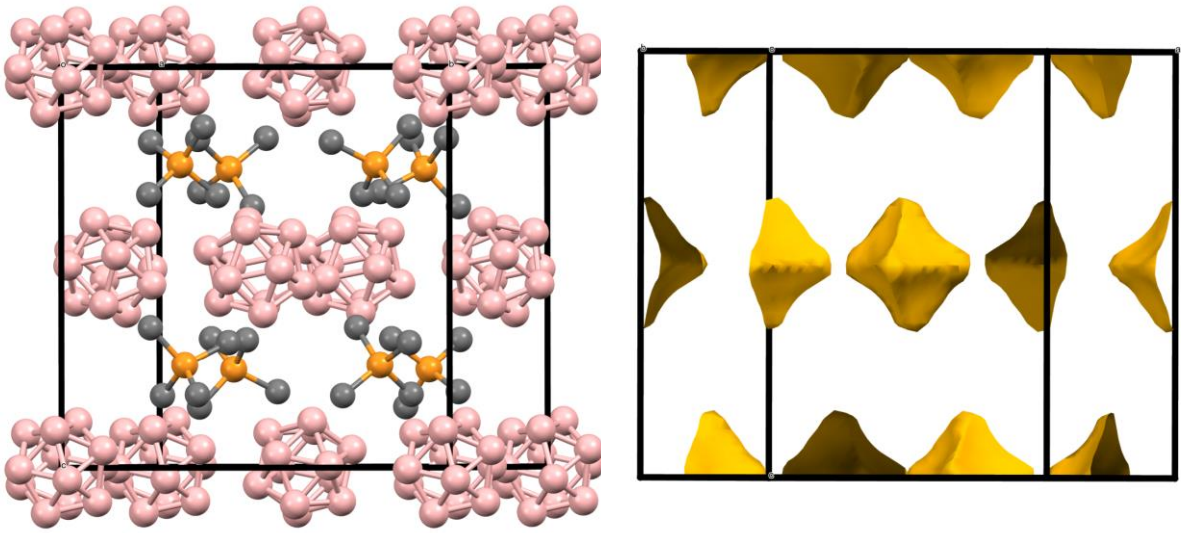

A11. Fcc anti CaF_2 kind of structure of porous TMPD.

CONTINUED **No. 205** $Pa\bar{3}$

Generators selected (1); $t(1,0,0)$; $t(0,1,0)$; $t(0,0,1)$; (2); (3); (5); (13)

Positions

Multiplicity, Wyckoff letter, Site symmetry			Coordinates				Reflection conditions
							h,k,l cyclically permutable
							General:
24	d	1	(1) x,y,z	(2) $\bar{x}+\frac{1}{2},\bar{y},z+\frac{1}{2}$	(3) $\bar{x},y+\frac{1}{2},\bar{z}+\frac{1}{2}$	(4) $x+\frac{1}{2},\bar{y}+\frac{1}{2},\bar{z}$	$0kl$: $k=2n$
			(5) z,x,y	(6) $z+\frac{1}{2},\bar{x}+\frac{1}{2},\bar{y}$	(7) $\bar{z}+\frac{1}{2},\bar{x},y+\frac{1}{2}$	(8) $\bar{z},x+\frac{1}{2},\bar{y}+\frac{1}{2}$	$h00$: $h=2n$
			(9) y,z,x	(10) $\bar{y},z+\frac{1}{2},\bar{x}+\frac{1}{2}$	(11) $y+\frac{1}{2},\bar{z}+\frac{1}{2},\bar{x}$	(12) $\bar{y}+\frac{1}{2},\bar{z},x+\frac{1}{2}$	
			(13) $\bar{x},\bar{y},\bar{z}$	(14) $x+\frac{1}{2},y,\bar{z}+\frac{1}{2}$	(15) $x,\bar{y}+\frac{1}{2},z+\frac{1}{2}$	(16) $\bar{x}+\frac{1}{2},y+\frac{1}{2},z$	
			(17) $\bar{z},\bar{x},\bar{y}$	(18) $\bar{z}+\frac{1}{2},x+\frac{1}{2},y$	(19) $z+\frac{1}{2},x,\bar{y}+\frac{1}{2}$	(20) $z,\bar{x}+\frac{1}{2},y+\frac{1}{2}$	
			(21) $\bar{y},\bar{z},\bar{x}$	(22) $y,\bar{z}+\frac{1}{2},x+\frac{1}{2}$	(23) $\bar{y}+\frac{1}{2},z+\frac{1}{2},x$	(24) $y+\frac{1}{2},z,\bar{x}+\frac{1}{2}$	
							Special: as above, plus
8	c	.3.	x,x,x	$\bar{x}+\frac{1}{2},\bar{x},x+\frac{1}{2}$	$\bar{x},x+\frac{1}{2},\bar{x}+\frac{1}{2}$	$x+\frac{1}{2},\bar{x}+\frac{1}{2},\bar{x}$	no extra conditions
			$\bar{x},\bar{x},\bar{x}$	$x+\frac{1}{2},x,\bar{x}+\frac{1}{2}$	$x,\bar{x}+\frac{1}{2},x+\frac{1}{2}$	$\bar{x}+\frac{1}{2},x+\frac{1}{2},x$	
4	b	.$\bar{3}$.	$\frac{1}{2},\frac{1}{2},\frac{1}{2}$	$0,\frac{1}{2},0$	$\frac{1}{2},0,0$	$0,0,\frac{1}{2}$	hkl : $h+k,h+l,k+l=2n$
4	a	.$\bar{3}$.	$0,0,0$	$\frac{1}{2},0,\frac{1}{2}$	$0,\frac{1}{2},\frac{1}{2}$	$\frac{1}{2},\frac{1}{2},0$	hkl : $h+k,h+l,k+l=2n$

A12. Fcc Wyckoff sites of space group 205 (TMPD).

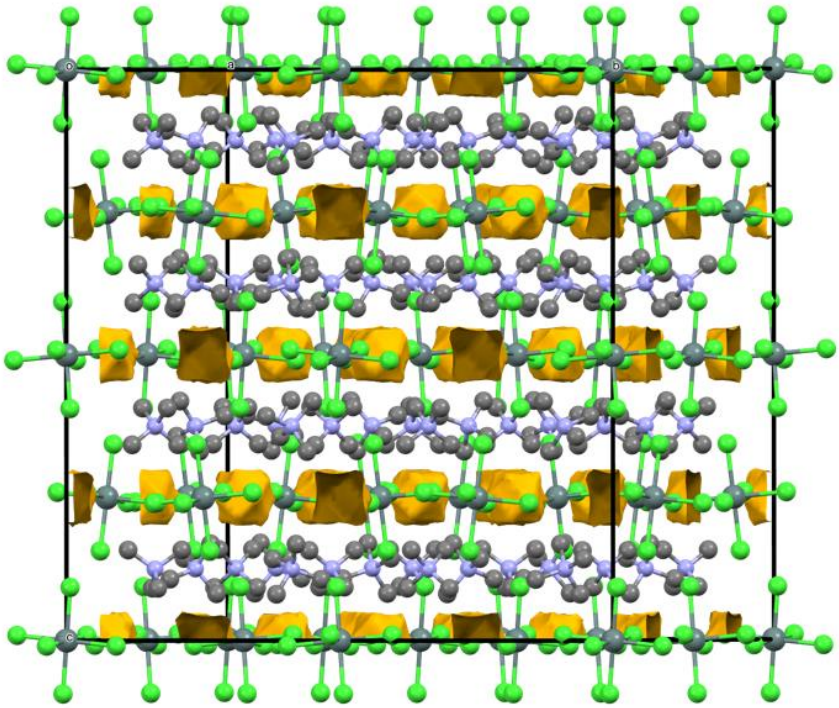

A13. Crystal structure of $(NMe_4)_2SnCl_6$.

UNIVERSITÉ CATHOLIQUE DE LOUVAIN
Faculté des sciences
Place des sciences, 2 bte L6.06.01, 1348 Louvain-la-Neuve, Belgique | **www.uclouvain.be/sc**